

**University of Alberta**

**Modeling Scintillator-Photodiodes as Detectors for Megavoltage Computed  
Tomography**

By



**Thalat Theresa Monajemi**

**A thesis submitted to the Faculty of Graduate Studies and Research in Partial  
fulfillment of the requirement for the degree of Master of Science**

in

**Medical Physics**

**Department of Physics**

**Edmonton, Alberta**

**Spring 2004**



Library and  
Archives Canada

Bibliothèque et  
Archives Canada

Published Heritage  
Branch

Direction du  
Patrimoine de l'édition

395 Wellington Street  
Ottawa ON K1A 0N4  
Canada

395, rue Wellington  
Ottawa ON K1A 0N4  
Canada

*Your file* *Votre référence*

*ISBN: 0-612-96522-8*

*Our file* *Notre référence*

*ISBN: 0-612-96522-8*

The author has granted a non-exclusive license allowing the Library and Archives Canada to reproduce, loan, distribute or sell copies of this thesis in microform, paper or electronic formats.

L'auteur a accordé une licence non exclusive permettant à la Bibliothèque et Archives Canada de reproduire, prêter, distribuer ou vendre des copies de cette thèse sous la forme de microfiche/film, de reproduction sur papier ou sur format électronique.

The author retains ownership of the copyright in this thesis. Neither the thesis nor substantial extracts from it may be printed or otherwise reproduced without the author's permission.

L'auteur conserve la propriété du droit d'auteur qui protège cette thèse. Ni la thèse ni des extraits substantiels de celle-ci ne doivent être imprimés ou autrement reproduits sans son autorisation.

---

In compliance with the Canadian Privacy Act some supporting forms may have been removed from this thesis.

Conformément à la loi canadienne sur la protection de la vie privée, quelques formulaires secondaires ont été enlevés de cette thèse.

While these forms may be included in the document page count, their removal does not represent any loss of content from the thesis.

Bien que ces formulaires aient inclus dans la pagination, il n'y aura aucun contenu manquant.

# Canada

## Abstract

The imaging characteristics of a cadmium tungstate,  $\text{CdWO}_4$ , detector was modeled and measured in 1.25 MeV and 6 MV beams. The detector includes eight  $\text{CdWO}_4$  crystals, each  $2.75 \times 8 \times 10 \text{ mm}^3$ , bonded together and in contact with sixteen silicon photodiodes such that, each crystal covers two photodiodes. The characteristics investigated are the frequency dependent modulation transfer function, MTF (f), noise power spectrum, NPS (f), and detective quantum efficiency, DQE (f). The tools used in modeling these characteristics include the Monte Carlo simulation codes, EGSnrc and DETECT2000, for high energy and optical photons, respectively. The DQE of the detector was found to be approximately constant at 26% and 19% for 1.25 MeV and 6 MV photons up to a spatial frequency of 0.16 cycles/mm, respectively. Due to pulse to pulse fluctuations in the output of the linear accelerator, the NPS(f) and DQE(f) were not verified experimentally in a 6 MV beam.

To Hansol

## Acknowledgements

First and foremost I would like to thank my supervisor, Dr. Satyapal Rathee, for guiding me through my studies as well as being the best teacher I have ever had. I feel immense gratitude towards him for his hard work, patience and knowledge. Without his suggestions and ideas this work would not have been possible.

I would also like to thank my committee members Dr. G. Fallone, Dr. R. Sloboda and Dr. R. Marchand for giving me their time as well as helpful suggestions in completing this thesis.

I would like to thank the members of the Medical Physics department for making my time here enjoyable and interesting. Special thanks go to Alana, Anna, Erin, Keith and Steven for being the coolest office mates ever. Alana, thank you for making me feel guilty every time I eat meat. Thank you for taking me on the crazy adventures. I want to go on more adventures with you! Thank you for teaching me that it is great to have cool world-saving opinions and take a stand on them. Anna, thank you for making the office a fun place to hang out. I love that you say what you feel without worrying about what other people might think. It makes you really fun to talk and listen to. Erin thanks for being a great listener and for being so open about your life. I can honestly say that during the two years that I have known you, I have never had a boring conversation with you. I appreciate and value your honest attitude towards life. Keith, thank you for being the only real-life rock star I have ever known and letting me stalk you and your band. Steven, thank you for always inviting me to do cool stuff. I don't think that I will ever meet someone who likes tobogganing as much as you or makes his students write jokes instead of scientific conclusions to physics experiments. Thank you for teaching me how to swear really well. Thank you for making sitting at my computer really fun.

I would like to thank all four of my parents for believing in me and letting me be who I am, even if I did not turn out to be even remotely close to what they imagined or wished for. Although, I don't wish to favour anyone, I feel that I have to specially thank my father for having sacrificed many opportunities in his life so that I can live my life any way that I desire. I would like to thank my two brothers, Mani and Sina, for being the best little brothers any sister could wish for. Thank you for loving me unconditionally. Thank you for expressing how proud of me you are regardless of what I do or what life choices I make. I feel so incredibly blessed to have you guys in my life.

Last but certainly not least, I would like to thank Hansol for his love and support. Despite all of our ups and downs, I have always felt like I had a shoulder to lean on whenever I needed one. You are my best friend and I feel lucky to have met you and shared part of my life with you.

# Table of Contents

<b>Chapter 1: General Overview.....</b>	<b>1</b>
<b>Chapter 2: Background.....</b>	<b>5</b>
<b>2.1 Conformal Radiotherapy.....</b>	<b>8</b>
2.1.1 Intensity Modulated Radiotherapy.....	8
<b>2.2 Role of Imaging in Delivering IMRT.....</b>	<b>11</b>
<b>2.3 Imaging Devices.....</b>	<b>13</b>
2.3.1 Portal Films.....	13
2.3.2 Electronic Portal Imaging Devices.....	14
2.3.3 3-D Computed Tomography for Set up Verification.....	15
<b>2.4 CT Imaging Options Available in Treatment Position.....</b>	<b>16</b>
2.4.1 Linear accelerator Plus Diagnostic kVCT Scanner.....	17
2.4.2 Linear Accelerator plus kV Cone Beam CT.....	17
2.4.3 MVCT.....	18
2.4.3.1 History.....	18
2.4.3.2 Problems with MVCT.....	21
<b>2.5 Types of Detectors Used in CT Imaging.....</b>	<b>23</b>
2.5.1 Gas Detectors.....	23
2.5.2 Scintillation Detectors.....	25
<b>Chapter 3: Materials and Methods.....</b>	<b>30</b>
<b>3.1 Single Crystals.....</b>	<b>31</b>
3.1.1 Choice of Scintillators.....	32
<b>3.2 CdWO<sub>4</sub> Detector Array.....</b>	<b>35</b>
3.2.1 Detector Electronics.....	36
3.2.1.1 Detector Assembly Components.....	37

3.2.1.2 Data Acquisition Control Circuits.....	44
3.2.1.3 Data Acquisition Sequence.....	45
<b>3.3 Software Tools.....</b>	<b>49</b>
3.3.1 EGSnrc.....	49
3.3.1.1 Transport Parameters Used in our EGSnrc User Code.....	53
3.3.2 DETECT2000.....	54
3.3.2.1 Surface Models in DETECT2000.....	54
<b>3.4 Studies Performed on Single Crystals.....</b>	<b>60</b>
3.4.1 Calculation Model.....	61
3.4.2 Measurements.....	66
3.4.2.1 Single Crystal Signal.....	66
3.4.2.2 Afterglow Assessment.....	66
<b>3.5 Dose Response and Beam Attenuation Characteristics of the CdWO<sub>4</sub> Detector.....</b>	<b>67</b>
3.5.1 Detector Dose Response.....	68
3.5.2 Measurements of Beam Attenuation.....	68
<b>3.6 Imaging Characteristics Studies Performed on the CdWO<sub>4</sub> Detector Array.....</b>	<b>69</b>
3.6.1 Modeling the Imaging Characteristics.....	74
3.6.1.1 Detector Geometry.....	74
3.6.1.2 Theory Used in Calculating the Imaging Characteristics.....	77
3.6.2 Measurements.....	83
3.6.3 Checking the Upper Limit of DQE (f).....	86
<b>Chapter 4: Results and Discussion.....</b>	<b>90</b>
<b>4.1 Single Crystals.....</b>	<b>91</b>
4.1.1 Afterglow Assessment.....	91



4.1.2 Detector Signal as a Function of Crystal Height.....	92
<b>4.2 Linearity of CdWO<sub>4</sub> Array Detector.....</b>	<b>94</b>
4.2.1 Detector Dose Response.....	95
4.2.2 Measurement of the Beam Attenuation.....	96
<b>4.3 Imaging Characteristics Performed on the CdWO<sub>4</sub> Detector...98</b>	
4.3.1 Gamma Photon Energy Deposition.....	98
4.3.2 Optical Photon Transport.....	100
4.3.3 Checking the Upper Limit of DQE(0).....	106
<b>4.4 Measured and Modeled LSF, MTF (f), NPS (f) and DQE(f).....108</b>	
<b>Chapter 5: Future Directions.....</b>	<b>116</b>
<b>5.1 Aliasing.....</b>	<b>116</b>
5.1.1 Theory.....	116
5.1.2 Materials and Methods.....	118
5.1.3 Results and Discussion.....	119
<b>5.2 Crystal Height.....</b>	<b>124</b>
5.2.1 Materials and Methods.....	124
5.2.2 Results and Discussion.....	125
<b>Chapter 6: Conclusions.....</b>	<b>133</b>
<b>Bibliography.....</b>	<b>137</b>

## List of Tables

Table 3.1	Properties of selected $\gamma$ -ray detecting scintillators.....	34
Table 4.1	The results of the preliminary assessment of DQE(0) of the array of CdWO <sub>4</sub> detector, using the output of EGSnrc.....	106
Table 5.1	The results of the preliminary assessment of DQE(0) of the array of CdWO <sub>4</sub> detector with crystals of heights 3, 4, 5, 6, and 8 cm in 1.25 MeV beam, using the Swank analysis of section 3.6.3.....	128

## List of Figures

Figure 2.1	Xenon gas detector.....	24
Figure 2.2	Scintillation detector.....	26
Figure 3.1	Photograph of photodiodes and single CdWO <sub>4</sub> crystals.....	31
Figure 3.2	The geometry of our CdWO <sub>4</sub> detector.....	36
Figure 3.3	The Detector electronics schematics.....	37
Figure 3.4	Circuit diagram showing the detector assembly components.....	38
Figure 3.5	The basis for operation of photodiodes.....	41
Figure 3.6	Data acquisition timing sequence for the eight-channel detector assembly in Co <sup>60</sup> Measurements.....	46
Figure 3.7	Data acquisition timing sequence for the eight-channel detector assembly in 6 MV Measurements.....	48
Figure 3.8	Polar plot of the distribution of light created by POLISH and GROUND surface models.....	57
Figure 3.9	Polar plot of the distribution of light created by the UNIFIED surface model.....	59
Figure 3.10	The optical emission spectrum of CdWO <sub>4</sub> as used in our study....	63
Figure 3.11	The optical emission spectrum of CsI(Tl) as used in our study....	63
Figure 3.12	Absorption mean free path of optical photons in CdWO <sub>4</sub> as Used in our Study.....	64
Figure 3.13	Photosensitivity spectrum of the photodiodes as used in our study.....	64
Figure 3.14	The modeled and real single CsI(Tl) crystal.....	65
Figure 3.15	The set-up used in measuring the signal of single crystals.....	66
Figure 3.16	The set-up used in measuring the beam attenuation.....	69
Figure 3.17	The modeled geometry of the 8-element crystal array.....	76
Figure 3.18	Varian600C energy spectrum for 6MV photons .....	83

Figure 3.19	Experimental set-up for finding the imaging characteristic of our prototype detector.....	86
Figure 4.1	Afterglow assessment of 1cm long CdWO <sub>4</sub> and CsI(Tl) crystals..	92
Figure 4.2	The normalized measured and modeled signals as a function of crystal height for both CdWO <sub>4</sub> and CsI(Tl) single crystals under identical conditions in a Co <sup>60</sup> beam.....	93
Figure 4.3	Results of optical simulations for single crystals in DETECT2000.....	94
Figure 4.4	Dose response of the prototype detector.....	96
Figure 4.5	Attenuation response of the prototype detector.....	97
Figure 4.6	Simulated energy deposition for 1.25 MeV and 6 MV photons...	99
Figure 4.7	Simulated energy deposition for 1.25 MeV and 6 MV photons	100
Figure 4.8	The optical LSF for various locations of line sources in the x-direction and at a depth of 4.5 mm within the fourth crystal.....	102
Figure 4.9	The optical LSFs for the optical line sources at 0.5 mm and 9.5mm depths in the central voxel of the fourth crystal in x-direction.....	102
Figure 4.10	Simulated fraction of detected optical photons as a function of the depth of the optical line source at the center of the fourth crystal in CdWO <sub>4</sub> detector array.....	104
Figure 4.11	Simulated fraction of bulk absorbed optical photons as a function of the depth of the optical line source at the center of the fourth crystal in CdWO <sub>4</sub> detector array.....	104
Figure 4.12	Simulated fraction of surface absorbed optical photons as a function of the depth of the optical line source at the center of the fourth crystal in CdWO <sub>4</sub> detector array.....	105
Figure 4.13	Simulated fraction of transmitted optical photons as a function of the depth of the optical line source at the center of the fourth crystal in CdWO <sub>4</sub> detector array.....	105

Figure 4.14	Absorbed energy distributions for 1.25 MeV and 6 MV photons as given by the output of EGSnrc.....	107
Figure 4.15	The modeled and measured LSF for the 8-element crystal array in 1.25 MeV beam.....	108
Figure 4.16:	The modeled and measured MTF(f) for the 8-element crystal array in 1.25 MeV beam.....	109
Figure 4.17	The modeled and measured normalized $NPS_{det}(f)$ for the 8-element crystal array in 1.25 MeV.....	109
Figure 4.18	The modeled and measured DQE(f) for the 8-element crystal array in 1.25 MeV.....	110
Figure 4.19	The modeled and measured MTF(f) for the 8-element crystal array in 6 MV beam.....	111
Figure 4.20	The modeled and measured normalized $NPS_{det}(f)$ for the 8-element crystal array in 6MV.....	112
Figure 4.21	The modeled and measured DQE(f) for the 8-element crystal array in 6 MV.....	112
Figure 4.22	The pulse to pulse fluctuations in the output of a Varian600C linac as measured by our detector.....	113
Figure 5.1	The simulated MTF(f) of the 8 and 16 element array of $CdWO_4$ in a 1.25 MeV beam.....	121
Figure 5.2	The simulated NPS(f) of the 8 and 16 element array of $CdWO_4$ in a 1.25 MeV beam.....	121
Figure 5.3	The simulated DQE(f) of the 8 and 16 element array of $CdWO_4$ in a 1.25 MeV beam.....	122
Figure 5.4	The simulated MTF(f) of the 8 and 16 element Array of $CdWO_4$ in a 6 MV beam.....	122
Figure 5.5	The simulated NPS (f) of the 8 and 16 element array of $CdWO_4$ in a 6 MV beam.....	123

Figure 5.6	The simulated DQE (f) of the 8 and 16 element Array of CdWO <sub>4</sub> in a 6 MV beam.....	123
Figure 5.7	The results of the simulations of the MTF(f) of the 8-element CdWO <sub>4</sub> array with crystal heights of 5,6, and 8 cm in a 1.25 MeV beam.....	128
Figure 5.8	The results of the simulations of the NPS(f) of the 8-element CdWO <sub>4</sub> array with crystal heights of 5,6, and 8 cm in a 1.25 MeV beam.....	129
Figure 5.9	The results of the simulations of the DQE(f) of the 8-element CdWO <sub>4</sub> array with crystal heights of 5,6, and 8 cm in a 1.25 MeV beam.....	129
Figure 5.10	The fraction of optical photons detected, as a function of the original z location of the line optical photon source in a 2.75 x 8 x 60 mm <sup>3</sup> CdWO <sub>4</sub> crystal.....	130
Figure 5.11	The fraction of optical photons bulk absorbed, as a function of the original z location of the line optical photon source in a 2.75 x 8 x 60 mm <sup>3</sup> CdWO <sub>4</sub> crystal.....	130
Figure 5.12	The fraction of optical photons surface absorbed, as a function of the original z location of the line optical photon source in a 2.75 x 8 x 60 mm <sup>3</sup> CdWO <sub>4</sub> crystal.....	131
Figure 5.13	The fraction of optical photons transmitted through the photodiodes, as a function of the original z location of the line optical photon source in a 2.75 x 8 x 60 mm <sup>3</sup> CdWO <sub>4</sub> crystal.....	131

## List of Abbreviations

AED	Absorbed Energy Distribution
CdWO <sub>4</sub>	Cadmium Tungstate
Co <sup>60</sup>	Cobalt-60
CsI(Tl)	Cesium Iodide (Thallium doped)
CTV	Clinical Tumour Volume
DQE(f)	Detective Quantum Efficiency (Frequency dependent)
DRR	Digitally Reconstructed Radiographs
EPID	Electronic Portal Imaging Device
GTV	Gross Tumour Volume
IMRT	Intensity Modulated Radiotherapy
kV	Kilo-Voltage
kVCT	Kilo-Voltage Computed Tomography
LSF	Line Spread Function
MTF(f)	Modulation Transfer Function (Frequency dependent)
MVCT	Mega-Voltage Computed Tomography
NPS(f)	Noise Power Spectrum
PTV	Planning Target Volume

## Chapter 1: GENERAL OVERVIEW

Megavoltage Computed Tomography (MVCT) is an imaging technique for verifying the patient position during fractionated radiotherapy (see section 2.4.3). The advantage of this modality over portal films (see section 2.3.1) and Electronic Portal Imaging Devices (EPIDs) (see section 2.3.2) is that MVCT offers three-dimensional images of the patient instead of two-dimensional projections. Although MVCT offers some advantages over kilovoltage Computed Tomography (kVCT) such as easier inhomogeneity corrections (see section 2.4.3.1) and less complicated engineering of the treatment system, the main problems with MVCT are poor low contrast resolution, high image noise and large dose to patients (see section 2.4.3.2). To minimize the consequences of these problems, it is very important that the detectors used for imaging at MV energies are optimized to perform adequately to give high image quality at a reasonable dose delivered to the patients. In fact, all the problems mentioned above are inherent to interaction and dose deposition properties of MV photons, and the only fundamental improvement in image quality and patient dose performance can come from improving the performance of the detectors. Important characteristics of a detector are low cost, high efficiency, stability, fast temporal response, and linearity of response to radiation over a wide range of beam energies and intensities, freedom from electronic noise, and a compact size. The detective quantum efficiency (DQE) is the squared ratio of signal to noise, SNR, in detector signal to inherent quantum SNR of the incident beam (Barrett and Swindell, 1981). A higher DQE gives better statistics and therefore leads to the need for lesser dose to obtain images with good soft tissue contrast. Stability is measured by consistency and reproducibility of detector response from moment to moment. Detectors are usually frequently recalibrated to ensure their stability. Responsiveness is measured by the time that it takes the detector to receive, record and discard a signal sample.



There are many parameters in the design of a detector that have to be considered for optimization. For example in optimizing a scintillation detector, these parameters include the scintillation material type, geometry and dimensions, surface finish and coating, optical glue type as well as photodiode type and geometry. Since all of these parameters have to be taken into consideration, it is beneficial to use a computer model to optimize these parameters to save time and cost, and to gain efficiency.

The objective of this research is to model the imaging characteristics of a prototype scintillator-photodiode detector for MVCT. The detector is an array of eight  $\text{CdWO}_4$  crystals in contact with photodiodes. The ultimate goal of this project is to optimize this detector based on the model developed, build this optimized version, and study the imaging characteristics of the final detector. This thesis is organized into six different chapters.

A general background to the thesis is given in chapter 2. The topics include different steps taken in treating a patient in radiotherapy, a discussion of conformal radiotherapy and intensity modulated radiotherapy (IMRT), role of imaging in delivering IMRT, different imaging devices employed in delivering IMRT in particular portal films, EPIDs and Computed Tomography (CT), the three-dimensional imaging options which are available in treatment position, a more detailed look into MVCT including its history and the problems associated with it followed by an introduction to different types of detectors employed in MVCT including gas detectors and solid state detectors.

The materials, methods and theory used to model the detector array including the measurements are presented in chapter 3. The instrumentation and electronics of the prototype detector are described; these include the characteristics of scintillation crystals, photodiodes, the detector assembly board, data acquisition control circuit board and the analogue-to-digital (A-to-D) converter board. The details of the software tools employed in the Monte Carlo simulation of high-energy photons, EGSnrc, and optical photons, DETECT2000, are provided. Monte Carlo simulations and experimental methods are used to calculate and measure the signal produced by single crystals of  $\text{CsI(Tl)}$  and

CdWO<sub>4</sub> of various heights. The afterglow in the two crystal types is experimentally measured. This chapter also describes the two simple experiments performed to assess the linearity of the detector response with respect to dose and in the measurement of attenuation provided by solid water slabs. In the last part of chapter 3, the theory for modelling and measuring the basic imaging characteristics of this prototype array is described. These characteristics include the frequency dependent modulation transfer function, MTF(f), noise power spectrum, NPS(f), and detective quantum efficient, DQE(f).

In chapter 4, the results of the experiments explained in chapter 3 are presented and discussed. These results include the afterglow assessment and a comparison of the modeled and measured signals as a function of crystal height in a Co<sup>60</sup> beam along with the corresponding details of optical photon simulations in DETECT2000 for single crystals of CdWO<sub>4</sub> and CsI(Tl). The second set of results shows the linearity of the prototype detector both in a blocked and unblocked Co<sup>60</sup> beam. The measured and modelled imaging characteristics of the prototype detector in Co<sup>60</sup> and 6 MV beams are presented. It is also shown why we were not able to measure the NPS(f) and DQE(f) in the 6 MV beam. In this chapter the details of optical photon transport for the prototype detector are also shown.

In chapter 5, the detector model as developed in the study is applied to various different types of crystal geometry. In the first part, a 16-element crystal array is compared with the previous 8-element array in order to understand the effect of reducing crystal width on MTF(f), NPS(f) and DQE(f). In the second part, the effect of increasing the crystal height on imaging parameters is considered in order to determine the theoretical height which gives the maximum DQE(f).

Chapter 6 provides the conclusions based on the theoretical modelling and the experimental measurements.

**References:**

<sup>1</sup> Barret H., Swindell W., *Radiological Imaging: The Theory of Image Formation, Detection, and Processing*, (Academic Press, 1981).

## Chapter 2: BACKGROUND

The process of treating tumours using radiation is very complex and involves many steps. As summarised by Van Dyk (1999), these steps include: diagnosis and 3-D imaging, target volume and organ localization, beam selection, optimization, shaping and dose calculation, treatment simulation, biological modeling and prescription, treatment verification and delivery, and patient follow up. These steps are now briefly described.

- *Diagnosis and 3-D Imaging:*

Once a patient is diagnosed with cancer using cytology, pathology, imaging or other diagnostic techniques, the first step is to determine the stage of the tumour. This is followed by a decision as to whether the patient is going to be considered for curative or palliative treatment. In either case imaging for treatment planning is necessary, and a diagnostic imaging system such as x-ray computed tomography (CT), magnetic resonance imaging (MRI), single photon emission tomography (SPECT), positron emission tomography (PET) and ultrasound maybe used. The patient is imaged while in the same immobilization system as used for the treatment.

- *Planning Target Volume (PTV) and Critical Organ Localization:*

Report number 50, from the International Commission of Radiation Units and measurements (ICRU, 1993), has addressed the standardization of the terminology of specifying planning target volume (PTV) and prescribing dose. The gross tumour volume (GTV) is drawn by an oncologist within the 3D images of the patient using the tools in the treatment-planning computer. This volume

includes the palpable or visible extent and location of the malignant growth. The clinical target volume (CTV) is obtained by placing a margin around GTV. The CTV includes the microscopic extent of cancerous cells and this volume must be adequately irradiated to achieve the goal of therapy. In order to achieve adequate irradiation of the CTV, a margin is placed around the CTV that accounts for the day-to-day setup uncertainty of the patient and the other geometrical errors in the treatment unit. This volume is called the PTV. Critical organs are any organs that are located close to the PTV and the function of these organs may be compromised if unnecessary irradiation occurs. These organs are also delineated within the 3D images of the patient by an oncologist and/or a treatment planner.

- *Beam Selection, Shaping, Optimisation and Dose Calculation:*

A set of treatment beams of radiation type, energy, orientation and field size are selected in order to adequately irradiate the PTV and avoid unnecessary irradiation of the critical organs. Beam modifying devices, such as wedges and missing tissue compensators in photon beams, and tissue equivalent bolus in electron beams, are often used to improve the uniformity of radiation dose distribution throughout the PTV. The dose calculation is performed by the treatment planning system and displayed as an overlay over the PTV and critical organs. Once the physician chooses a suitable treatment plan, the beam shaping cerrobend blocks and the other beam modifying devices are manufactured.

- *Treatment Simulation:*

A radiotherapy treatment simulator is a machine that has the same geometry as the treatment unit, but uses diagnostic quality x-rays to perform localization and treatment planning verifications (Van Dyk and Munro, 1999). It is used to make sure that the selection of treatment beam orientations and shapes is safely deliverable by the treatment unit. One important function of the treatment simulation is to create a reference image (i.e. radiographic film image) of each

beam. This image is used to ensure that the patient's set up is reasonably reproducible day-to-day by comparing the images with the portal images taken with megavoltage (MV) photon beams. Nowadays, more and more treatment sites use digitally reconstructed radiographs (DRRs), a divergent projection through the patient's CT data set, to replace radiographic film image for the reference image. Therefore, need of the conventional simulators is decreasing.

- *Biological Modeling and Prescription:*

Research is being carried out using biological models such as normal tissue control probability and tumour response (Van Dyk, 1999) to check the amount of dose prescribed to different tumour sites and maximum dose tolerable by the critical organs. However, this approach is currently under development and is not widely used in clinical practice. In general, after reviewing the dose distribution calculated by the treatment planning system, a dose is prescribed by the physician and the amount of radiation delivered to the patient by each beam is calculated using the prescription and the treatment plan data.

- *Treatment Verification and Delivery:*

The patient is treated in one of Co<sup>60</sup>, linear accelerator, brachytherapy or superficial orthovoltage machine. The patient set up during treatment is often verified using portal imagers or other imagers.

- *Patient Follow-up:*

Finally the tumour control and normal tissue response are evaluated during treatment and a few years following the treatment for example by using diagnostic imaging systems and other diagnostic tools.

## **2.1 Conformal Radiotherapy**

The main goal in radiation therapy is to deliver a dose as high as necessary to the tumour while minimizing the dose to the surrounding normal tissue. In order to achieve this goal, conformal radiotherapy has been developed (Mohan, 1996). This technique of radiotherapy is an attempt to conform the shape of the treatment beams in all three dimensions to the exact shape of the tumour and at the same time to minimize the dose to the surrounding normal tissue (Mohan, 1996). The biological hypothesis behind conformal radiotherapy is that improved local tumour control decreases the probability of developing distant metastasis. This hypothesis assumes that distant metastases occur if some residual tumour exists after radiation treatment is completed (Mohan, 1996). In practice, it has been found that the accuracy in achieving total conformation to the tumour volume depends on the tumour site, extent of the disease, the localization and nature of the normal critical structures and the delivery technique. In many cases, the use of conformal radiotherapy alone is not sufficient for delivering the desired tumour and normal tissue doses, especially when a critical organ is located close to a concave shaped PTV such as in head and neck and prostate cancers (Mohan, 1996).

### **2.1.1 Intensity Modulated Radiotherapy**

In order to overcome some of the shortcomings of conformal radiotherapy, intensity modulated radiotherapy (IMRT) has been developed. In conformal therapy, while the beams are conformed to the shape of the PTV, the beam intensity is uniform within the unblocked part of the field. In IMRT, the intensity of the beam within the conformed portion of the field is modulated to provide even greater conformance of the dose to the PTV (Mohan, 1996). In inverse planned IMRT, a treatment-planning computer optimizes the 2-D intensity

modulated fluence profiles of each beam based on the dosimetric requirements of the PTV, and the constraints of the critical organs. Although the optimization algorithm used in the present systems are all based on physical dose constraints, the process of inverse planned IMRT conceptually lends itself to the use of biological constraints to be used in the optimization process (Mohan, 1996). Most systems that are used in the clinic require the initial selection of beam directions. The optimization algorithm then produces the modulated fluence profiles by taking care of the dose constraints specified by the user as well as the patient surface irregularities, tissue inhomogeneities, and scattered radiation. IMRT is also used in simple cases where the modulation of the fluence of a given beam is designed semi-automatically by the user. This process is called forward planned IMRT in that an inverse optimization of the fluence profiles is not used (Mohan, 1996). Irrespective of the method for obtaining the modulated 2-D fluence profiles of the treatment beams, there can be several means of delivering such fluence profiles in practice. Some techniques that are used for delivering IMRT beams are multileaf collimators (MLCs) and computer-controlled radiotherapy (CCRT) (Mohan, 1996).

IMRT can be delivered in many ways. Currently there are at least six methods of delivering IMRT (Webb, 2001).

- *Cast Metal Compensators:*

This simple technique gives different beam intensities across the field depending on the shape of the compensator.

- *Multiple-Static MLCs:*

These MLC sub-fields are stationary when the radiation is on and move to different pre-planned positions when radiation is off. The sum of radiation delivered from different MLC sub-fields when the beam is on gives the final



distribution of the beam at a specified orientation. The process is then repeated for the other beam orientations.

- *Dynamic MLCs:*

These MLC fields are able to move during beam on times. A method of delivering IMRT developed by Yu in 1995 uses the capabilities of dynamic MLCs and arc therapy. In this approach the MLC positions change during the gantry rotation. Several superimposing arcs are used where for each arc, a different multileaf position is employed for each angle. The goal is to get the desired dose distribution when all the beams are added together (Mohan, 1996).

- *Tomotherapy:*

In this form of delivering IMRT, the radiation is collimated to a fan beam. The MLC leaf movement is binary such that the individual leaves are either in or out of the fan beam path at a very high speed (Webb, 2001). Therefore, at a given time, individual leaves are either open or closed. The success of the beam distribution produced by this method depends on the rapid switching of the different collimator elements between open and closed positions according to the plan. Tomotherapy is delivered in two forms: helical tomotherapy (Mackie et al., 1993, Olivera et al., 1999) and sequential tomotherapy (Carol, 1995). During helical tomotherapy a longitudinal translation of the couch and the gantry rotation occur at the same time while the binary MLC leaves are rapidly opening and closing according to the sinogram pattern designed by the treatment planning system. This way, the modulated slit treatment beam describes a helical path around the patient. During sequential tomotherapy the gantry rotates around the patient at a fixed longitudinal position of couch while the leaves open and close as a function of gantry angle. The couch is then moved in the longitudinal direction by a specified length in a very accurate and precise manner so that no cold or hot spots occur in the longitudinal direction. This is followed by the rotation of the

gantry and the process is repeated until the entire length of the PTV is covered. The precision of the longitudinal movement is maintained by an external indexing device that controls the couch movement. This way the patient is treated one slice at a time (Mohan, 1996).

- *Scanning Attenuating Bar:*

An attenuating bar is programmed to dwell at certain places in the field more than others. The places at which the bar dwells the most get the least amount of radiation. By programming the movements of the bar the desired beam distribution is achieved (Webb, 2001).

- *Swept Pencils of Radiation:*

As the name suggests, this method employs sweeping pencils of radiation that move across the radiation field based on a pre-programmed plan to create the desired dose distribution (Webb, 2001).

## **2.2 Role of Imaging in Delivering IMRT**

Since the goal of radiation therapy is to deliver a dose as high as possible to the tumour while sparing the surrounding normal tissue, it is very important to guarantee safety by delivering accurate treatment. Most treatments are delivered in fractions, which makes reproducibility of the PTV and the internal critical organ positions with respect to the treatment beams very important. Experiments have shown that an error in dose delivery of 7% to 15% can significantly compromise tumour control and create increased normal tissue complications (Munro, 1999). Conformal radiotherapy and IMRT are new techniques that make achieving the main goal of radiation therapy easier. The problem with conformal radiotherapy and IMRT is that the planned dose gradients at the edges of the PTV are very large to minimize irradiation of normal tissue. Therefore, a small error in

positioning the patient results in delivering large dose to the surrounding normal tissue and not enough dose to the tumour, both of which are undesirable situations. When treatment is delivered in many fractions, there are complications due to daily patient set up, tumour shape change, and tumour and critical organ motion. The discrepancy between the planned and the delivered dose is classified as systematic (class A) or random (class B). A "class A" error repeats itself many times during the course of a treatment. These errors are potentially more dangerous of the two because they result in a systematic shift in the planned dose. Random errors are less problematic because during the entire course of a treatment they might cancel each other out. It has been suggested that the potential tolerable level for the discrepancy between the planned and delivered dose can be up to 5% (ICRU 39, 1985). Therefore it is very important that the patient position is verified daily in a fractionated treatment regime.

Recently, with the advent of tomotherapy (Mackie et al., 1993), new techniques for treatment verification have been suggested that employ megavoltage computed tomography (MVCT), and the exit fluence measured by the detector during the treatment in order to provide a 3-D reconstruction of the actual dose distribution that is delivered to the patient. In general the approach of 3-D dose reconstruction can be used if the 3-D CT anatomy of the patient in the treatment position and the incident fluence on the patient during the treatment delivery are known (Kapatoes et al., 2001). The incident fluence is obtained by back-projecting the exit fluence measured by detector, and correcting for scattered radiation in the patient and the spatial spread in the detector. Using this knowledge, the delivery can be modified during a fraction or before the next fraction to compensate for the detected set-up and/or dose delivery errors. The ultimate goal in radiation treatment is image guided radiotherapy. This technique of image guided radiotherapy closes the loop on planning, delivery and verification (Keller et al., 2002).

## **2.3 Imaging Devices**

Because of the overwhelming need for accurate knowledge of patient set-up, positions of the PTV and the critical organs relative to treatment beams, and verification of radiation treatment, many methods have been developed to provide radiological images of the patient in the treatment position.

### **2.3.1 Portal Films**

In this method, a radiographic film image of the patient is obtained using the megavoltage (MV) cone beam from a linear accelerator. The use of portal films can be divided into two categories: localization and verification. Localization films only use a high speed film and a fraction of the treatment beam for imaging. Verification films are slow responding and are exposed during the entire time of a treatment fraction; the treatment does not have to be interrupted for the film to be removed. In the case of localization, the film is irradiated using double exposure. The first exposure field size is generally 5 to 10 cm larger than the prescribed treatment beam with the entire beam shaping accessories removed. The second exposure is taken with the field size and field shaping accessories in position for treatment. For small treatment fields where there is very little anatomy visible, this is useful because it shows the edges of the treatment field relative to the patient anatomy (Munro, 1999).

Portal films generally require relatively high exposures and wet chemical processing to obtain images. Another problem with portal films is their high cost and storage issues. Also in the case of localization films, one has to wait until the film is developed before the treatment can be continued (Shalev, 1996).

The frequent use of portal films is recommended for uncooperative patients, treatment of sites that require geometrical accuracy of up to 4 mm, difficult set ups, paediatric patients and where the matching of the field edges is absolutely necessary (Munro, 1999).

### **2.3.2 Electronic Portal Imaging Devices (EPIDs)**

EPIDs in their most general form are electronic alternatives to portal films. Three kinds of electronic portal imagers are common: matrix ion chamber, TV camera based EPIDS and flat panel EPIDS (Munro, 1999). While portal films are generally viewed by the radiation oncologist to verify the treatment set up, EPID images are also viewed by the radiation therapists in many centres. In this way the use of portal imaging expands to helping radiation therapists improve their treatment techniques and patient set up (Munro, 1999).

Besides their use for set up verification, EPIDs are also used as a quantitative method of comparing two different set up techniques for one treatment. EPIDs offer great promise for adaptive radiotherapy. Currently if an error in patient set up is detected, the position of the patient is adjusted for the remainder of the treatment fractions. Another promise of EPIDs is online viewing of the image where the errors in the patient positioning are corrected before the main part of the daily fraction is given to the patient. This technique, in its ideal form would have the portal imager send a signal to the accelerator to interrupt the treatment once enough radiation has been received for imaging. An image registration program quantifies the errors in the patient positioning. The registration program then sends a message to the linear accelerator to either move the couch to reposition the patient, or just continue the dose delivery. EPIDs can also be used to monitor the position of an MLC during dynamic MLC treatments.

This way the treatment is interrupted should there be a discrepancy between the actual leaf movements and the prescribed pattern (Munro, 1999).

The problem with portal imaging for set up verification is that it is a two-dimensional projection technique. Therefore, it inherently superimposes the information along the beam path to produce two-dimensional images in the plane perpendicular to the beam. This results in poor low contrast resolution due to structural noise that comes from adding the images of different structures on top of each other.

### **2.3.3 3-D Computed Tomography for Set up Verification**

Computed tomography allows 3-D viewing of the patient anatomy slice by slice. CT acquires transmission data at various angles around the patient using a collimated fan beam of x-rays. If an adequate number of projection angles consisting of accurate transmission data are measured, then a tomographic image of the patient can be reconstructed using the mathematical technique of filtered back projection (Shepp and Logan, 1974). The process is repeated at several longitudinal locations obtaining a collection of contiguous images to provide 3-D information of radiological anatomy of the patient. Each pixel in the reconstructed CT image represents the average linear attenuation coefficient of the tissues present in that voxel. Since the linear attenuation coefficient depends on the x-ray spectrum used for imaging, a standardization of pixel values is performed to give similar image intensity from one CT system to another. Therefore, the displayed pixels are integers (CT numbers) representing the normalized attenuation coefficient of body tissue relative to that of water according to the following relationship:

$$CT(x, y) = 1000 \frac{\mu(x, y) - \mu_{water}}{\mu_{water}} \quad (2.1)$$

where  $\mu(x, y)$  is the average linear attenuation coefficient of tissue in the voxel located at  $(x, y)$ ,  $\mu_{water}$  is the linear attenuation coefficient of water for the imaging beam, and  $CT(x, y)$  is the CT number or Hounsfield number used to display each pixel (Bushberg et al., 2002).

Besides their proposed use for treatment set up verification and dose reconstruction, CT scanners are very commonly used both for diagnostic imaging and in radiation treatment planning. CT images do not have the rich spatial resolution offered by planar imaging devices such as radiographs; this disadvantage is counterbalanced by the fact that CT images provide greatly improved low contrast resolution and true 3-D information about the anatomy. Moreover, in CT images, unlike planar images, the structures are not superimposed on top of each other (Berndt, 2002).

Although 3-D imaging is possible both at kilovoltage (kV) and megavoltage (MV) energies, kVCT images offer superior spatial and low contrast resolutions. A clinically useful CT scanner has fine high contrast spatial resolution, good soft tissue contrast and uses low radiation dose. High contrast resolution is not as important as soft tissue contrast for the purpose of verifying the patient positioning.

#### **2.4 CT Imaging Options Available in Treatment Position**

At the time of writing this thesis, three different 3-D CT imaging options are available in treatment position. A brief description of these devices is given as follows.

#### **2.4.1 Linear Accelerator plus Diagnostic kVCT Scanner**

This unit combines a conventional C-arm linear accelerator used for treatment and a conventional kV diagnostic CT scanner. Both instruments share the same room and the same patient couch. The linear accelerator and the CT scanner are placed at the opposite ends of the couch. This way, rotating the couch by 180° enables using either the CT scanner or the linear accelerator. The axes of rotation of the linear accelerator and CT system are parallel to each other. The position of the isocenter of the linear accelerator is the same as the origin of the CT coordinate system, once the couch is rotated 180 degrees. The positional accuracy of the common couch is reported to be 0.2, 0.18, and 0.39 mm in the lateral, longitudinal, and vertical directions respectively. This way the scan-position accuracy of the CT gantry is less than 0.4 mm in these three dimensions. In this system, instead of the patient couch moving longitudinally into the CT scanner, as is done with conventional CT scanners, the CT gantry itself moves into the couch (Kuriyama et al., 2003).

Although this imaging option is the best as a state-of-the-art CT system is available within the treatment room, it poses a great financial burden on many cancer clinics. Besides the cost of purchasing and installing the unit, the change in the geometry of the existing treatment rooms has to be considered when purchasing this unit.

#### **2.4.2 Linear Accelerator plus kV Cone Beam CT**

The second option combines a kV cone beam CT scanner with a linear accelerator. A retractable x-ray tube is placed at 90 degrees to the linear accelerator head; the treatment head and the x-ray tube share the same gantry. This unit is capable of radiography, fluoroscopy and cone beam computed



tomography. A large area indirect active matrix flat panel detector is placed opposite to the x-ray tube and rotates as the gantry rotates. A single computer is used for detector calibration, image data acquisition, processing and cone beam CT reconstruction. Cone beam CT using this approach involves taking multiple images, i.e. the cone beam projections, at different angles as the gantry moves through a 360 degree angle. Filtered back projection, modified for the cone beam geometry (Feldkamp et al., 1984) is then used to get 3-D images. High spatial resolution in 3-D was reported for this system. This system is proposed as a good candidate for high-precision image-guided radiotherapy (Jaffray et al., 2002). There are a number of issues that need further attention in order to remove artefacts due to scattered radiation (Endo et al., 2001), and lag and ghosting in the amorphous silicon photodiode array (Siewerdsen et al., 1999). Since the detector used in the reported literature is not optimized for CT imaging and source to detector distance is large to maintain the C-arm geometry of linear accelerator, the low contrast resolution performance of this system could be improved.

### **2.4.3 MVCT**

For many years megavoltage imaging has been proposed as a method of verifying the patient positioning during radiotherapy. This method of imaging is discussed in detail in the next section.

#### **2.4.3.1 History**

The first MVCT system was developed at the University of Arizona in the early 1980's (Simpson et al., 1982). In this system, an array of plastic scintillators was placed opposite to the treatment head on a 4MV Varian linear accelerator to create a third generation CT scanner. The goals of this system were to provide 2D or 3D maps of electron density distribution for treatment planning, verify patient

set up, and provide a 3D means of checking the treatment conformation according to the plan. This prototype was able to give a spatial resolution of 4 mm and determine an electron density difference of less than 1% (Simpson et al., 1982). Since its original description, this scanner has been modified many times. An upgraded version of this scanner was used in Royal Marsden Hospital in the UK (Lewis et al, 1992). This version used a Philips SL25 linear accelerator and 124 BGO scintillation crystals of size 5 x 20 x 50 mm<sup>3</sup> in contact with silicon photodiodes. These detectors are placed on the gantry of linear accelerator opposite to the treatment head and beam is collimated to fan beam geometry. The system is reported to provide a low contrast (i.e. difference in signal among objects with similar attenuation properties relative to the background signal) resolution of 5% for a dose of 9 cGy (ignoring the in-plane and out of plane scattered radiation) per rotation. Another version of this scanner employs a two dimensional array of optically isolated CsI(Tl) crystals viewed by a lens and a CCD camera. The size of each crystal is of 3 x 3 x 10 mm<sup>3</sup>. This detector was developed for cone-beam MVCT with the purpose of treatment verification in conformal radiotherapy. The quantum efficiency of this detector is about 18% for a 6 MV x-ray photon beam. This detector allows a low contrast resolution of 2% with a dose of 40 cGy, and a high contrast spatial resolution of about 2.5 mm (Mosleh-Shirazi et al., 1998). Perhaps, the main drawback of this system is that there is a significant loss of optical photons in the optical chain connecting the scintillation detector array to the CCD camera.

Ford et al. (2002) have made an attempt to perform dose reconstruction using an EPID and cone-beam CT imaging with MV photons from a linear accelerator. The detector used in this system is an indirect detection active matrix flat panel imager using 340 micron thick gadolinium oxysulfide scintillation screen illuminating a 2-D array of amorphous-silicon photo-diodes. The pixel size

was  $0.76 \times 0.76 \text{ mm}^2$ . A low contrast resolution of 2% at 200 cGy with 100 cone beam projections was reported.

The helical tomotherapy unit described in section 2.1.1 has on board MVCT. The MV detector, an array of high-pressure xenon gas cavities (Bushberg et al., 2002), is placed opposite to the fan-beam of MV photons collimated by a computer controlled multileaf collimator. In a xenon gas detector, the electronic charge is generated in the xenon gas cavity that has very poor quantum efficiency at MV photon energy. However, the primary photons interact mainly with the tungsten septa plates. The electrons released and the low energy scattered photons produced from these interactions are readily attenuated in xenon gas, and increase the quantum efficiency of this detector. The CT images from this system are used for patient set up verification and as such an image registration between the MVCT and the planning CT images is performed prior to each treatment. Dose reconstruction combines the transmission data that is taken during treatment with images of the patient's anatomy to calculate the spatially distributed dose to the patient (Kapatoes et al., 2001). In a typical kVCT scanner, a dose of a few cGy gives soft tissue contrast of the order of 0.5% for objects that have a diameter of 5 mm (Ruchala, 1999). Although a kVCT may provide better low contrast resolution at a lower dose and thus may be a superior imaging tool for the purpose of patient position verification prior to treatment, this technology would add considerably to both cost and engineering difficulty of the unit. Moreover, the inferior quality of MVCT images should still be adequate for the purposes of patient set up verification and dose reconstruction. An advantage of MVCT over kVCT is that, at MV energies, the CT numbers are more linearly related to tissue electron densities. This is because, at MV energies, Compton scattering is the dominant interaction and the Compton cross section depends directly on the electron density. Therefore CT numbers at MV energies are a better measure of the actual linear attenuation coefficients of different tissues for the treatment

beam spectrum. This makes MVCT potentially more accurate for dose calculations and inhomogeneities corrections than kVCT (Ruchala et al., 1999; Keller et al., 2001). Using this system, a low contrast resolution below 2% and spatial resolution of 3 mm with doses ranging from 8 to 12 cGy have been reported (Ruchala et al., 1999).

#### 2.4.3.2 Problems with MVCT

Poor low contrast resolution, high image noise and large dose to the patients are the main problems that are encountered in MV imaging.

- *Poor Soft Tissue Contrast:*

At kilovoltage photon energies (e.g. 60 KeV photons in water), approximately 10% of the photons interact with the tissue through the photoelectric process. (Ruchala et al., 1999). For low atomic number ( $Z$ ) materials, the photoelectric interaction coefficient varies almost proportional to  $Z^{3.8}$  per electron and to  $Z^3$  for high  $Z$  materials (Johns and Cunningham, 1983). Therefore even though the effective atomic numbers of different tissues in the body show small differences (e.g. 7.64 for muscle, 12.31 for bone and 6.46 for fat according to Johns and Cunningham (1983)) the difference in the photoelectric process is significant. This results in rich contrast among different tissue types at kV energies.

The Compton process is much more important than either photoelectric absorption or pair production for photons in the range of 100 keV to 10 MeV. In contrast with photoelectric interactions, Compton interactions are almost independent of atomic numbers of the interacting media. Therefore at MV energies the main reason for tissue contrast would be the density difference, which is not very significant among tissues (e.g. 1040 kg/m<sup>3</sup> for muscle, 1650 kg/m<sup>3</sup> for bone and 916 kg/m<sup>3</sup> for fat) (Johns and Cunningham, 1983).

In conclusion since the contrast among different tissue types depends on the absolute difference among the linear attenuation coefficients and this difference is larger at KV energies, soft tissue contrast is inferior at MV energies compared to kV energies.

- *Higher Image Noise:*

At MV energies, a very small fraction of photons actually interact with the detector. Moreover, interacting photons do not deposit the same amount of energy in the interacting medium. This situation is quite different from kV energies where almost all of the energy of the interacting photons is deposited in the detector (Johns and Cunningham, 1983). Therefore, the quantum efficiency of detectors at MV photon energies is lower; this fact results in higher quantum noise in projection data measurements. Another reason for higher noise in the data is reduction in incident fluence, required to lower the dose deposited in the patient as explained below.

- *High Dose deposited in the Patient:*

Mass absorption coefficients are not very different for the same tissue at kV or MV energies. For example, according to Johns and Cunningham (1983), the mass absorption coefficient of muscle is  $0.0312 \text{ cm}^2/\text{g}$  for 60 keV photons and  $0.0205 \text{ cm}^2/\text{g}$  for 4 MeV photons. This means that the fraction of the energy deposited in the medium is similar at kV and MV energies. However, the absolute value of the energy deposited in the patient is larger at MV energies compared to kV energies (Ruchala et al., 1999).

To overcome this problem, the number of MV photons incident on the detector has to decrease significantly (Ruchala et al., 1999). The problem with using this approach is that it results in an increase in the image noise. Groh et al.

(2002) have derived an approximate relationship between dose (D), signal to noise ratio (SNR), image pixel dimensions ( $\Delta$ ), image slice thickness (T), and quantum efficiency  $\eta$  as follows:

$$D \propto \frac{SNR^2}{\eta \Delta^3 T} \quad (2.2)$$

Therefore, any decrease in dose comes at the cost of image quality degradation either in the shape of decreased SNR, larger pixels, thicker slices or any combination of these factors. In fact, a detector's quantum efficiency is the only parameter that can be improved without affecting the other parameters. It is accepted that an MVCT detector that has optimum quantum efficiency and DQE will result in the lowest image noise for a given patient dose.

## 2.5 Types of Detectors Used in CT Imaging

Common detectors used in CT imaging are gas detectors and scintillation detectors.

### 2.5.1 Gas Detectors

These detectors use xenon gas at high pressures usually about 25 atm. The gas is placed in long thin cells between two collecting electrodes used for applying external electric field for charge collection. The energy deposited by the incident x-ray photons ionizes the gas atoms. Ionic charge is then collected by electrode plates creating currents in the front-end electronics which are proportional to x-ray fluence (Bushberg et al., 2002). This process is demonstrated in Figure 2.1.

Due to the lower density of the gas relative to solid state detectors, the quantum efficiency is very low; however, the temporal response of these detectors is very favourable for fast third generation (Bushberg et al., 2002) kVCT scanners. To compensate for poorer detector efficiency, the detectors are made longer in the beam direction. Also the septa plates can be made very thin to reduce the dead spaces between sensitive elements (i.e. improve geometric efficiency). The geometry of these detectors makes their performance very dependent on the direction of the incident beam (Bushberg et al., 2002). The quantum efficiency of the xenon gas is even poorer at MV photon energies unless the septa plates serve as the primary detector, as in the case of tomotherapy as discussed in section 2.1.1. In modern diagnostic CT systems, these detectors have been largely replaced by fast, stable, more efficient ceramic scintillators that lend themselves well to the multi-row formations used in multi-slice scanners (Bushberg et al., 2002).

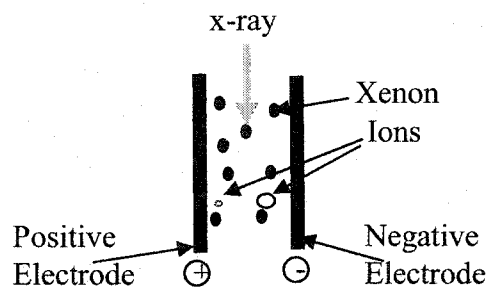


**Figure 2.1:** Xenon Gas Detector: In a xenon gas detector, the x-ray photon ionizes the gas. The ions are collected by electrodes to produce currents proportional to the x-ray fluence.

### 2.5.2 Scintillation Detectors

Scintillation detectors normally consist of a scintillating material in contact with photodiodes. Once the x-rays interact with the scintillation material, they produce many optical photons along their paths. A fraction of these optical photons, i.e. the optical photons that are not absorbed in the crystal bulk or that escape from surfaces, are detected by the photodiodes. This process is illustrated in Figure 2.2.

Since scintillation detectors have a higher atomic number and density than gas detectors, their quantum efficiency is generally higher as well (Bushberg et al., 2002). Scintillation detectors are very popular for third generation CT scanners. Most commercial systems use multiple rows of ceramic (rare earth materials) scintillators coupled to photodiodes to collect projection data for several longitudinal positions on the patient per rotation. Using a combination of pre and post-patient collimators, and electronic addition of the detector signals from various rows, these detector systems are capable of producing multiple tomographic slices that vary from 0.5 mm to 10 mm in thickness. Currently all the multiple array detectors are placed on third generation CT scanners. The implementation of these devices on fourth generation CT scanners would require too many detectors (Bushberg et al., 2002).



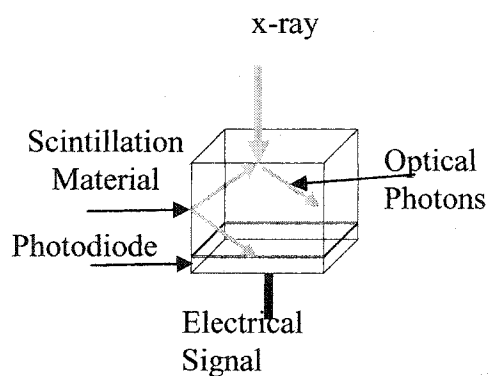


**Figure 2.2:** Scintillation Detector: In a scintillation detector, the interacting x-rays produce optical photons in the material along their paths. A fraction of these optical photons make their way to the photodiodes. If the optical photons are detected by the photodiodes, the result is an electrical signal proportional to the number of detected optical photons.

## References:

- <sup>1</sup> Berndt A.G., "A Fourth Generation 192Ir Source-Based CT scanner for Brachytherapy", PhD thesis, University of Manitoba (2002).
- <sup>2</sup> Bushberg J.T., Seibert J.A., Leidholdt E.M., Boone J.M., *The Essential Physics of Medical Imaging*, (Lippincott Williams & Wilkins, Philadelphia, 2002).
- <sup>3</sup> Carol M.P., "Peacock<sup>TM</sup>: a system for planning and rotational delivery of intensity modulated fields," *Int.J. Img. Sys. Tech.* 6:56-61 (1995).
- <sup>4</sup> Endo M., Tsunoo T., Nakamori N., and Yoshida K., "Effect of scattered radiation on image noise in cone beam CT," *Med. Phys.* 28: 469-474 (2001).
- <sup>5</sup> Feldkamp L.A., Davis L.C., and Kress J.W., "Practical cone-beam algorithm," *J. Opt. Soc. Amer.*, 1: 612-619 (1984).
- <sup>6</sup> Ford E.C., Chang J., Mueller K., Sindhu K., Todor D., Mageras G., Yorke E., Ling C.C., and Amols H., "Cone-beam CT with megavoltage beams and an amorphous silicon electronic portal imaging device : potential for verification of radiotherapy of lung cancer," *Med. Phys.* 29: 2913-2924 (2002).
- <sup>7</sup> Groh B. A., Siewerdsen J. H., Drake D. G., Wong J. W., and Jaffray D. A., " A performance comparison of flat-panel imager-based MV and kV cone-beam CT," *Med. Phys.* 29: 967-975 (2002).
- <sup>8</sup> International Commission on Radiation Units and Measurements, "Prescribing, Recording, and Reporting Photon Beam Therapy," ICRU Report 50, Washington, D. C. (1993).
- <sup>9</sup> International Commission on Radiation Units and Measurements, "Determination of Dose Equivalents Resulting from External Radiation Sources," ICRU Report 39, (1985).
- <sup>10</sup> Jaffray D.A., Siewerdsen J.H., Wong J.W., Martinez A.A., "Flat panel cone-beam computed tomography for image guided radiation therapy," *Int. J. Radiation Oncology Biol. Phys.* 53: 1337-1349 (2002).
- <sup>11</sup> Johns H.E., Cunningham J.R., *The Physics of Radiology*, 4<sup>th</sup> ed. (Thomas, Springfield, IL, 1983).
- <sup>12</sup> Kapatoes J. M., Olivera G. H., Balog J. P., Keller H., Reckwerdt P. J., and Mackie T. R., "On the accuracy and effectiveness of dose reconstruction for tomotherapy," *Phys. Med. Biol.* 46: 943-966 (2001).

- <sup>13</sup> Keller H., Glass M., Hiderer R., Ruchala K., Jeraj R., Olivera G., and Mackie T.R., “ Monte Carlo study of a highly efficient gas ionization detector for megavoltage imaging and image-guided radiotherapy,” *Med. Phys.* 29: 165-175 (2002).
- <sup>14</sup> Kuriyama K., Hiroshi O., Sano N., Komiyama T., Tanaka S., Aikawa Y., Tateda Y., Araki T., Ikenaga S., Umatsu M., “ A new irradiation unit constructed of self-moving gantry-CT and linac,” *Int. J. Radiation Oncology Biol. Phys.* 55: 428-435 (2003).
- <sup>15</sup> Lewis D.G., Swindell W., Morton E.J., Evans P.M., and Xiao Z.R., “ A megavoltage CT scanner for radiotherapy verification,” *Phys. Med. Biol.* 37: 1985-1999 (1992).
- <sup>16</sup> Mackie T. R., Holmes T., Swerdloff S., Reckwerdt P., Deasy J. O., Yang J., Paliwal B., and Kinsella T., “ Tomotherapy: a new concept for the delivery of dynamic conformal radiotherapy,” *Med. Phys.* 20: 1709-1719 ( 1993).
- <sup>17</sup> Mohan R., “Intensity modulated radiotherapy”, in *Teletherapy: Present and Future*, edited by Mackie T.R and Palta J.R. (Advanced Medical Publishing, Madison, WI, 1996), pp.761-793.
- <sup>18</sup> Mosleh-Shirazi M.A., Evans P.M., Swindell W., Webb S., Partridge M., “ A cone-beam Megavoltage CT Scanner for Treatment Verification in Conformal Radiotherapy”, *Radiotherapy and Oncology.* 48: 319-328 (1998).
- <sup>19</sup> Munro P., “Megavoltage radiation for treatment verification”, in *The Modern Technology of Radiation Oncology* , edited by Van Dyk J. (Medical Physics Publishing, Madison, WI, 1999), pp. 481-508.
- <sup>20</sup> Olivera G. H., Shepard D.M., Ruchala K., Aldridge J.S., Kapatoes J., Fitchard E.E., Reckwerdt P. J., Fang G., Balog J., Zachman J., Mackie T. R., “Tomotherapy”, in *The Modern Technology of Radiation Oncology* , edited by Van Dyk J. (Medical Physics Publishing, Madison, WI, 1999),pp. 521-588.
- <sup>21</sup> Ruchala K.J., Olivera G.H., Schloesser E.A., Mackie T.R., “ Megavoltage CT on a tomotherapy system,” *Phys. Med. Biol.* 44: 2597-2621 (1999).
- <sup>22</sup> Shalev S., “Megavoltage portal imaging”, in *Teletherapy: Present and Future*, edited by Mackie T.R and Palta J.R. (Advanced Medical Publishing, Madison, WI, 1996), pp.445-469.
- <sup>23</sup> Shepp L.A. and Logan, B.F., “The Fourier reconstruction of a head section,” *IEEE Trans.Nucl.Sci.*,21:21-43 (1974).

- <sup>24</sup> Simpson R.G., Chen C.T., Grubbs E.A, Swindell W., "A 4-MV CT scanner for radiation therapy: the prototype system," *Med. Phys.* 9: 574-579 (1982).
- <sup>25</sup> Siewerdsen J. H., and Jaffray D. A., "A ghost story: spatial-temporal response characteristics of an indirect-detection flat-panel imager," *Med. Phys.* 26: 1624-1641 (1999).
- <sup>26</sup> Van Dyk J., "Radiation oncology overview", in *The Modern Technology of Radiation Oncology*, edited by Van Dyk J. (Medical Physics Publishing, Madison, WI, 1999), pp.1-19.
- <sup>27</sup> Van Dyk J., Munro P., "Simulators", in *The Modern Technology of Radiation Oncology*, edited by Van Dyk J. (Medical Physics Publishing, Madison, WI, 1999), pp.95-130.
- <sup>28</sup> Webb S., *Intensity-Modulated Radiation Therapy*, Institute of Physics Publishing, (Bristol and Philadelphia, 2001).

## Chapter 3: MATERIALS AND METHODS

In scintillation-photodiode detectors, the x-rays interact with the scintillation material and set electrons in motion. These electrons ionize and excite the scintillation material, which then emits flashes of light. A fraction of the optical energy may reach the photodiodes where it creates additional charge in the depletion layer. The charge produced in the photodiode elements is collected by a charge sensitive amplifier, digitized and stored in a computer for further processing. A scintillation photodiode detector, in its simplest form, contains a scintillation crystal, a photodiode, amplifier, analog-to-digital (A-to-D) converter and a computer. The components of our prototype detector, both the single crystals  $\text{CdWO}_4$  and  $\text{CsI(Tl)}$ , and a  $\text{CdWO}_4$  array, are briefly discussed in this chapter. The prototype electronic hardware is also described.

The interaction of MV photons with the scintillation material and the subsequent transport of optical energy are complex phenomena. Therefore, we have used two different software packages that separately transport x-ray and optical photons through the scintillation material, namely EGSnrc and DETECT2000, respectively. This chapter also discusses the geometry of various crystal and photodiode components, and the associated parameters used for photon transport.

The important imaging characteristics of multi-element detectors are characterized by the spatial frequency dependent modulation transfer function (MTF ( $f$ )), noise power spectrum (NPS( $f$ )) and detective quantum efficiency (DQE( $f$ )). This chapter presents a modified theoretical model to calculate these

parameters using the results of Monte Carlo simulation, and discusses the experiments conducted to measure these functions for the prototype detector.

### 3.1 Single Crystals

We have obtained single crystals of  $\text{CdWO}_4$  and  $\text{CsI(Tl)}$  (Rexon Components, Inc., Beachwood, Oh) of  $0.275 \times 0.8 \text{ cm}^2$  cross section and heights of 0.4, 1.0, 1.2, 1.6, and 2.0 cm. An array of photodiodes (16-element, S5668-02, Hamamatsu Corporation) was used for optical photon detection. The size of each photodiode is  $0.1175 \times 0.2 \text{ cm}^2$ . The single photodiode elements are 0.4 mm apart. Each crystal covers two photodiodes (see Figure 3.2) and each pair of photodiodes is coupled. Therefore each crystal provides one channel detector. A picture of the single elements is shown in Figure 3.1.

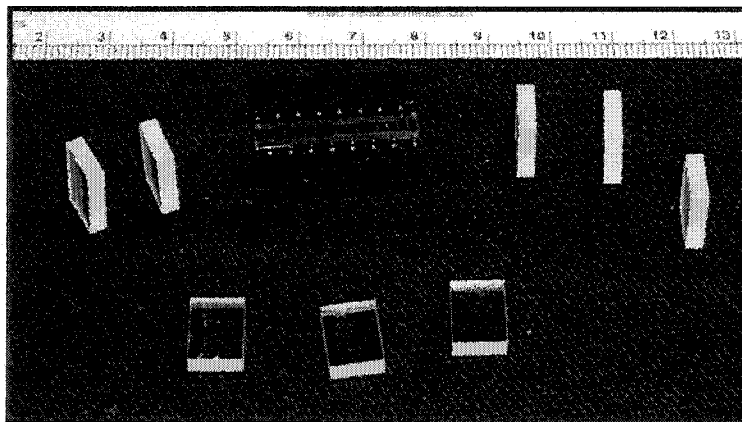


**Figure 3.1:** Photograph of Photodiodes and Single  $\text{CdWO}_4$  Crystals.

### 3.1.1 Choice of Scintillators

There are several scintillating materials available for photon detection. The most common scintillating crystals used in medical imaging applications are NaI(Tl), BGO, CsI(Tl), LSO, ZnWO<sub>4</sub> and CdWO<sub>4</sub>. Selected properties of these detectors are shown in Table 3.1. The density and the attenuation coefficient of a scintillation material determine its x-ray quantum efficiency (i.e. the fraction of incident x-rays which deposit some energy in the detector) for a given spectrum of photons. Generally the higher the density, the larger the x-ray quantum efficiency. Scintillation materials that have higher light yield are desirable since light detection becomes easier. It is also important that there is a reasonable match between the optical emission spectrum of the scintillation material and the sensitivity spectrum of the photodiode. The scintillation material should also be non-hygroscopic so that it does not require complex enclosure and can be easily handled. Afterglow is defined as the fraction of light emitted from the scintillation material after the x-ray exposure has ended. This is generally caused by the longer lasting fluorescence decay of the scintillation material.

NaI(Tl) was not chosen for our work because of its lower density that results in lower x-ray quantum efficiency at MV photon energies. The very low light yield of BGO is its main shortcoming, although it has a reasonably high density. The light output of CsI(Tl) is the largest of the scintillators listed. However, its afterglow, measured at 6 ms after stopping irradiation, could be as high as 5%. The afterglow becomes an important consideration for fast CT imaging. The density of CsI(Tl) at 4.51 g/cm<sup>3</sup> is lower than for CdWO<sub>4</sub> at 7.9 g/cm<sup>3</sup>. These properties are further investigated for CsI(Tl) in section 3.4.2.2 where we measured the afterglow in CdWO<sub>4</sub> and CsI(Tl) crystals. Although ZnWO<sub>4</sub> is almost as dense as CdWO<sub>4</sub>, its light yield is only 67% of CdWO<sub>4</sub>. As seen in Table 3.1, LSO is probably a good candidate for CT application; however,

data regarding its afterglow is not available and the scintillating crystal itself is not readily available (Derenzo and Moses, 1992). Therefore, we have chosen to optimize the detector based on  $\text{CdWO}_4$  and photodiodes for MVCT application, although the capability of the Monte Carlo modeling to predict the signal in scintillation detectors was investigated for both  $\text{CdWO}_4$  and  $\text{CsI(Tl)}$ .

We have obtained individual  $\text{CdWO}_4$  and  $\text{CsI(Tl)}$  crystals (Rexon Components, Inc., Beachwood, Oh) of  $0.275 \times 0.8 \text{ cm}^2$  cross-sectional area and heights of 0.4, 1.0, 1.2, 1.6 and 2.0 cm. These crystals were wrapped in 10 cm long teflon tape on all sides except the one in contact with the photodiodes (16-element, S5668-02, Hamamatsu Corporation). The teflon tape forms a reflective coating that increases the amount of light reaching the photodiode. Each photodiode has a size of  $0.1175 \times 0.2 \text{ cm}^2$ , and two consecutive photodiode elements are 0.04 cm apart. Each crystal covers two consecutive photodiode elements (see Figure 3.2). A bare metal foil found in hobby shops was placed underneath the crystal face exceeding the photodiode area to reflect light back into the crystal. An optical coupling glue compound (Dow Corning 20-057) was placed between the photodiode and scintillation crystals.



**Table 3.1:** Properties of selected  $\gamma$ -ray detecting scintillators (Derenzo and Moses, 1992; Krus et al., 1999)

Crystal	Density (g cm <sup>-3</sup> )	$\mu^{-1}$ (cm) <sup>*</sup>	Hygro- scopic	$\lambda_{\max}$ (nm)	Photons /MeV	After- glow (% at ?ms)
<b>NaI:TI</b>	3.67	3.05	Yes	415	38,000	0.3- 5/6ms
<b>Bi<sub>4</sub>Ge<sub>3</sub>O<sub>12</sub> (BGO)</b>	7.13	1.11	No	480 480	700 7500	0.005/3 ms
<b>CsI(Tl)</b>	4.51	2.43	Slightly	450	59,000	0.5- 5/6ms
<b>Lu<sub>2</sub>SiO<sub>5</sub> (Ce) (LSO)</b>	7.4	1.22	No	420	30,000	-
<b>CdWO<sub>4</sub></b>	7.9	1.21	No	470	15,000	0.1/3ms
<b>ZnWO<sub>4</sub></b>	7.87	1.19	No	480	10,000	-

\* value for 511 keV photons

### 3.2 CdWO<sub>4</sub> Detector Array

This array of detectors was originally used for an <sup>192</sup>Ir-based CT scanner and consists of eight CdWO<sub>4</sub> scintillating crystals (Bicron Corporation) coupled to a 16-element photodiode array (S5668-02, Hamamatsu) with optical glue (Dow Corning 20-057) (Berndt, 2002). Each CdWO<sub>4</sub> crystal has dimensions of 0.275 x 0.8 x 1.0 cm<sup>3</sup>, while each photodiode is 0.1175 cm wide and 0.2 cm long with a 0.04 cm gap between consecutive elements. Therefore, each crystal covers exactly two photodiodes in the width (0.1175 cm) direction. The eight crystals are bonded together with white gelcoat (Ashland Chemical Type 1 polyester). The crystal dimension along 0.8 cm length could be the same as that of photodiode elements (i.e. 0.2 cm). However, this is not desirable since the x-ray beam width in the longitudinal (i.e. slice thickness) direction is almost always larger than 0.2 cm. Photodiode arrays that can be abutted to form a larger detector array and that are longer than 0.2 cm in base dimension are not commercially available. We have placed a bare metal foil, available from hobby shops, underneath the crystal area that exceeds the photodiode area. This foil acts as a rough yet nearly perfect reflector for the optical photons and increases the amount of light reaching the photodiodes (Berndt, 2002). Optical coupling glue was placed atop the photodiode elements, similar to the single crystals.

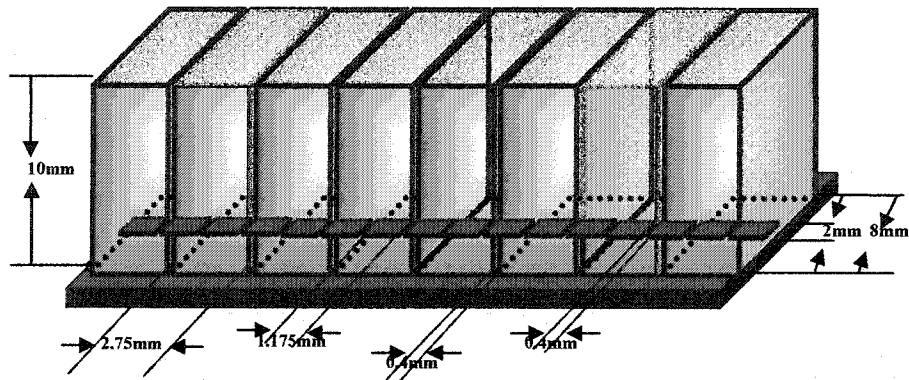


**Figure 3.2:** The Geometry of our CdWO<sub>4</sub> Detector: As shown, the dimensions of each crystal are 2.75 x 8 x 10 mm<sup>3</sup>. Two consecutive crystals are 0.4 mm apart. Each crystal is in contact with two photodiodes. The size of each photodiode is 1.175 x 2 mm<sup>2</sup>; the spacing between two photodiodes is 0.4 mm. Each adjacent pair of photodiodes in contact with one crystal is coupled to give one signal per crystal.

### 3.2.1 Detector Electronics

Our prototype detector consists of three different circuit boards: the detector assembly board, a data acquisition control circuit board and an analog-to-digital (A-to-D) converter board. These three components are shown in Figure 3.3. The output of the detector assembly board is eight time multiplexed voltages, each representing the reading of one scintillator. Four electronic signals regulate the various functions that are performed by the detector assembly board and the A-to-D board. These are the integrate-discharge ( $\bar{I}/D$ ) signal, the sample and hold ( $\bar{S}/H$ ) signal, the multiplexer (MUX) lines, and the external convert (E.C.) clock. A more detailed description of the different components of the detector electronics is given in the following sections.

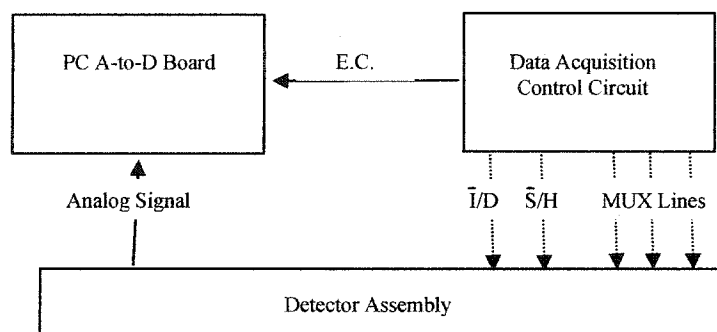


**Figure 3.3:** The Detector Electronics Schematics: The dashed lines indicate the presence of opto-isolators. E.C : External Convert Clock,  $\bar{I}/D$  : Integrate/Discharge signal,  $\bar{S}/H$  : Sample and hold signal.

### 3.2.1.1 Detector Assembly Board Components

The components of the detector assembly board for one channel are shown in Figure 3.4. Notice that the gain and filter stage is not the same between the linear accelerator and the  $\text{Co}^{60}$  boards. The reason for this difference is discussed in sub-section iii. Moreover, the timing sequences (shown in Figures 3.6 and 3.7) are also different between the  $\text{Co}^{60}$  and the linear accelerator board. The reason for this difference is discussed in section 3.2.1.3. The detector consists of eight channels. The detector assembly components for each channel include: two photodiodes (S5668-02, Hamamatsu); an integrator (TL074C ,Texas Instruments op-amp; DG442, Temic Analogue Switch); a gain and filter stage (gain for  $\text{Co}^{60}$  = 47, gain for linac = 4.7,  $f_c$  (i.e. cut off frequency) for  $\text{Co}^{60}$  = 339Hz); a sample and hold circuit (Analog Devices SMP-04); and then an 8-to-1 multiplexer (MUX) (Motorola MC14051B). The photodiodes produce a current,  $i_{\text{photo}}$ , which

is proportional to the  $\gamma$ -ray fluence incident on their corresponding crystals. This current then goes through the integrator which accumulates the charge created by  $i_{\text{photo}}$  for a time  $\Delta T$  and produces a voltage signal linearly proportional to the product of average  $i_{\text{photo}}$  and  $\Delta T$ . This voltage is then low pass filtered and magnified in the gain and filter stage. The sample and hold stage, holds the signal for a period of time. In this period of time the 8-to-1 MUX sends the output of the channels to the A-to-D converter board one by one. This way, the output of all the channels is sampled at the same instant in time. The voltage signals are digitized to 16-bit precision by the A-to-D converter (National Instruments, PCI-MIO-16XE-50). The acquisition software is written in LabView (National Instruments). The analogue signal processing electronics for the detector receive their timing signals from the data acquisition control circuit via opto-isolators (Motorola H11L1) to eliminate interference noise. Different components of the detector assembly board are discussed individually in the following sub-sections: i, ii, iii and iv.

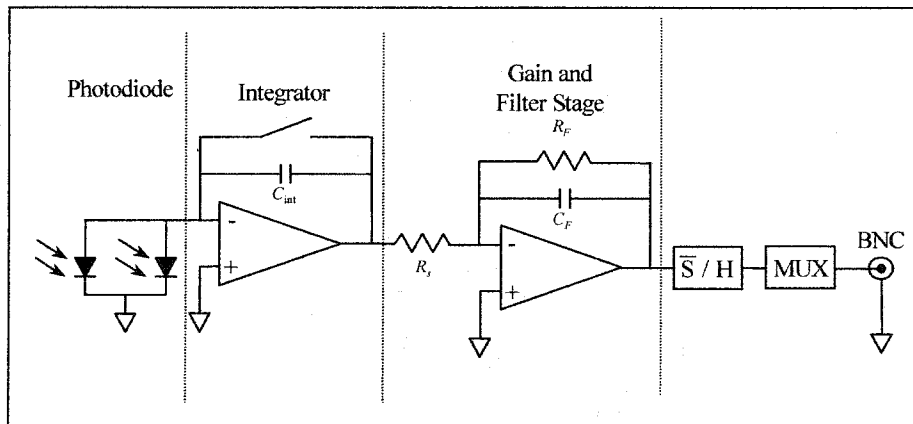


**Figure 3.4:** Circuit Diagram Showing the Detector Assembly Board Components: In the  $\text{Co}^{60}$  board  $C_{\text{int}}=1$  nF,  $R_s=1$  k $\Omega$ ,  $C_f=10$  nF,  $R_f=47$  k $\Omega$ . The components are the same in the linac board with the exception that  $R_f$  is 4.7 k $\Omega$  instead of 47 k $\Omega$ , and feed back capacitor  $C_f$  is not used.

## i. Photodiodes

The process by which the silicon photodiodes operate can be easily understood via the physics of semiconductor electronics. To control the number of charge carriers in semiconductors, they are usually doped with impurities. Elements from column III of the periodic table produce more holes by accepting electrons from the semiconductors; whereas elements from column V donate electrons thereby producing an excess of free electrons. The first group of semiconductors is called p-type (acceptors) and the latter, n-type (donors). The point of contact of a p-type and an n-type material is called a pn junction. In a small region around the pn junction, the electrons and holes recombine and leave no free charges. The lack of free electrons leaves the n-type material positively charged; similarly the lack of holes leaves the p-type material negatively charged. This region is called the depletion region and is shown in figure 3.5a. In the presence of external voltage,  $V_B$ , two types of currents flow in the pn junction material. The first one is diffusion current,  $I_d$ , flowing from the p-type material to the n-type material. In order for the diffusion current to occur, the electrons and holes must have enough thermal energy to overcome the depletion region barrier. The second current is called reverse saturation current,  $I_0$ , and flows from the positive side of the depletion region to the negative side. If a positive voltage is connected to the p-type semiconductor and a negative voltage to the n-type, the semiconductor circuit is called forward biased; when the negative voltage is connected to the p-type and the positive to the n-type, the circuit is called reversed biased. In a forward-biased circuit, the total current is given by:

$$i_{total} = I_d - I_0 \quad (3.1)$$

In a reverse-biased circuit, the depletion region is too large for the diffusion current to flow. Therefore the total current is given by:

$$i_{total} = -I_0 \quad (3.2)$$

When optical photons hit the depletion region of a pn junction, they cause additional current flow through the semiconductor in the direction of the reverse saturation current. This phenomenon is the basis for the operation of photodiodes. This additional current is called  $i_{photo}$ . In the case of photodiode operation, equations 3.1 and 3.2 still apply with the modification that  $I_0$  is equal to the sum of  $I_0$  and  $i_{photo}$ . If no external voltage is provided but optical light is present, the only current going through the photodiode is  $i_{photo}$ . The three modes of operation of a photodiode are shown in Figure 3.5b-d. The i-v characteristic curve of a photodiode is shown in Figure 3.5e. As shown in this figure, the response of the photodiode is linear if it is operated in reverse-biased mode or with no external voltage (Rizzoni, 2000). In these regions, the increase in reverse saturation current is directly proportional to the incident optical energy  $\phi_{light}$ . Even though operating a photodiode in reverse-bias voltage mode has the advantage of increased sensitivity due to the large size of the depletion region, the statistical (shot) noise in  $i_{total}$  is high. Therefore, our photodiodes were operated with no external voltage.

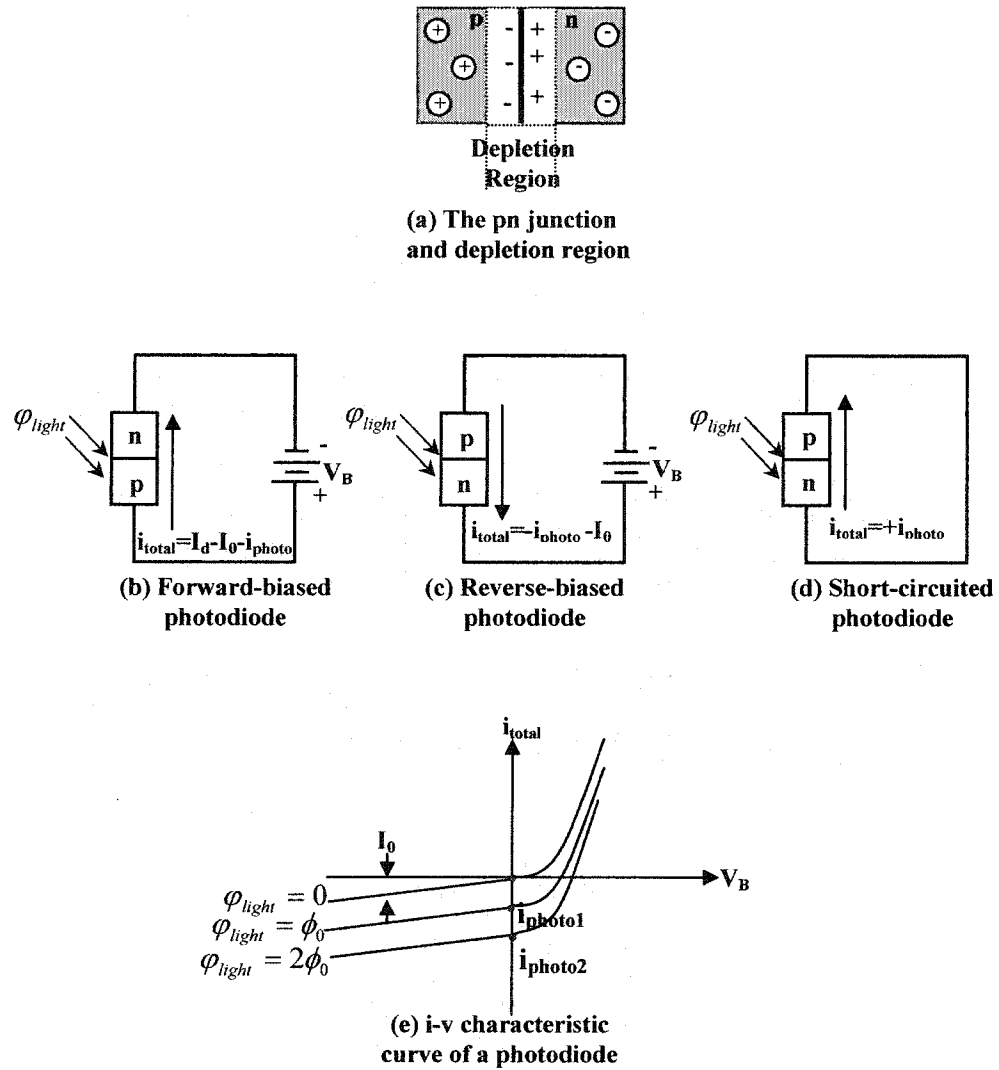


**Figure 3.5:** The Basis of Operation of Photodiodes: (a) a pn junction. (b)-(d) a photodiode operating in forward-biased, reverse-biased and short-circuited mode respectively. (e) the i-v characteristic curve of a photodiode.



## ii. Integrator

The gated integrator accumulates  $i_{\text{photo}}$  for a time  $\Delta T$  and produces a voltage signal that is linearly proportional to the product of average  $i_{\text{photo}}$  and  $\Delta T$ . The integrator is made up of a low noise JFET operational amplifier, a 1nF capacitor and an analogue reset switch as shown in Figure 3.4. When the switch is opened, the charge accumulates on the capacitor and when the switch is closed, the capacitor is discharged. For an ideal integrator the output voltage  $\Delta V_{\text{total}}$  in a  $\text{Co}^{60}$  beam is given by:

$$\Delta V_{\text{total}} = \frac{G}{C_{\text{int}}} \int_0^{T_0 - 0.3\text{ms}} (i_{\text{photo}} + i_D) dt \quad (3.3)$$

where  $i_{\text{photo}}$  is the photocurrent;  $C_{\text{int}}$  is the capacitance in the feed-back loop;  $G$  is the gain of the gain-and-filter stage;  $T_0$  is the sampling period;  $i_D$  is the sum of the op-amp input bias current and the switch leakage current. A time of 0.3 ms is subtracted from  $T_0$  and represents the times during which either the integrated voltage does not appear at the sample and hold circuit output, or the capacitor is being discharged (see Figure 3.6) in section 3.2.1.3. Assuming that  $i_D$  is constant during a sampling period, the dark voltage  $\Delta V_D$  which is present in the absence of light can be calculated using the following equation:

$$\Delta V_D = i_D G (T_0 - 0.3\text{ms}) / C_{\text{int}} = i_D G \Delta T / C_{\text{int}} \quad (3.4)$$

where  $\Delta T$  is the integration time. For acquiring data in a continuous radiation beam (i.e.  $\text{Co}^{60}$ ),  $T_0$  is obtained by dividing a free running 1 MHz clock and selected by dip switch settings. The dark voltage has been subtracted from all experimental voltage measurements reported in this thesis. Assuming that  $i_{\text{photo}}$  is

constant during a sampling period, the dark corrected voltage produced in the presence of light is calculated using the following equation:

$$\Delta V = i_{photo} G(T_0 - 0.3ms) / C_{int} = i_{photo} G\Delta T / C_{int} \quad (3.5)$$

In the case of a pulsed beam from a linear accelerator, the switch is opened immediately after the synchronization pulse of the linear accelerator occurs. The integration time for the pulsed radiation case is fixed at 0.7 ms, although it could be as low as several tens of  $\mu$ s. It should be noted that equation (3.5) is only applicable to the continuous radiation case. For pulsed radiation, the radiation occurs for a short period of time within each cycle (180 Hz). The integration time  $\Delta T$  could be made equal to the radiation pulse width duration during each cycle. This was not implemented in practice since the radiation pulse width is known to change from one system to another.

### iii. Gain and Filter Stage

The reason for using this stage is to amplify the output voltage of the integrator and low-pass filter it to get rid of some of the high frequency noise. It is important to choose the right cut-off frequency for this filter to reduce the electronic noise and, at the same time, not compromise the temporal response. The output of a gain and low-pass filter is given by:

$$V_{out} = -\frac{R_F}{R_s} V_0 (1 - e^{-t/\tau}) \quad (3.6)$$

where  $\tau = R_F C_F$ . The cut-off frequency of the filter for the continuous radiation case is given by:

$$f_c = \frac{1}{2\pi R_f C_F} = \frac{1}{2\pi(47k\Omega)(1nF)} = 339Hz \quad (3.7)$$

The reason for choosing  $\tau = 47 \mu s$  is that after a delay of  $5\tau = 0.235 ms$ , the magnitude of  $V_{out}$  is  $>0.99 \frac{R_F}{R_s} V_0$ . This means that the detector signal settles down in 0.235 ms, and sampling intervals as short as 0.5 ms can be used.

In the case of pulsed radiation, the dose per pulse is significantly higher than the instantaneous dose rate of  $Co^{60}$ . Therefore, the gain of this stage was reduced by a factor of 10 to 4.7 to avoid saturation, and the filter was removed to further improve the temporal response

#### iv. Sample and Hold Stage

The output of the gain-and-filter stage is determined by  $i_{photo}$  and  $\Delta T$ . However, the integration time must be the same for all the channels. So, the sample and hold circuit holds the output of all the channels at the same instant in time to keep the integration time identical for all of them. The 8-to-1 MUX sends these signals to the A-to-D board via an analog coaxial cable. There, these signals are converted to a 16-bit signal and held in the computer memory.

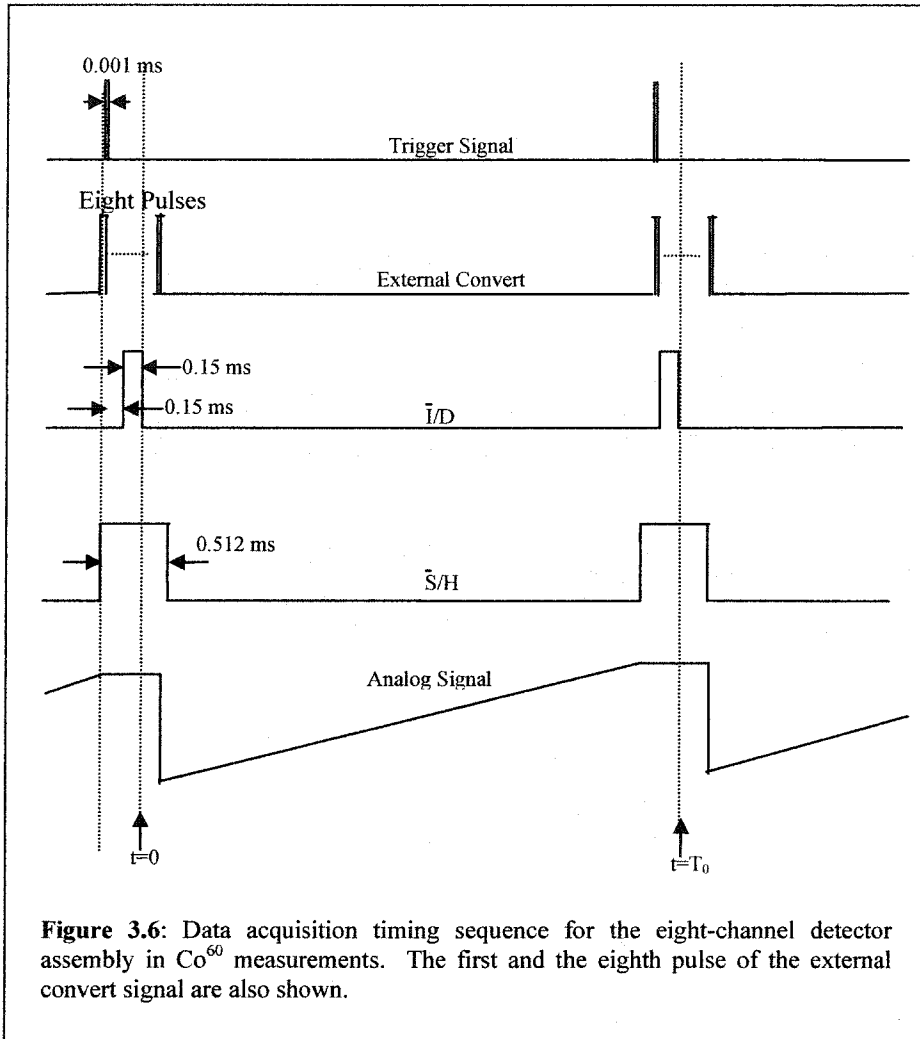
#### 3.2.1.2 Data Acquisition Control Circuits

The purpose of this board is to generate control signals for the gated integrator, the sample and hold, the MUX, and the A-to-D converter. The sampling frequency is obtained by dividing a stand alone 1MHz clock by a 20-bit binary counter, realized by cascading five synchronous 4-bit counters (Texas Instruments 74LS161). The higher 16 bits of this counter can be set via dip

switches to change the sampling frequency. The output of this is a trigger signal that initiates the generation of the other control signals. These control signals include an external control signal for the A-to-D converter (external convert signal), an integrate/discharge ( $\bar{I}/D$ ) signal, a sample and hold signal ( $\bar{S}/H$ ) and finally three binary control lines for the 8-to-1 analog MUX.

### 3.2.1.3 Data Acquisition Sequence

The data acquisition sequence for the board used in  $\text{Co}^{60}$  measurements is shown in Figure 3.6. The combination of the 1 MHz clock and the 4-bit counters produces trigger pulses (pulse width = 1  $\mu\text{s}$ ) at a frequency chosen by the user via dip switches. The data acquisition cycle starts 0.3 ms after the trigger signal comes on; this point is marked as  $t=0$  in Figure 3.6. At this time the capacitor in the integrator circuit is fully discharged; the  $\bar{I}/D$  (The bar over the "I" in  $\bar{I}/D$  indicates that integration occurs when the signal is low, and discharge occurs when the signal is high) is low (switch open), therefore charge begins to accumulate on the capacitor. The charge accumulation continues till  $t = (T_0 - 0.15 \text{ ms})$ . At this time, the capacitor is discharged by closing the switch for a period of 0.15 ms. Therefore, at  $t = T_0$  the integrator circuit is ready for the next cycle. At  $t = 0.212 \text{ ms}$ , the  $\bar{S}/H$  (The bar over the "S" in  $\bar{S}/H$  indicates that sampling occurs when the signal is low, and holding when it is high) signal starts sampling. Sampling continues till  $t = (T_0 - 0.3 \text{ ms})$ . The  $\bar{S}/H$  signal is high for 0.512 ms starting at  $t = (T_0 - 0.3) \text{ ms}$ . During this holding period, the three MUX control lines generate a 3-bit number between 0 and 7 that determines which channel is read during each external convert pulse by the A-to-D converter. The eight external convert pulses come on shortly after the next trigger signal comes on. The three MUX control lines and the external convert signals are pulsed synchronously. The waveform at the bottom of Figure 3.6 shows the output of a given detector at the input of multiplexer.



The output of linear accelerators is not continuous; rather the x-rays are delivered in pulses. Therefore for the linear accelerator measurements, we were not able to use the same timing board as the one used in  $\text{Co}^{60}$ . Consider integrating the detector signal for 0.7 ms at two instances in time. During the first integration cycle we may integrate two pulses of radiation, as opposed to possibly three pulses in the next integration cycle. Therefore, it was necessary to change the timing board for the linear accelerator radiation readings.

The data acquisition sequence for the board used in 6 MV measurements is shown in Figure 3.7. In this case the sync pulse from the linear accelerator (180 Hz) is chosen as the trigger. The radiation comes on 2-3  $\mu\text{s}$  after the sync pulse comes on and lasts for 5-6  $\mu\text{s}$ . The data acquisition cycle starts almost immediately after the trigger signal comes on; this point is marked as  $t=0$  in Figure 3.7. The capacitor in the integrator circuit has been fully discharged and the  $\bar{I}/D$  is set to low, therefore, charge is accumulating on the capacitor. The charge accumulation continues till  $t = 0.8$  ms when the capacitor is discharged. Just before discharging the capacitor at  $t = 0.7$  ms, the  $\bar{S}/H$  signal is set to high to hold the integrated voltage for 0.4 ms. During this holding interval, the three MUX control signals are generated synchronously with the external convert pulses (20 KHz). The waveform at the bottom of Figure 3.7 shows the output of the sample and hold chip which is the signal being sent to the A-to-D converter via the coaxial cable.

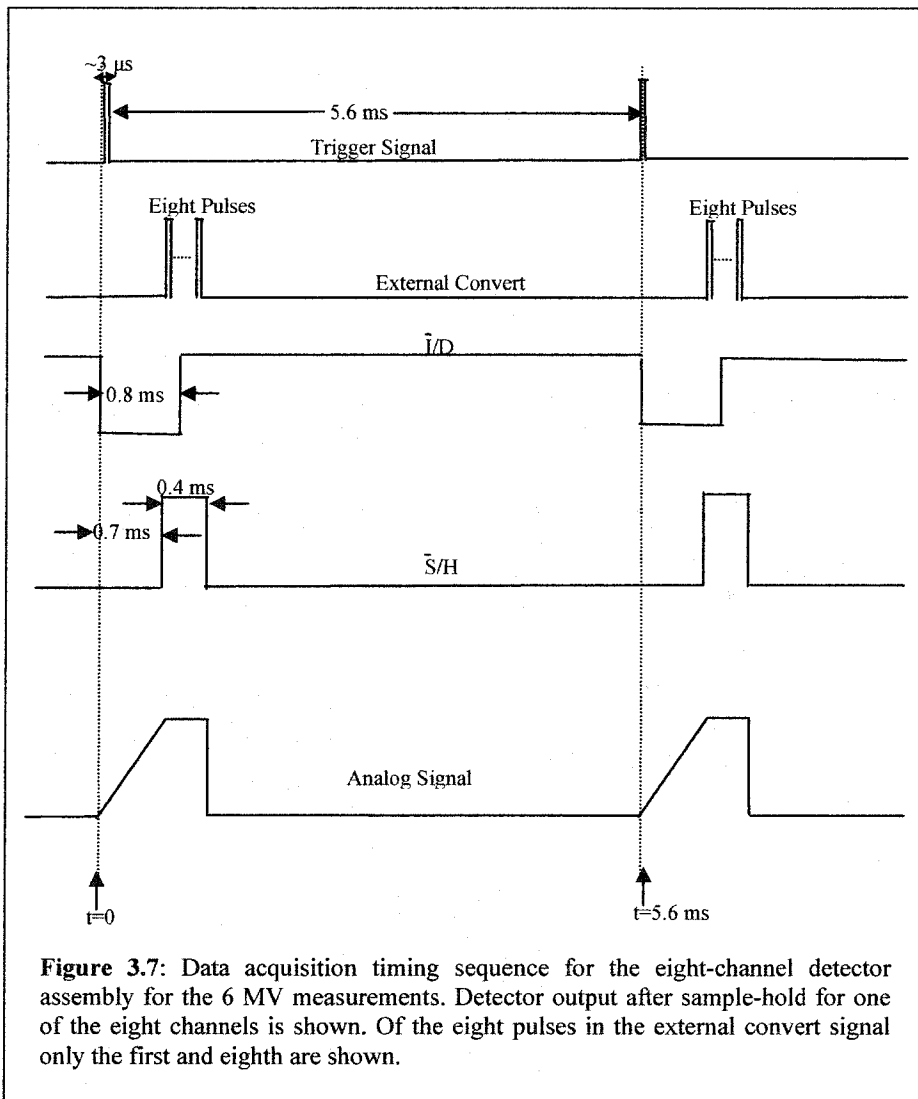


**Figure 3.7:** Data acquisition timing sequence for the eight-channel detector assembly for the 6 MV measurements. Detector output after sample-hold for one of the eight channels is shown. Of the eight pulses in the external convert signal only the first and eighth are shown.

### 3.3 Software Tools

We employed two separate Monte Carlo codes for simulating the response of the single crystals and the detector array to  $\gamma$ -rays. EGSnrc (Kawrakow and Rogers, 2002) was employed for modeling the high energy photon interactions in the crystals. DETECT2000 ([www.gel.ulaval.ca/detect](http://www.gel.ulaval.ca/detect)) was used for predicting the fate of the optical photons created in the crystals.

#### 3.3.1 EGSnrc

We used the electron gamma shower code (EGSnrc) for simulating the interaction of x-rays in the MeV range. EGSnrc is a general purpose code for Monte Carlo simulation of electron and photon transport in different media. The interaction of photons with surrounding matter occurs via four different processes: photoelectric absorption, Rayleigh or coherent scattering, Compton or incoherent scattering and pair production. Specifically DOSXYZnrc was used; this is a general purpose user code for simulating Cartesian coordinate dose deposition.

- *Photoelectric Absorption:*

In this process, a photon collides with an atom and ejects one of the bound electrons from it. This ejected electron is called a photoelectron with energy equal to the energy of original photon minus its own binding energy. The atom is left in an excited state and emits characteristic radiation and/or Auger electrons (Auger electrons carry away the extra energy of an excited atom) until it is returned to its ground state. The photoelectric cross section varies with photon energy approximately as  $1/(h\nu)^3$ , where  $h\nu$  is the photon energy (Johns and Cunningham, 1983).



- *Rayleigh or Coherent Scattering:*

As photons pass over an atom, the electric field component of their electromagnetic wave momentarily vibrates the electrons in the atom. These electrons then emit radiation with the same wavelength as the incident radiation. Since the scattering waves from different atoms combine with each other, this process is called coherent scattering. The cross section for Rayleigh scattering decreases rapidly as the energy of the incident photons increases and is almost negligible for energies greater than 100 keV in low atomic number materials (Johns and Cunningham, 1983). This process does not contribute to energy deposition in the medium.

- *Compton or Incoherent Scattering:*

In this case radiation interacts with a single electron. Some of the incident photon's energy is transferred to the kinetic energy of the electron and the rest is given to the scattered photon. Both the energy and momentum are conserved at the point of interaction, thus, the initial angle of the electron set in motion and the photon path are easily determined. In soft tissue Compton is the most important interaction in the photon energy range of 100 keV to 10 MeV. (Johns and Cunningham, 1983).

- *Pair Production:*

This process is only possible if the energy of the incident photon is greater than 1.02 MeV. The cross section for this interaction increases rapidly with energy above this threshold. If photons pass near the nucleus of an atom, the field of the nucleus may break the photon into a positron and an electron (an example of conversion of energy into mass). Occasionally, this process occurs in the field of an electron, in which case it is called triplet production. The cross section for pair production process increases as the energy of the incident photon increases. (Johns and Cunningham, 1983).

Charged particles, namely positrons and electrons, lose their energy in a medium by two different processes: inelastic collision with atomic electrons and radiation.

- *Inelastic Collisions with Atomic Electrons:*

In these types of collisions, some kinetic energy of charged particles is transferred to the electrons. This transfer of energy leads to the excitation of atoms. These excited atoms then return to their ground state via the emission of characteristic photons and/or Auger electrons. (Kawrakow and Rogers, 2002).

- *Radiation:*

Radiative energy losses occur in the form of annihilation for positrons and bremsstrahlung for electrons. Bremsstrahlung becomes the more important process as the energy of the electrons increase. Bremsstrahlung refers to radiation produced as a result of the decelerating of electrons (Johns and Cunningham, 1983). Once a positron finally comes to rest, it is annihilated by combining with a free electron to produce two photons of 0.511 MeV each ejected in opposite directions from the point of annihilation (an example of mass being converted to energy) (Johns and Cunningham, 1983).

Electrons also go through many elastic collisions along their paths which lead to frequent direction changes (Kawrakow and Rogers, 2002).

The detailed results of interactions of photons and charged particles in a medium are too complicated to predict analytically; Monte Carlo methods are the only known solution for prediction of these results. During a Monte Carlo simulation, particles with energy, charge, and direction (photons or charged particles) are created according to the distribution of their source. The distance

between catastrophic interactions is sampled from the exponential law of attenuation and depends on the total interaction cross section of the particle in the medium. The type of interaction depends on the relative contribution of various processes at the point of interaction. Secondary particles, with defined energies, charge and direction, are created as a result of these interactions, and are subsequently transported. The direction and energy of the original particle is continually changing. This process is continued until all the particles, i.e. the primary and secondary, are either absorbed or leave the interacting medium. It is possible to score the absorbed energy or the energy fluence of particles of a given type and charge within the user defined voxels of the medium. This process is continued for all the histories of the source and then averaged over all of these histories. Therefore, the larger the number of histories, the more statistically reproducible are the results of Monte Carlo simulation (Kawrakow and Rogers, 2002).

A problem arises in the case of Monte Carlo electron transport. Many fast electrons produce numerous charged particles, of very low energy, along their paths as they are slowing down. These secondary charged particles also go through many interactions before they are absorbed or escape the volume. Modeling every single interaction could be a very time consuming process. Therefore, EGSnrc employs a condensed history method, in which some of these interactions are grouped together. The justification for doing this is that during one interaction, the charged particles normally lose a very small amount of energy and go through a very slight change of direction. As a result of the condensed history technique, an artificial parameter called the step-length is introduced in the EGSnrc simulations of electron interactions.

In our calculation, the potential to use poly-energetic photons from the source was implemented in DOSXYZnrc as well as the ability to write a text file

which gives the spatially dependent energy deposition per incident gamma photon (Lachaine et al., 2001). Since the modeling of the detector response was done in a 1.25 MeV beam of  $\text{Co}^{60}$ , and a poly-energetic 6MV beam from a linear accelerator, the dominant interaction processes are Compton scattering and pair production (Johns and Cunningham, 1983).

### 3.3.1.1 Transport Parameters Used in our EGSnrc User Code

EGSnrc uses energy thresholds for each particle; below the thresholds the particles are assumed to deposit their energy locally. Ecut and AE are the minimum total energy of a charged particle that is transported in the medium. If the energy of an electron falls below the larger of Ecut or AE, its transport is terminated and all of its energy is deposited in the voxel in which it is located (Rogers, 2002). AP and Pcut are quantities similar to AE and Ecut with the exception that they are applicable to photons instead of charged particles. We used 0.521 MeV for Ecut/AE and 0.01 MeV for Pcut/AP. These values are based on the voxel dimensions of the crystals simulated in our calculations. UE and UP which are the upper limits of charged particle and photon transport respectively were both set to 20 MeV. The charged particle boundary crossing algorithms were chosen to be *exact* so that they are transported in single scattering mode as soon as they are within a distance from the boundary given by the *skin depth for the boundary crossing* algorithm (Rogers, 2002). The Koch and Motz (KM) method was selected for the bremsstrahlung angular sampling to ensure accurate simulation for the angle of the photon produced as a result of the bremsstrahlung interaction (Rogers, 2002). The atomic relaxation simulation is employed in our user code. This way the relaxation of atoms to their ground state after Compton and photoelectric effect is simulated (Rogers, 2002). All the other transport parameters in the code were set to their default values (Rogers, 2002).

### **3.3.2 DETECT2000**

To model the optical photon interactions, we used DETECT2000 ([www.gel.ulaval.ca/detect](http://www.gel.ulaval.ca/detect); Levin and Moisan, 1997). DETECT2000 is a Monte Carlo optical simulation code capable of modeling the geometry of scintillation detectors as well as a detailed treatment of the propagation, absorption, loss or detection of optical photon transport through these detectors. DETECT2000 generates optical photons isotropically at user defined points and follows their fate until they are either absorbed in the crystal bulk or surface coating, detected, or escape the volume. The program allows definition of the geometry of the crystal, optical glue and photodiodes using a generalized syntax ([www.gel.ulaval.ca/detect](http://www.gel.ulaval.ca/detect); Levin and Moisan, 1997).

#### **3.3.2.1 Surface Models in DETECT2000**

DETECT2000 allows the user to choose among six different surface finishes: METAL, PAINT, POLISH, GROUND, UNIFIED and PSEUDO. A PSEUDO surface is a non-existent surface and is merely employed for the purpose of connecting different components of similar material properties. The remaining five surfaces each treat the absorption and transmission of light at their boundaries differently.

##### **i. Metal**

In this model, the surface is assumed to be smooth and covered with a metallic coating. This surface allows no transmission. The user could specify a reflection coefficient, RC, for the surface. If a photon hits this surface, it is either absorbed in the surface with the probability  $(1-RC)$  or reflected back into the

component by specular reflection ([www.gel.ulaval.ca/detect](http://www.gel.ulaval.ca/detect); Levin and Moisan, 1997). In the event of a specular reflection, the angles of incidence and reflection with respect to the global normal of the surface are the same (Pedrotti and Pedrotti, 1993).

## **ii. Paint**

This model simulates a surface painted with a diffuse reflective material. As with the METAL model, no transmission is allowed and the user has the option of specifying an RC for the surface. If a photon hits this surface, depending on the RC, it is either absorbed in the surface or reflected back into the component by Lambertian reflection ([www.gel.ulaval.ca/detect](http://www.gel.ulaval.ca/detect); Levin and Moisan, 1997). Lambert's law states that the intensity of light scattered from a point on a reflecting surface follows a cosine relationship (Pedrotti and Pedrotti, 1993):

$$I(\theta_s) = I_0 \cos(\theta_s) \quad (3.8)$$

where  $\theta_s$  is the polar angle of the scattered light and  $I_0$  is the incident light intensity at the point. Lambert's law approximates what is observed in reflection from rough surfaces where many randomizing events may occur before the light leaves the surface (Pedrotti and Pedrotti, 1993).

## **iii. Polish**

This model simulates a perfectly polished surface that may or may not be in contact with another component. If no other component is specified, the surface is assumed to be in contact with vacuum. If a photon hits a POLISH surface, it is first tested for the probability of Fresnel (near source) reflection. This probability,  $R$ , is given by ([www.gel.ulaval.ca/detect](http://www.gel.ulaval.ca/detect); Levin and Moisan, 1997):

$$R = \frac{1}{2} \left[ \frac{\sin^2(\theta_i' - \theta_t')}{\sin^2(\theta_i' + \theta_t')} + \frac{\tan^2(\theta_i' - \theta_t')}{\tan^2(\theta_i' + \theta_t')} \right] \quad (3.9)$$

where  $\theta_i'$  and  $\theta_t'$  are the angles of incidence and refraction with respect to the local normal (which in this model is parallel to the global normal), respectively. The probability of transmittance, T, in this model is given by:

$$T = 1 - R \quad (3.10)$$

In case of refraction, Snell's law is followed. This law is stated as (Pedrotti and Pedrotti, 1993):

$$n_i \sin \theta_i = n_t \sin \theta_t \quad (3.11)$$

where  $n_i$  and  $n_t$  are the refractive indices of the incidence and transmittance media respectively; and  $\theta_i$  and  $\theta_t$  are the angles of incidence and transmittance with respect to the local normal respectively. Depending on the values of  $n_i$ ,  $n_t$  and  $\theta_i$ , total internal reflection might occur, in which case the photons are directed back into the incidence medium at an angle which again follows Snell's law. An external diffuse reflective coating with a reflection coefficient, RC, may be specified for this model to redirect some of the transmitted photons back into the incidence medium by Lambertian reflection ([www.gel.ulaval.ca/detect](http://www.gel.ulaval.ca/detect); Levin and Moisan, 1997).

#### iv. Ground

This model simulates a roughened optical surface. The only physical difference between this model and a POLISH surface is that the local surface

normals do not all point in the same direction. Therefore, the local normals are not parallel to the global normal but follow a Lambertian distribution. As with the POLISH model, the user has the option of specifying an external diffuse reflective coating with a reflection coefficient, RC, to redirect some of the transmitted photons back into the incidence medium by Lambertian reflection (www.gel.ulaval.ca/detect; Levin and Moisan, 1997). The distribution of light created by the POLISH and GROUND models are shown in Figure 3.8.

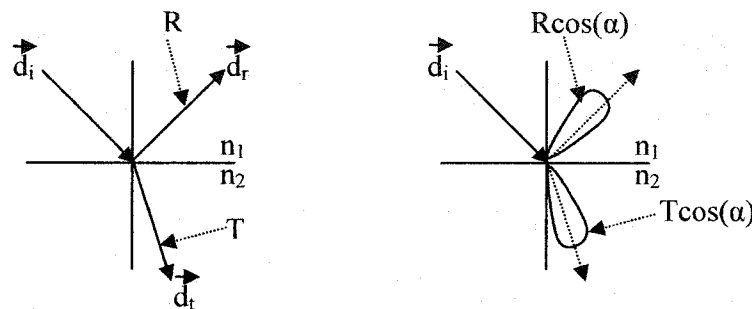


**Figure 3.8:** Polar plot of the distribution of light created by POLISH (left) and GROUND (right) surface models.  $\vec{d}_i$ : direction vector of incident photon,  $\vec{d}_r$ : direction vector of reflected photon,  $\vec{d}_t$ : direction vector of refracted photon,  $n_1$ : index of refraction of incidence medium,  $n_2$ : index of refraction of the transmission medium,  $\alpha$ : the angle between the local and global normal vectors.

## v. Unified

In the UNIFIED model, the angle between the local and global normals,  $\alpha$ , follows a Gaussian distribution with a mean of zero and a standard deviation, SA, defined by the user. Therefore, the user has the option of defining the degree of surface roughness in this model. As with GROUND and POLISH surfaces, this model allows the user to define an RC for an external diffuse reflective coating to redirect some of the transmitted optical photons back in the medium by



Lambertian reflection. In the UNIFIED model the user has the additional option of specifying an index of refraction, NRC, for this surface. This model also allows the user to specify a value for any of the following four types of reflection coefficients:

- $C_{sl}$ : the specular lobe constant. This coefficient controls the probability of specular reflection around a local normal.
- $C_{ss}$ : the specular spike constant. This coefficient controls the probability of specular reflection around the global normal.
- $C_{bs}$ : the backscatter spike constant. This coefficient controls the probability of backward reflection and is usually only applicable to very rough surfaces where a photon may go through several reflections in a deep imperfection and then be reflected back along its initial direction.
- $C_{dl}$ : the diffuse lobe constant. This coefficient controls the probability of internal Lambertian reflection.

The sum of these four coefficients is constrained to unity to conserve the probabilities of reflection and transmittance from the surface. A polar plot of the distribution of light created by the UNIFIED model is shown in Figure 3.9 ([www.gel.ulaval.ca/detect](http://www.gel.ulaval.ca/detect); Levin and Moisan, 1997).

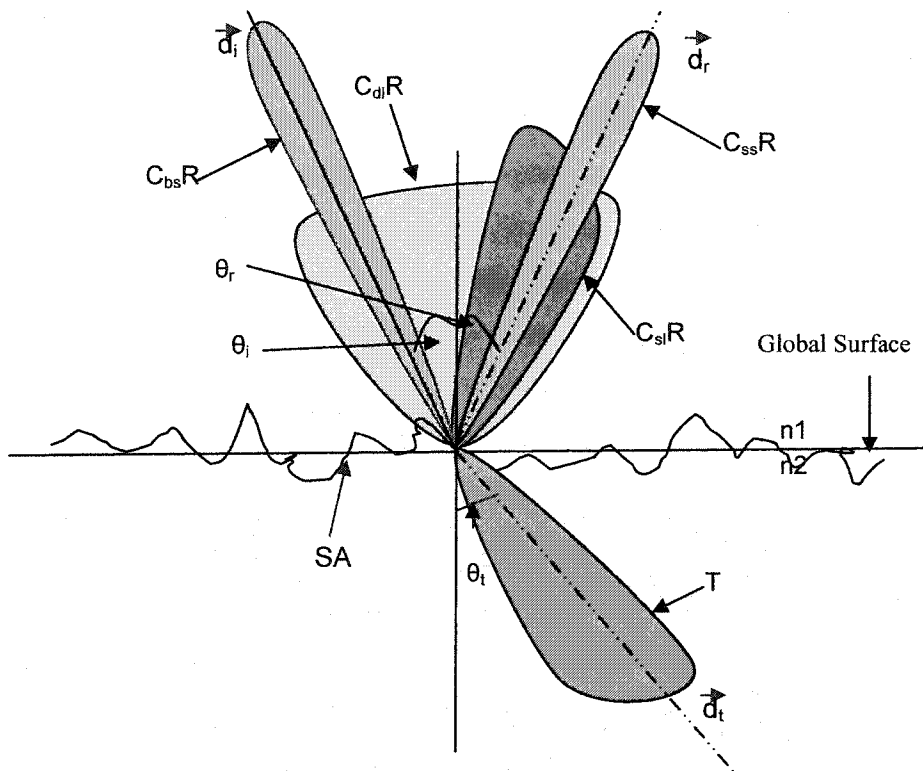


**Figure 3.9:** Polar plot of the distribution of light created by UNIFIED surface model.  $\vec{d}_i$ : direction vector of incident photon,  $\vec{d}_r$ : direction vector of reflected photon,  $\vec{d}_t$ : direction vector of refracted photon,  $n_1$ : index of refraction of incidence medium,  $n_2$ : index of refraction of transmission medium, SA: the standard deviation of the distribution of the angle of the local normal vectors with the global normal,  $C_{sl}$ : the specular lobe constant,  $C_{ss}$ : the specular spike constant,  $C_{bs}$ : the backscatter spike constant,  $C_{dl}$ : the diffuse lobe constant, T: transmittance distribution.

### 3.4 Studies Performed on Single Crystals

As stated before, single  $\text{CdWO}_4$  and  $\text{CsI(Tl)}$  crystals of fixed cross-section (0.275 cm x 0.8 cm) and variable heights were wrapped in teflon tape for reflective coating. The software packages described above were used to calculate the relative number of optical photons detected in the photodiode (per unit incident fluence from a teletherapy  $\text{Co}^{60}$  unit) as a function of the crystal height. Using the detector hardware and timing circuit boards described in previous sections, the detector signal was also measured for each crystal in the  $\text{Co}^{60}$  beam. A comparison of the measured and calculated signal allowed us to establish that the Monte Carlo methods can be used to accurately transport both the  $x(\gamma)$ -ray and the optical photons through the scintillation materials. In addition, some of the optical transport parameters such as the reflection coefficient of the reflective teflon tape could be estimated to provide a better match between the calculated and measured signal. The particular methods of calculating the signal using the two-step Monte Carlo method, and the measurement procedure, are described in the following sections.

#### 3.4.1 Calculation Model

The relative signal in the photodiode for each crystal was calculated using the two-step Monte Carlo model as follows. Each scintillation crystal was divided into  $0.055 \times 0.1 \times 0.1 \text{ cm}^3$  voxels in the DOSXYZnrc user code of the EGSnrc Monte Carlo system, running within the Linux operating system. In the Monte Carlo simulations, a rectangular beam of 1.25 MeV photons was incident such that it covered the entire upper crystal face. The user code was then used to calculate the total energy deposited within the entire crystal, as well as in each individual voxel. The transport parameters used in the simulation are stated in

section 3.3.1.1. A total of  $10^6$  photon histories were followed to give a statistical uncertainty of less than 4% in each voxel.

In the second step of the simulation, the geometry and characteristics of the crystals were modeled in the optical Monte Carlo code DETECT2000. A total of  $10^6$  optical photons were generated in each crystal. The number of optical photons isotropically generated in a voxel was proportional to the energy deposited in the voxel as determined from EGSnrc simulation. The optical emission spectra for  $\text{CdWO}_4$  and  $\text{CsI(Tl)}$  were taken from Kinloch et al. (1994) and Duclos (1998) respectively; these are shown in Figures 3.10 and 3.11. Optical photon transport in DETECT2000 considers self-absorption and scattering within crystal bulk, reflection and absorption in surface coating (i.e. teflon tape), refraction and total-internal reflection at crystal-glue-photodiode interfaces, and the spectral sensitivity of the photodiode array. The absorption mean free path of optical photons in  $\text{CdWO}_4$  was taken from Kinloch et al. (1994) and is shown in Figure 3.12. The corresponding value for  $\text{CsI(Tl)}$  was taken from manufacturer's specifications ([www.bicron.com](http://www.bicron.com)) ; a value of 10000 mm was used. The values of scattering coefficient were 1386 and 100000 mm for the  $\text{CdWO}_4$  and  $\text{CsI(Tl)}$  crystals, respectively. Crystal faces coated with the teflon tape were simulated as "ground" surfaces with a specified reflection coefficient (RC) for the coat. As such, the RC for the teflon tape is not known. Therefore, the optical simulations were carried out with several values of RC of teflon tape for both  $\text{CdWO}_4$  and  $\text{CsI(Tl)}$  crystals. It was found that a RC value of 0.975 for  $\text{CdWO}_4$  crystals (wrapped in-house) and 0.95 for  $\text{CsI(Tl)}$  crystals (factory wrapped) resulted in calculated detector signals that best matched the measured data. Since the crystal dimension in the y-direction, as shown in Figure 3.14, was larger than the photodiode, the crystals were divided into three parts joined by "pseudo-surfaces". The exit face (i.e. the plane defined by  $z = \text{crystal height}$ ) of the middle part (component 2 in Figure 3.14), in contact with optical glue, was a "ground" surface

without any external coating. The exit faces of the other two parts (components 1 and 3 in Figure 3.14) were "unified" surfaces to include the refraction due to glue (refraction coefficient = 1.47). The other parameters for this surface were chosen to include the fairly rough (SA = 10) and very shiny (RC = 1.0) bare metal foil that was placed to reflect optical photons back into the crystal. The interface between the optical glue and the photodiode was considered as "polish" surface without any external coating, to allow refraction and total-internal reflection. Since the thicknesses of the optical glue and photodiode were small (1 mm), the remaining surfaces of these two components were considered as perfect reflectors (metal) to avoid unnecessary escape of optical photons. Both the actual geometry and the modeled geometry of the CsI(Tl) crystals are shown in Figure 3.14. The refraction indices for  $\text{CdWO}_4$  (2.1-2.2), CsI(Tl) (1.8), and photodiode (1.54) were taken from manufacturer's specifications (Bicron; Hamamatsu). Similarly, the sensitivity spectrum of the photodiode was taken from the specification sheets. The photosensitivity of the photodiodes is given in Figure 3.13. The optical photons were then transported through the crystal until the photons were either absorbed within the crystal or the surface coating or detected by the photodiodes. A fraction of the optical photons hitting the photodiode surface was transmitted, based on the mismatch between the scintillator's emission and photodiode's sensitivity spectra. The theoretical detector signal was then calculated as the product of the fraction of total energy deposited in the crystal (EGSnrc output), the fraction of optical photons detected by the photodiode (DETECT2000 output), and the optical conversion efficiency of the scintillation material (Table 3.1).

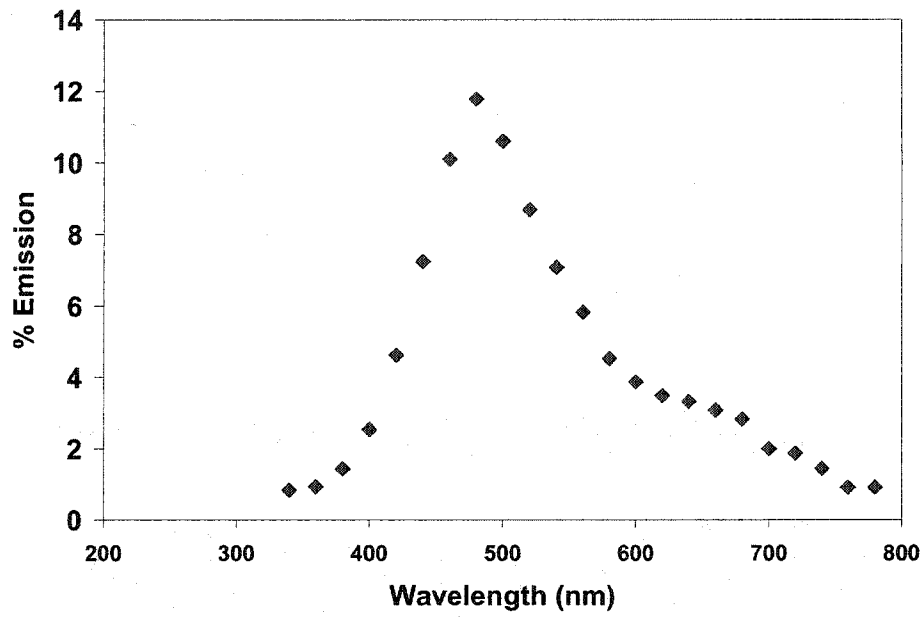


**Figure 3.10:** The optical emission spectrum of CdWO<sub>4</sub> as used in our study (Kinloch et al., 1994).

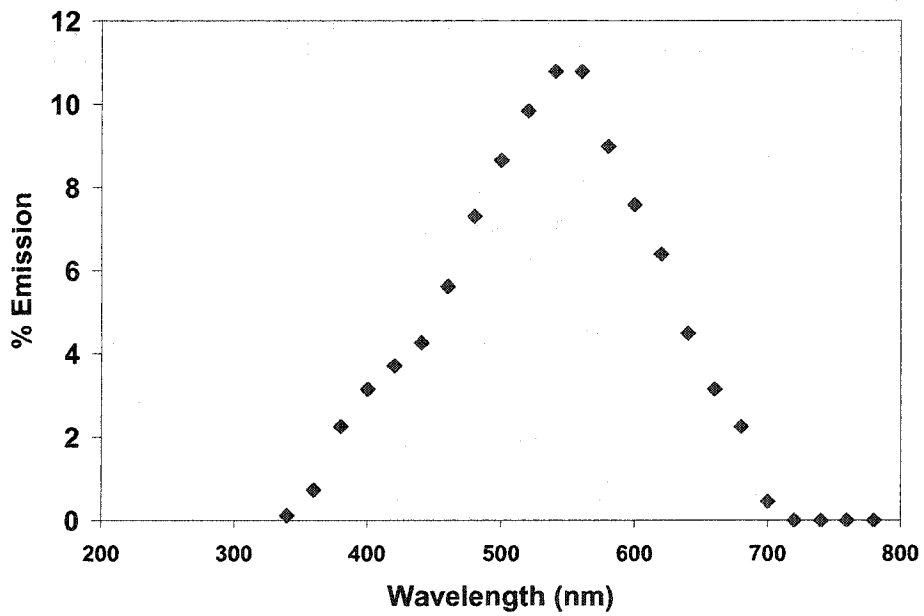


**Figure 3.11:** The optical emission spectrum of CsI(Tl) as used in our study (Duclos, 1998).

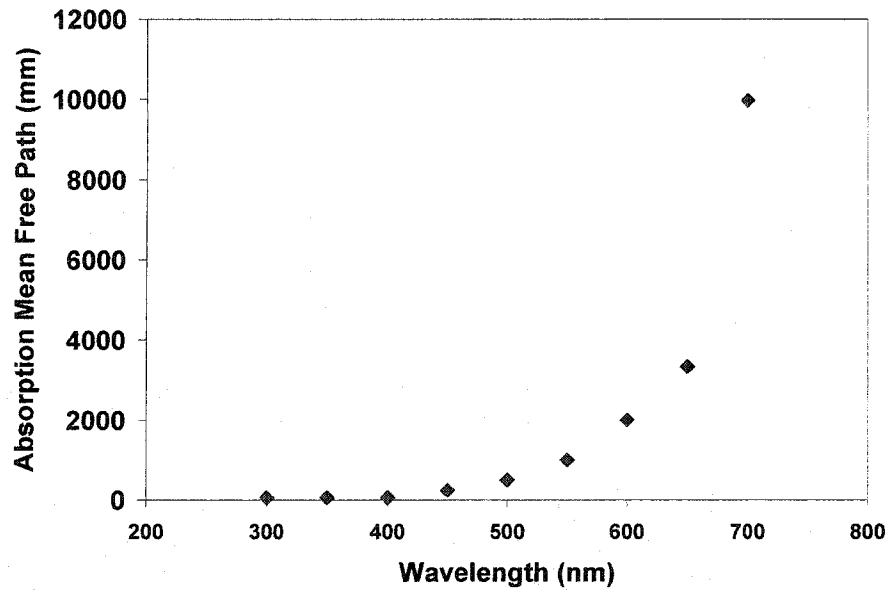


**Figure 3.12:** Absorption mean free path of optical photons in CdWO<sub>4</sub> (Kinloch et al., 1994).

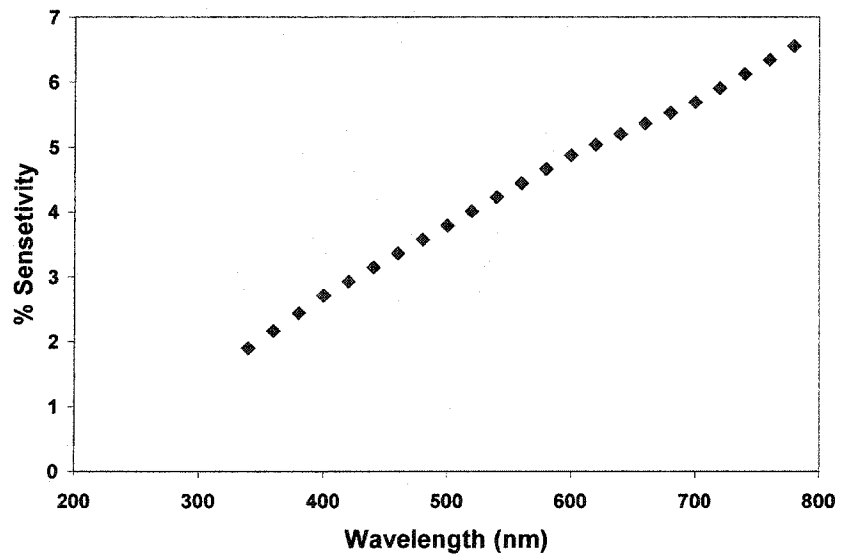


**Figure 3.13:** Photosensitivity spectrum of the photodiodes as used in our study ([www.Hamamatsu.com](http://www.Hamamatsu.com)).

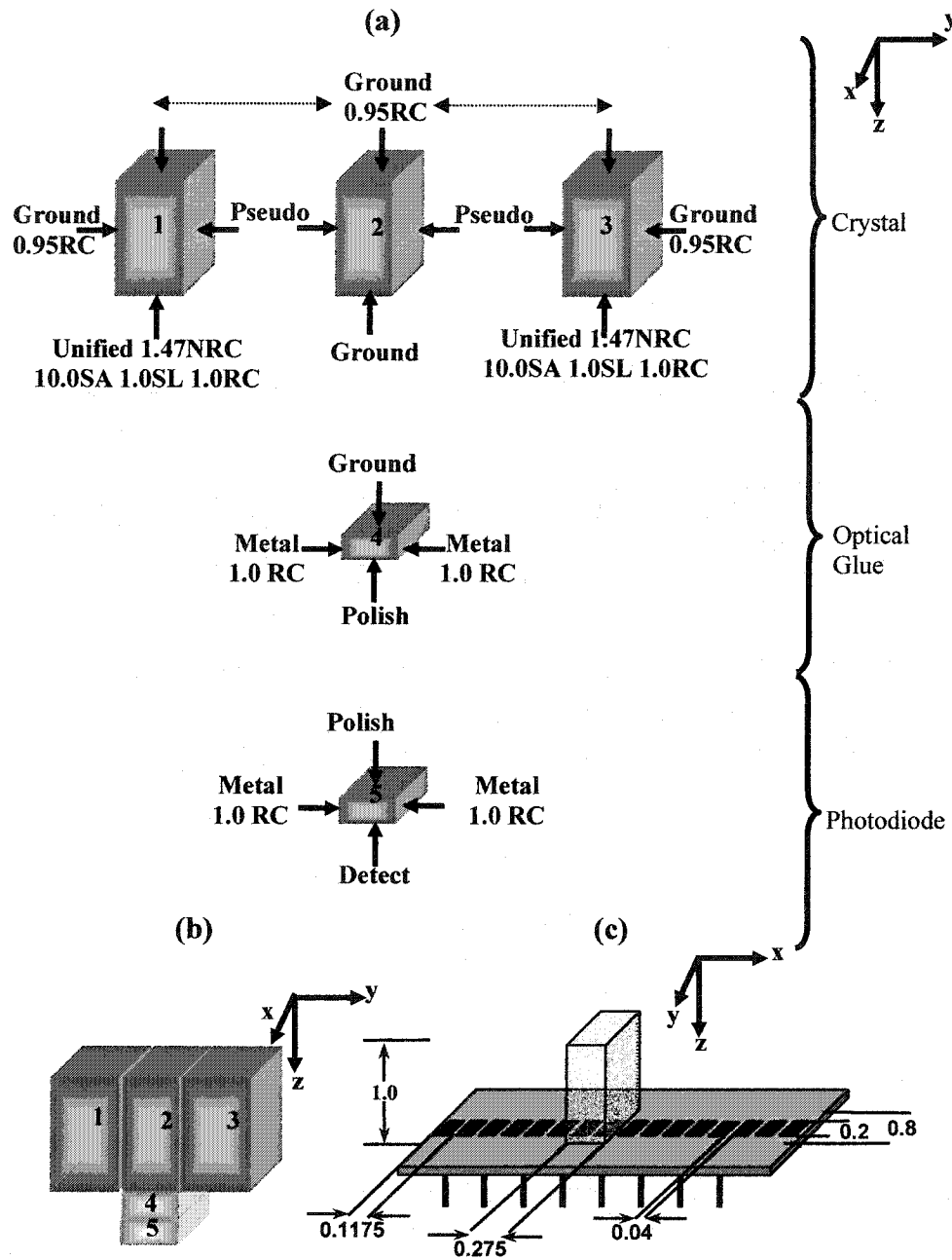


**Figure 3.14:** The modeled and actual single CsI(Tl) crystal: (a) Components 1, 2 and 3 show the three segments of the CsI(Tl) crystal of height 1 cm as modeled in DETECT2000. The x and z dimensions of these components are 0.275 cm and 1 cm respectively. The y dimension of these components is 0.3, 0.2 and 0.3 cm respectively. Component 4 shows the modeled optical glue of size  $0.275 \times 0.2 \times 0.1 \text{ cm}^3$ . Component 5 shows the modeled photodiode of size  $0.275 \times 0.2 \times 0.1 \text{ cm}^3$ . (b) The relative position of components in DETECT2000 with respect to each other. (c) The actual dimensions (cm) and positioning of the single crystal and photodiodes. The surfaces going into and coming out of the page for components 1-3 are *Ground 0.95RC*, and for components 4-5 are *Metal 1.0RC*.



## 3.4.2 Measurements

### 3.4.2.1 Single Crystal Signal

The wrapped single crystals were individually placed on the central photodiode pair under a  $4 \times 4 \text{ cm}^2$   $\text{Co}^{60}$  beam at a distance of 110 cm from the source. For each crystal, 1000 detector readings were taken using an integration period of 0.7 ms while the beam was on. An average dark current signal was subtracted from the average of 1000 readings to obtain the detector signal as a function of crystal height. For each scintillation crystal type, the measured detector signal was compared with that calculated from the two-step Monte Carlo method discussed in the previous sections. Both the calculated and measured signals were normalized to their respective means of all crystal heights. A photograph of our set-up for these measurements is shown in Figure 3.15.

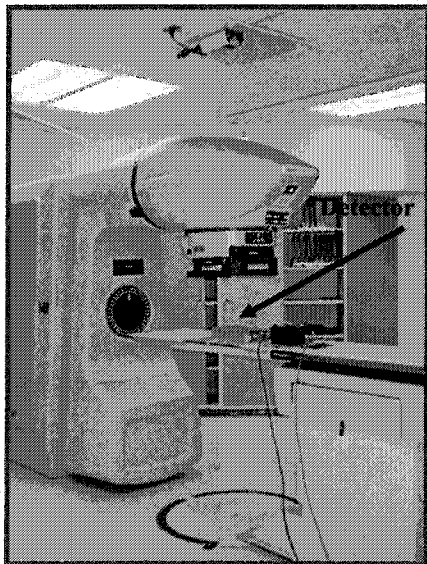


**Figure 3.15:** The set-up used in measuring the signal of single crystals.

### 3.4.2.2 Afterglow Assessment

Afterglow in scintillation crystals was assessed as the residual signal as a function of time after the radiation beam was turned off. As the time scale of these measurements is of the order of ms, an x-ray beam with even shorter turn-on and turn-off times is required. Since the travel time of the  $\text{Co}^{60}$  source is hundreds of ms, the radiation beam from an electronically controlled x-ray tube, a radiotherapy simulator (Model Super 800 CP, Phillips Medical Systems) operated in radiographic mode, was used to assess the afterglow. The detector box was placed on the simulator couch and  $\text{CdWO}_4$  and  $\text{CsI(Tl)}$  crystals of 10 mm height were placed on the photodiodes. The detector was placed in one quadrant of the  $10 \times 10 \text{ cm}^2$  field to avoid the cross hairs. The frequency of the trigger signal on the timing board was set to 1345 Hz, resulting in a detector reading every  $\sim 0.74$  ms ( $\sim 0.44$  msec integration time). The detector readings were recorded for several seconds. The x-ray beam was off for approximately 1000 ms of initial data acquisition, data was then acquired for a 4000 ms exposure at 140 kV and 40 mA, and the beam was again turned off for the last  $\sim 2500$  ms. The dark current was subtracted from all data points. The mean signal from the dark subtracted data was calculated for the two crystals from the portion of signal during the beam on. The entire dark subtracted data set for each of the two crystals was then normalized to the mean signal for that crystal.

### 3.5 Dose Response and Beam Attenuation Characteristics of the $\text{CdWO}_4$ detector

An array of eight  $0.275 \times 0.8 \times 1.0 \text{ cm}^3$  (x,y,z, Figure 3.17)  $\text{CdWO}_4$  crystals was constructed by bonding the crystals in white gelcoat (Ashland Chemical Type 1 polyester gelcoat) polyester resin epoxy, commonly used as the outer coat for Fiberglas boats (Berndt, 2002). The crystals were held 0.04 cm apart when being coated with gelcoat and bonded (Berndt, 2002) in polyethylene

moulds. The crystal array made from CdWO<sub>4</sub> was used to test the detector's response to dose rate. The same detector was also used to measure the attenuation of a Co<sup>60</sup> beam by solid water. A linear dose response and accurate attenuation measurement capability are desirable properties of a CT detector.

### 3.5.1 Detector Dose Response

This experiment was designed to test the response of the detector with respect to dose in a 4 x 4 cm<sup>2</sup> Co<sup>60</sup> beam. The experiment was carried out with an 8-element CdWO<sub>4</sub> array. The source to detector distance (SDD) was varied from 76 cm to 106 cm in 5 cm steps, with an additional measurement at 110 cm. A total of 1000 data points were collected at each SDD using an integration period of 0.7 ms. The mean detector signal over these 1000 points minus the dark current was taken as the detector signal at each SDD. For each SDD, the dose in free space per integration period was calculated using the calibrated dose rate in free space of the Co<sup>60</sup> unit (D<sub>0</sub>), the head scatter factor for a 4 x 4 cm<sup>2</sup> beam (HSF(4x4cm<sup>2</sup>)) and the inverse square factor.

$$Dose(Gy) = D_0 \left( \frac{Gy}{min} \right) \cdot HSF(4x4cm^2) \cdot \frac{80^2}{SDD^2} \cdot 0.7msec \cdot \frac{1}{60 \cdot 1000} \left( \frac{min}{msec} \right) \quad (3.12)$$

### 3.5.2 Measurement of Beam Attenuation

The fundamental objective of CT detectors is to measure the attenuation of the beam by the scanned object in an accurate and linear manner with good signal to noise ratio. A second experiment was therefore designed to study the attenuation of a Co<sup>60</sup> beam by solid water using the 8-element CdWO<sub>4</sub> array. Slabs of solid water (15 slabs each 2 cm thick) were placed in the path of a narrowly collimated Co<sup>60</sup> beam (2 x 4 cm<sup>2</sup>) on top of the treatment couch, while

the detector was placed under the treatment couch at a SDD of 103cm. The source to couch top distance was 85 cm. For each thickness of solid water, 1000 readings for each detector element were taken using an integration period of 1.7 ms. The corresponding dark current was subtracted from the mean of these readings to give the detector signal for each solid water thickness. The attenuation factor for each solid water thickness was then calculated. The set-up for this experiment is shown in Figure 3.16.

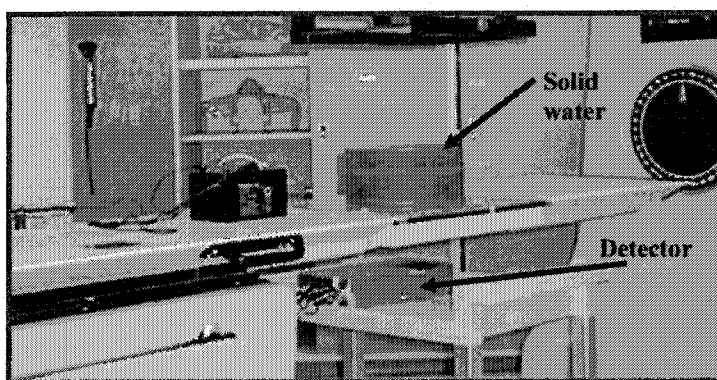


**Figure 3.16:** The set-up used in measuring beam attenuation.

### **3.6 Imaging Characteristics Studies Performed on the CdWO<sub>4</sub> Detector Array**

Image quality is a generic concept applicable to different types of images. “Quality” however is a very subjective concept; therefore attempts have been made to quantify this notion. The true test of a diagnostic imaging system is how well it allows the detection of subtle abnormalities (Bushberg et al., 2002). The main components of image quality are contrast, spatial resolution, and noise (Bushberg et al., 2002). In what follows each of these components and their relevance to CT imaging is discussed. All the discussions in this section are taken from Bushberg et al.(2002) .

**Contrast:** Contrast is the difference in brightness between adjacent regions in an image. The final contrast in an image is the result of the combined effects of data acquisition, image reconstruction from projections, and display. Different types of contrast include the subject contrast, detector contrast, digital image contrast and displayed contrast. Subject contrast is the difference in some aspect of the input signal (energy fluence incident on detector) before it is recorded, therefore it is independent of the detector being used. Detector contrast it is a measure of how the detector array translates the subject contrast (incident fluence) into output contrast in measured projection data. Digital image contrast is the contrast obtained in the reconstructed output image after a series of automatic operation are performed on the output signal as a part of the reconstruction process. Finally, the displayed contrast of a digital image is the output obtained after the digital image data in the computer is converted to the display hardware output using a look-up table .The appearance of the final image can be changed dramatically by manipulating this look-up table; this process can be done in real time with visual feed back from the display monitor. Therefore, a detector that responds linearly to incident fluence is desirable, and that has a steep slope in a linear relation between detector signal and incident fluence is very important. kVCT has the best contrast resolution of any clinical x-ray modality. The contrast resolution of screen-film radiography and kVCT are approximately 5% and 0.5%, respectively.

**Spatial Resolution:** Spatial resolution is the ability of a system to clearly display two very small and very closely spaced separate objects .One way of quantifying the spatial resolution of a detector is to analyze the response of the system to a point signal. This response is termed the point spread function or PSF of the system. If the shape of the PSF is independent of the spatial location where the point input is placed, the system is said to be stationary. The extent of a

system's PSF quantifies the detector blurring properties. The line spread function, or LSF, of a system describes the response of the system to a line input. LSF can be visualized as a linear summation of a large number of PSFs and it has the advantage of being easier to measure than a PSF. The modulation transfer function or MTF of a system is a very complete description of the spatial resolution properties of the system. This function shows what percentage of the input signal's contrast is recorded by the imaging system as a function of the spatial frequency (or size) of the signal. The size of an object is related to its spatial frequency by the following relationship:

$$f = \frac{1}{2\Delta} \quad (3.13)$$

where  $\Delta$  is the size of the object in the dimension of interest and  $f$  is the corresponding spatial frequency. With the knowledge of the LSF of a detector in one direction, for example  $LSF(x)$ , the MTF of the detector as a function of spatial frequency in that direction,  $MTF(f)$ , can be computed using the following equation:

$$MTF(f) = |FT\{LSF(x)\}| \quad (3.14)$$

where FT is the Fourier transform. In quantifying the spatial resolution of our detector, we employed LSFs in determining the MTF of the detector as discussed in the following section.

It should be remembered that the MTF described above is for the detector alone. It is measured and calculated in complete isolation to the rest of the imaging components in a CT system. The other factors that contribute to the MTF of a CT scanner are focal spot size, source and detector collimators, type of

convolution filter used in the filtered back projection image reconstruction method (Glover and Eisner, 1979), interpolation type and image pixel size. These factors are not considered here, rather the detector's MTF is analyzed since the main objective is to model the detector system as opposed to a complete CT imaging system. Due to larger pixel sizes employed in CT scanning, spatial resolution in CT scanning is generally worse than x-ray radiography.

**Noise:** Image noise is a stochastic component introduced into the image from different sources. The mean value and standard deviation, or noise, in a quantity can be determined by repeated measurements of the quantity. If N is the number of measurements performed and  $X_i$  is the value obtained after each single measurement, the mean value,  $\bar{X}$ , can be calculated as:

$$\bar{X} = \frac{1}{N} \sum_{i=1}^N X_i \quad (3.15)$$

The standard deviation,  $\sigma$ , is defined as:

$$\sigma = \sqrt{\frac{\sum_{i=1}^N (\bar{X} - X_i)^2}{N-1}} \quad (3.16)$$

X-ray and  $\gamma$ -ray statistics follow a Poisson distribution, P(x), given by:

$$P(x) = \frac{\bar{X}^x}{x!} e^{-\bar{X}} \quad (3.17)$$

where  $\bar{X}$  is the mean value and  $x$  is the dependent variable. The Poisson distribution is very close to a Gaussian distribution,  $G(x)$ , when  $\sigma = \sqrt{\bar{X}}$  in the Gaussian equation given by:

$$G(x) = ke^{-\frac{1}{2}\left(\frac{\bar{X}-x}{\sigma}\right)^2} \quad (3.18)$$

where  $k$  is a constant,  $\bar{X}$  is the mean value and  $\sigma$  is the standard deviation. The conditional approximate equivalence of the Poisson and Gaussian distributions is useful in quantum imaging. If the mean input signal on the detector consists of  $N$  Poisson distributed quanta, the input noise can be approximated by  $\sqrt{N}$ ; therefore the input signal to noise ratio,  $SNR_{in}$ , is given by:

$$SNR_m = \frac{N}{\sigma} = \frac{N}{\sqrt{N}} = \sqrt{N} \quad (3.19)$$

In a perfect detector the output SNR is determined only by the input SNR. However, most imaging systems add a considerable amount of noise to the input, and do not absorb all the input quanta. The importance of detected SNR is closely related to the contrast resolution of the system. According to Rose's criterion, to identify an object the output SNR for the object has to be better than about 5. The noise power spectrum or Wiener spectrum of the noise variance ( $\sigma^2$ ) of the output signal of a system is the most complete way of quantifying the system's output noise properties. This function shows the spread of the output variance of a uniform signal over all spatial frequencies. Analyzing the Wiener spectrum can show if there are subtle relationships between noise at one point of the imaging chain with respect to the others. In our analysis of the detector noise, we employed the Wiener spectrum.



**Detective Quantum Efficiency:** The detective quantum efficiency of an imaging system is defined as:

$$DQE = \frac{SNR_{out}^2}{SNR_{in}^2} \quad (3.20)$$

where  $SNR_{in}$  is the input signal to noise ratio and  $SNR_{out}$  is the output signal to noise ratio. DQE is the gold standard by which the imaging performance of a detector is measured since it quantifies the overall SNR performance of an imaging system. Hence, an accurate description of the detector DQE was the major goal in the study of the imaging characteristics of our prototype detector.

### 3.6.1 Modeling the Imaging Characteristics

#### 3.6.1.1 Detector Geometry

The geometry of the prototype detector array was discussed in section 3.2. The geometry of the crystal array modeled in DETECT2000 is shown in Figure 3.17, where individual  $0.275 \times 0.8 \times 1.0 \text{ cm}^3$  ( $x,y,z$ ) (Notice that this voxel sizes are different from the ones used for single crystals)  $\text{CdWO}_4$  crystals are described as Component 1 (items labeled with a '1' in Figure 3.17). All surfaces are "ground" with  $RC = 0.975$ , with the exception that  $RC$  does not apply to the surface facing the photodiodes as it was not coated. Component 2 in Figure 3.17 describes a single sheet of optical glue compound ( $2.48 \times 0.8 \times 0.0075 \text{ cm}^3$ ) that is placed between the bonded crystal array and the photodiode's top surface. In the bonded array, spaces between crystals are filled with gelcoat. Therefore, in the top surface of Component 2, the surfaces which are not in contact with the crystals have a surface finish of "ground 0.975RC" to simulate the gelcoat finish properties. The top surface of the photodiode array is very complex (Figure

3.14(c): (1) spaces in between the photodiode elements are finished with a smooth, shiny metal; (2) the excess length of crystal in y-direction is sitting atop bare-metal foil; and (3) the photodiodes themselves have different properties than (1) and (2). The bottom of the single sheet of optical glue (i.e. Component 2 in Figure 3.17) cannot be modeled as a complex surface in DETECT2000. Therefore, additional optical glue components were generated to take care of complexities (1) and (2) described above. The optical glue Components 3 and 4 (each  $2.48 \times 0.3 \times 0.001 \text{ cm}^3$ ) have their bottom surfaces defined as "metal RC = 1.0", to model the bare metal foil. The end surfaces in the x and y directions are also "metal RC = 1.0" except junctions with photodiodes and shiny spaces, which are made through "pseudo" surfaces. The optical glue Components 6, 8, ... 34 (each  $0.04 \times 0.2 \times 0.001 \text{ cm}^3$ ) describe spaces in between the photodiodes, with a bottom surface of "metal RC = 1.0". The interface to Components 3 and 4 is "pseudo" in the y-direction, and to Components 5, 6, 7...35 is "detect" in x-direction. The photodiode Components 5, 7, 9...35 (each  $0.1175 \times 0.2 \times 0.01 \text{ cm}^3$ ) interface to Components 3 and 4 as "pseudo" in the y-direction. All other surfaces except the top of these components are assumed to be "detect". The top surface of Components 3 to 35 is "polish" to interface with the bottom of Component 2.

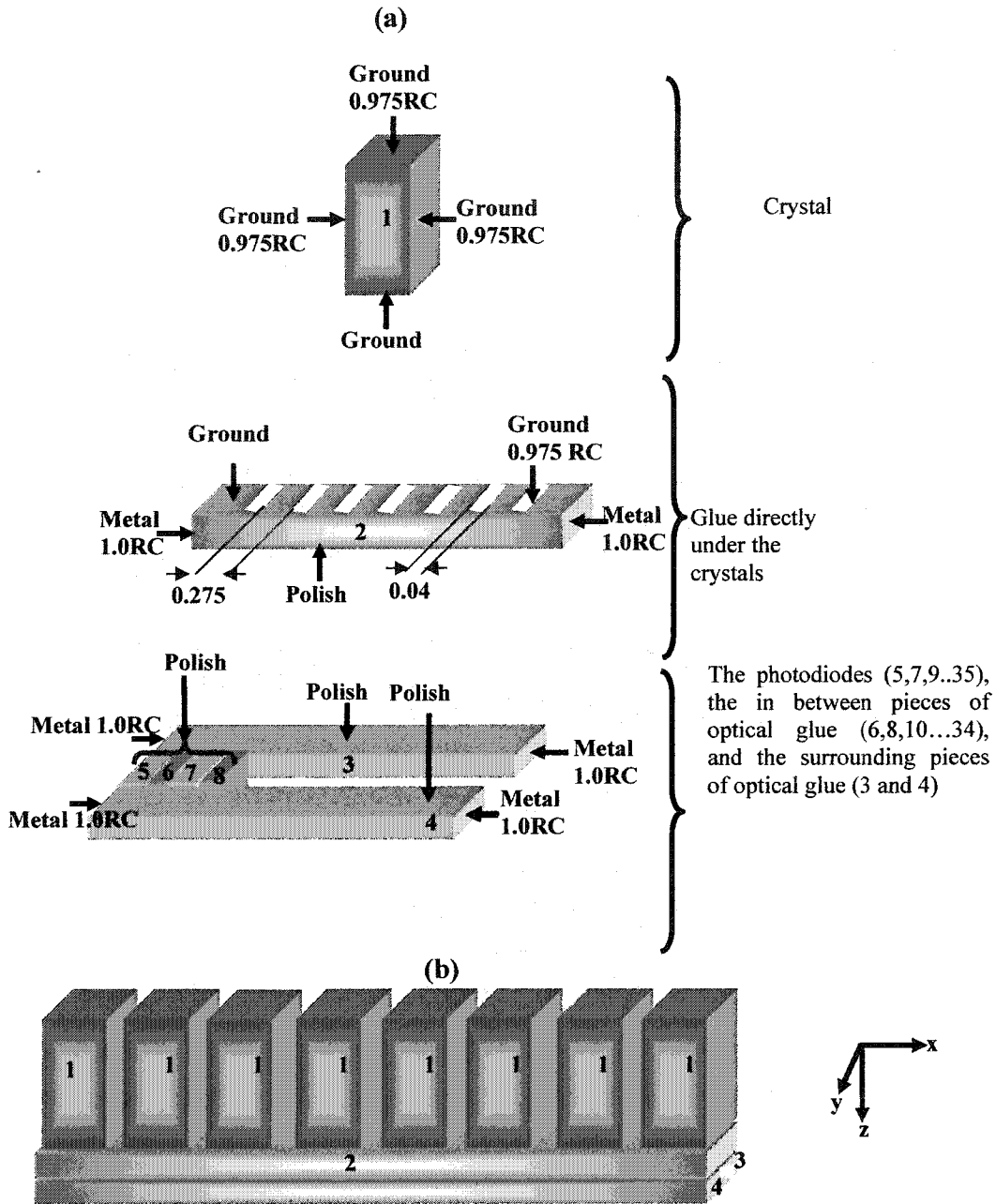


**Figure 3.17:** The modeled geometry of the 8-element crystal array. (a) The dimensions of each crystal are  $0.275 \times 0.8 \times 1.0 \text{ cm}^3$ . The dimensions of glue component 2 are  $2.48 \times 0.8 \times 0.0075 \text{ cm}^3$ . The dimensions of component 3 and 4 are  $2.48 \times 0.3 \times 0.001 \text{ cm}^3$ . The dimensions of photodiode components 5, 7, 9...35 are  $0.1175 \times 0.2 \times 0.001 \text{ cm}^3$ . The dimensions of glue components 4, 6, 8...34 are  $0.04 \times 0.2 \times 0.001 \text{ cm}^3$ . (b) This figure shows the relative position of components with respect to each other. In components 1 and 2, the surfaces going into and coming out of the page are *Ground 0.975R* and *Metal 1.0RC*, respectively. In component 3, the surface going into the page is *Metal 1.0RC*, while the surface coming out of the page is *Pseudo*; in component 4 this order is reversed. For components 5 to 35 the surfaces going into and coming out of the page are *Pseudo*. The bottom surfaces of components 6, 8, 10... 34 and components 3-4 are *Metal 1.0RC*. All the other surfaces are *Detect*.

### 3.6.1.2 Theory Used in Calculating the Imaging Characteristics

The goal of modeling was to determine the imaging characteristics of our detector. Therefore, we modified the method suggested by Kausch et al (1999) to suit the detector geometry for the scintillation array. Mathematical derivation of this method is presented as follows.

The DQE of a detector array in the Fourier domain is defined as:

$$DQE(f) = \frac{\frac{\mu_{out}^2(f)}{NPS_{out}(f)}}{\frac{\mu_{in}^2(f)}{NPS_{in}(f)}} \quad (3.21)$$

where  $\mu_{in}(f)$  is the input signal (incident fluence) in frequency space,  $\mu_{out}(f)$  is the output detector signal in frequency space,  $NPS_{in}(f)$  is the input noise power spectrum, and  $NPS_{out}(f)$  is the output noise power spectrum. Let  $s(n)$  be the incident fluence on each element of the detector represented in the sampled spatial domain.  $s(n)$  can be written as:

$$s(n) = \bar{s}(n) + \Delta s(n) \quad (3.22)$$

where  $\bar{s}(n)$  is the average input signal on a detector element,  $n$ , and  $\Delta s(n)$  is the fluctuation around the average. Let  $g(n)$  be the number of optical photons detected by each detector, again represented in the sampled spatial domain.

$$g(n) = \bar{g}(n) + \Delta g(n) \quad (3.23)$$

where  $\bar{g}(n)$  is the average output signal from a detector element,  $n$ , and  $\Delta g(n)$  is the fluctuation around the average. In our case, the input signal is the beam of x-ray photons impinging on the detector, and the output signal is the number of optical photons detected by the photodiodes. In frequency space, the input and output signals can be written as:

$$\mu_{in}(f) = \sum_n \bar{s}(n) \bullet e^{i2\pi[(fn)/M]} \quad (3.24)$$

$$\mu_{out}(f) = \sum_n \bar{g}(n) \bullet e^{i2\pi[(fn)/M]} \quad (3.25)$$

where  $M$  is the number of elements in the array and the symbol  $\bullet$  denotes multiplication. The noise power spectrum of the input and output signal can be written as:

$$NPS_{in}(f) = \left\langle \left| \sum_n \Delta s(n) \bullet e^{i2\pi[(fn)/M]} \right|^2 \right\rangle \quad (3.26)$$

$$NPS_{out}(f) = \left\langle \left| \sum_n \Delta g(n) \bullet e^{i2\pi[(fn)/M]} \right|^2 \right\rangle \quad (3.27)$$

where  $\langle \rangle$  implies averaging over many realizations. Assuming a linear, shift invariant system we have:

$$g(n) = \lambda \bullet \sum_{n'} l_d(n-n') \bullet s(n') \bullet dn' + \Delta g_{Det}(n) \quad (3.28)$$

where  $\lambda$  is the average number of optical photons detected per incident x-ray,  $l_d(n)$  is the LSF of the detector and  $\Delta g_{Det}(n)$  is the noise due for image degradation of the detector. Equation 3.28 can be written as the sum of its mean signal and noise (fluctuations around mean) components:

$$\bar{g}(n) = \lambda \cdot \sum_{n'} l_d(n-n') \cdot \bar{s}(n') dn' \quad (3.29)$$

$$\Delta g(n) = \lambda \cdot \sum_{n'} l_d(n-n') \cdot \Delta s(n') dn' + \Delta g_{Det}(n) \quad (3.30)$$

If a pencil beam of  $N_y$  x-rays is incident on the detector, the input signal  $\bar{s}(n)$  in frequency space is written as follows:

$$\mu_{in}(f) = N_y \quad (3.31)$$

The Fourier transform of equation 2.29 gives:

$$\mu_{out}(f) = \lambda \cdot L_d(f) \cdot N_y \quad (3.32)$$

where  $L_d(f)$  is the absolute value of the Fourier transform of the LSF or the MTF of the detector. The input and output noise power spectra are given by:

$$NPS_{in}(f) = N_y \quad (3.33)$$

$$NPS_{out}(f) = \left\langle \left| FT\left(\lambda \cdot \sum_{n'} l_d(n-n') \cdot \Delta s(n') dn' + \Delta g_{Det}(n)\right) \right|^2 \right\rangle \quad (3.34, a)$$

$$= \lambda^2 \cdot |L_d(f)|^2 \cdot \langle |FT(\Delta s(n))|^2 \rangle + \langle |FT(\Delta g_{Det}(n))|^2 \rangle \quad (3.34, b)$$

$$= \lambda^2 \cdot |L_d(f)|^2 \cdot NPS_{in}(f) + NPS_{Det}(f) \quad (3.34, c)$$

Equation 3.33 is based on the assumption that the production of x-rays is spatially uncorrelated and follows a Poisson distribution. Equation (3.34,a) follows from substituting 3.30 in 3.27. Equation (3.34, b) follows by assuming that there is no correlation between the noise added by the detector and the noise inherent to x-ray production. Convolution in spatial domain is replaced by the product in frequency domain.

Therefore equation 3.21 can be rewritten as:

$$DQE(f) = \frac{\frac{1}{N_y} |L_d(f)|^2}{\frac{NPS_{Det}(f)}{\lambda^2 N_y^2} + \frac{1}{N_y} |L_d(f)|^2} \quad (3.35)$$

Since  $L_d(f) = MTF(f)$ , we have:

$$DQE(f) = \frac{MTF^2(f)}{\frac{NPS_{Det}(f)}{\lambda^2} + MTF^2(f)} \quad (3.36)$$

where  $\overline{NPS}_{Det}(f) = NPS_{Det}(f)/N_y$  is the normalized detector NPS.

To determine the imaging characteristics of our array of crystals, a narrow (0.2 mm) slit beam of 1.25 MeV photons, parallel to the y direction, was incident in the middle of the fourth crystal. The modified version of DOSXYZnrc, which is described in section 3.3.1, was used to estimate the dose deposited in each user defined voxel per incident gamma photon. The crystals were divided into 0.055 x 0.8 x 0.1 cm<sup>3</sup> voxels and the energy deposited into each voxel by each incident

photon,  $e_i(n',z)$ , was calculated. This energy distribution in the crystal array was stored separately for each of 10,000,000 incident photons.

The optical transport properties in the crystal array, where individual crystals are optically isolated, results in a spatially variant LSF since optical photons generated near the coated crystal surfaces do not have similar freedom to scatter as optical photons generated in the middle of the crystal. Therefore, DETECT2000 was used to calculate the spatially variant LSFs for optical photon spread,  $l(n; n',z)$ , by creating optical line sources within each crystal, located at the same 50 positions defined by x and z voxel locations as used in the EGNrc simulation.  $l(n; n',z)$ , is the optical LSF for a pencil of optical photons located at voxel( $n',z$ ) in the crystal, and n is the detecting photodiode in the x direction. Note that two consecutive photodiodes are coupled, and therefore n ranges from 1 to 8 for our 8-element crystal array. The superposition of the spatially resolved MV energy deposition distribution,  $e_i(n',z)$ , with the LSFs,  $l(n; n',z)$ , gives us the optical distribution functions  $g_i(n)$  for every photon number i as stated in the following equation:

$$g_i(n) = \sum_{n',z} l(n; n', z) \cdot e_i(n', z) \quad (3.37)$$

The average optical distribution function is given by:

$$\bar{g}(n) = \frac{1}{N_y} \sum_{i=1}^{N_y} g_i(n) \quad (3.38)$$

The mean number of optical photons per incident x-ray which are detected within the photodiode array is given by:



$$\lambda = \sum_n \bar{g}(n) \quad (3.39)$$

The normalized LSF of the detector and its MTF(f) are given by the following two equations respectively:

$$l_d(n) = \frac{\bar{g}(n)}{\lambda} \quad (e.40)$$

$$MTF(f) = \left| \sum_n \frac{\bar{g}(n)}{\lambda} e^{i2\pi(fn/M)} \right| \quad (3.41)$$

The fluctuation in the output for each individual x-ray is given by:

$$\Delta g_i(n) = g_i(n) - \bar{g}(n) \quad (3.42)$$

Taking the Fourier transform gives:

$$\Delta G_i(f) = \sum_n \Delta g_i(n) e^{i2\pi(fn/M)} \quad (3.43)$$

Therefore, the normalized detector noise power spectrum is given by:

$$\overline{NPS}_{Det}(f) = \frac{1}{N_y} \sum_i |\Delta G_i(f)|^2 \quad (3.44)$$

A similar modeling procedure was also used for a 6 MV photon beam with the exception that a 6 MV photon spectrum (Lachaine et al., 2001) was used for our slit beam. This spectrum, as well as a spectrum simulated by the Monte Carlo

code, BEAM (Sheikh-Bagheri,2002), for a 600C Varian linac is shown in Figure 3.18.

It is worth noting that in this work, as well as in the work performed by Kausch et al., the noise due to the creation of optical photons is ignored. This is due to the large number of optical photons generated in  $\text{CdWO}_4$  ( $\sim 15000/\text{MeV}$ ) and  $\text{CsI(Tl)}$  ( $\sim 59000/\text{MeV}$ ) crystals (Derenzo and Moses, 1992).

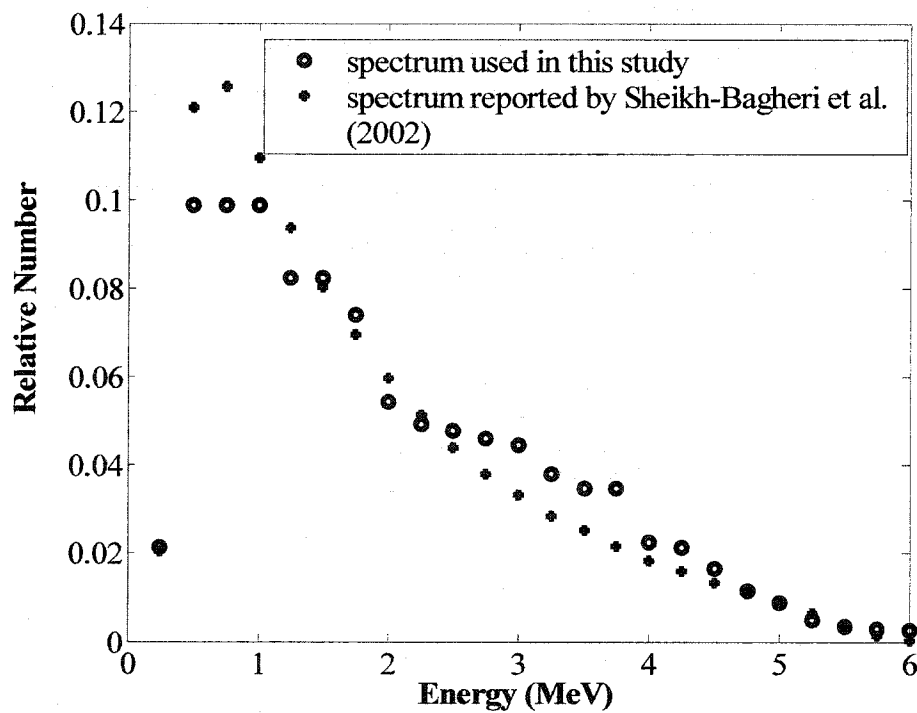


**Figure 3.18:** Varian 600C energy spectrum for 6MV photons.

### 3.6.2 Measurements

To measure the MTF(f), NPS(f) and DQE(f) in conditions similar to the modeled ones, the detector array was placed on the treatment couch in a Co<sup>60</sup> unit. The fourth crystal was centred at isocenter in the Co<sup>60</sup> beam, at a distance of 80 cm from the source. The beam was collimated to a 0.2 mm wide slit by two 25 x 5 x 10 cm<sup>3</sup> lead blocks. The output of each crystal was recorded with a 0.7 ms integration period, and a total of 10000 readings were taken for each detector element. The data was corrected for dark current and gain variations among detector elements. The corrected data,  $g_k(n)$  ( $k=1:10000$ ), was used for estimating the measured LSF and MTF(f) using equations (3.40) and (3.41). Since the number of photons per integration period,  $N_y$ , for the slit beam incident on the detector was not known, only the relative shape of  $NPS_{det}(f)$  could be determined using equation (3.44). Therefore, a separate approach had to be taken to find the absolute value of  $NPS_{det}(f)$  by measuring DQE(0) as follows. The detector array was irradiated using an open 5 x 5 cm<sup>2</sup> Co<sup>60</sup> beam and 50000 readings for each crystal were obtained using a 0.7 ms integration period and a SDD of 110 cm. This data was corrected for dark current and gain variations. Another set of the same data was collected and then subtracted from the first set to obtain noise only data. The noise power spectrum, NPS(f), was then calculated from the noise only data using the approach given by Williams et al. (1999). Absolute DQE(0) is then given by (Lachaine et al., 2001)

$$DQE(0) = \frac{MTF^2(0)}{(NPS(0)/d^2)\varphi} \quad (3.45)$$

where  $\varphi$  is the photon fluence impinging on the detector in a uniform open beam, and  $d$  is the average detector signal. The photon fluence per unit data collection interval can be calculated from the relationship between fluence and dose rate in

free space for 1.25 MeV photons of electronic equilibrium (Johns and Cunningham, 1983) using the following equation :

$$D = \Psi \left( \frac{\mu_{en}}{\rho} \right)_{tissue} = E \cdot \phi \cdot \left( \frac{\mu_{en}}{\rho} \right)_{tissue}$$

$$\rightarrow \phi = \frac{1 \mu\text{Gy}}{1.25 \text{ MeV} \cdot 0.00297 \text{ m}^2/\text{kg}} = 1.6812 \times 10^3 \frac{\text{photons}}{\text{mm}^2 \cdot \mu\text{Gy}} \quad (2.46)$$

where  $D$  is the dose,  $\psi$  is the energy fluence,  $\left( \frac{\mu_{en}}{\rho} \right)_{tissue}$  is the tissue mass energy absorption coefficient,  $E$  is the energy of each photon assumed to be 1.25 MeV, and  $\phi$  is the photon fluence per  $\mu\text{Gy}$ . The photon fluence per data collection interval  $\phi$  was then obtained by multiplying  $\phi$  by the dose calculated from equation (3.12). Since  $NPS$  and  $d$  in equation (3.45) are measured with an open beam,  $NPS$  contains the effect of the finite size of the  $\text{Co}^{60}$  source that is not accounted for in the model. Therefore, equation (3.45) is only used for normalizing the measured DQE (0).

Our experimental set-up in the 6 MV photon beam was similar to the one in the  $\text{Co}^{60}$  beam. Our detector measures the signal due to radiation in a linac beam (Varian 600C) on a pulse to pulse basis. The variations in the output of the linac are too large from pulse to pulse. Hence, we were unable to distinguish between the noise correlation among detector channels and the common noise in all channels due to the linac output. Thus, the absolute  $NPS(f)$  and  $DQE(f)$  were not measured in a 6 MV beam. The experimental set-up for these measurements is shown in Figure 3.19 for the  $\text{Co}^{60}$  case.

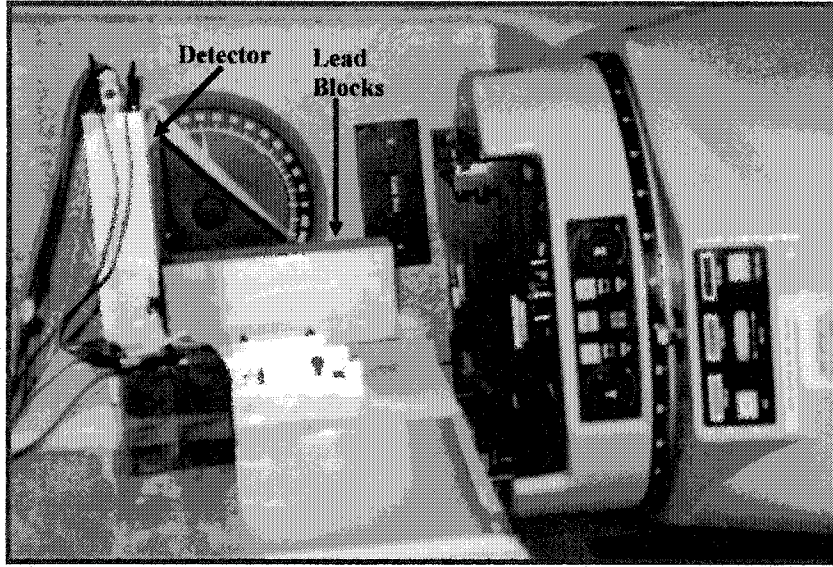


**Figure 3.19:** Experimental set-up for finding the imaging characteristics of our prototype detector.

### 3.6.3 Checking the Upper Limit of DQE(f)

To check the method used to get our DQE(0), we employed a method suggested by Swank (Swank, 1973). This method gives us the DQE(0) of our detector assuming no optical degradation of the signal. This method employs absorbed energy distributions or AEDs. The AED, as a function of energy  $E$ , gives the number of x-ray photons that deposit energy  $E$  in the crystal. Once the AED is known, the energy moments can be calculated using the following formula (Cho et al., 2001; Swank, 1973):

$$M_n = \int_E S(E) E^n dE \quad (3.47)$$

where  $M_n$  is the  $n^{\text{th}}$  energy moment,  $S(E)$  is the AED, and  $E$  is the amount of energy deposited in the scintillation crystals. Our energy resolution for

determining the AEDs from the output of EGSnrc is 0.01 MeV. An upper bound on the DQE(0) is then given by (Cho et al., 2001; Swank, 1973):

$$DQE(0) = \frac{M_1^2}{M_2} \quad (3.48)$$

## References:

- <sup>1</sup> Berndt A.G., "A Fourth Generation 192Ir Source-Based CT scanner for Brachytherapy", PhD thesis, University of Manitoba (2002).
- <sup>2</sup> Bushberg J.T., Seibert J.A., Leidholdt E.M., Boone J.M., *The Essential Physics of Medical Imaging*, (Lippincott Williams & Wilkins, Philadelphia, 2002).
- <sup>3</sup> Cho G., Kim H. K., Chung Y. H., Kim D. K., Lee H. K., Suh T. S., and Joo K. S., "Monte Carlo analyses of x-ray absorption, noise and detective quantum efficiency considering therapeutic x-ray spectrum in portal imaging detector," *IEEE Trans. Nuc., Trans., Sci.* 48: 1423-1427(2001).
- <sup>4</sup> Derenzo, S. and Moses W. W., "Experimental efforts and results in finding new heavy scintillators", Proceedings of the CRYSTAL 2000 International Workshop on Heavy Scintillators for Scientific and Industrial Applications, Chamonix, France, 125-135( 1992).
- <sup>5</sup> Duclos S. J., "Scintillator phosphors for medical imaging," *The Electrochemical Society Interface*, 34-38 (1998).
- <sup>6</sup> Glover G.H. and Eisner R.L, "Theoretical resolution of computed tomography systems," *J. Comput. Assist. Tomog.* 3: 85-91 (1979).
- <sup>7</sup> Johns H.E., Cunningham J.R., *The Physics of Radiology*, 4<sup>th</sup> ed. (Thomas, Springfield, IL, 1983).
- <sup>8</sup> Kausch C., Schreiber B., Kreuder F., Schmidt R., Dossel O., "Monte Carlo simulation of the imaging performance of metal/phosphor screens used in radiotherapy", *Med.Phys.* 26: pp. 2113-2124(1999).
- <sup>9</sup> Kawrakow I. and Rogers D. W. O., "The EGSnrc code system: Monte Carlo Simulation of electron and photon transport," NRCC Report PIRS-701(2002).
- <sup>10</sup> Kinloch D. R., Novak W., Raby P., and Toepke I., "New developments in Cadmium Tungstate", *IEEE Trans. Nucl. Sci.*, 41: pp .752-754 (1994).
- <sup>11</sup> Krus D. J., Novak W. P., Perna L., " Precision linear and two-dimensional scintillation crystal arrays for x-ray and gamma ray imaging applications," Presented at The SPIE International Symposium on Optical Science, Engineering and Instrumentation, July 18-23, 1999, Hard X-ray, Gamma-Ray and Neutron Detector Physics (SPIE Vol. 3768) .

- <sup>12</sup> Lachaine M., Fourkal E., Fallone B.G., “Detective quantum efficiency of a direct-detection active matrix flat panel imager at megavoltage energies”, *Med. Phys.* 28: 1364-1372 (2001).
- <sup>13</sup> Levin A. and Moisan C., “A more physical approach to model the surface treatment of scintillation counters and its implementation into DETECT,” in 1996 IEEE Nuclear Science Symp. Conf. Rec. 2, pp. 702-706 (1997).
- <sup>14</sup> Pedrotti F. L., Pedrotti L. S., *Introduction to Optics*, Prentice Hall (Upper Saddle River, NJ ,1993).
- <sup>15</sup> Rizzoni G., *Principles and Applications of Electrical Engineering*, 3rd Ed. (McGraw-Hill, 2000).
- <sup>16</sup> Rogers, D., EGSnrc Reference Manual,  
<http://www.irs.inms.nrc.ca/inms/irs/EGSnrc/pirs701/node58.html> (2002)
- <sup>17</sup> Sheikh-Bagheri D., and Rogers D.W.O., “Monte Carlo calculation of nine megavoltage photon beam spectra using the BEAM code,” *Med. Phys.* 29: 391-402 (2002).
- <sup>18</sup> Swank R. K., “ Absorption and noise in x-ray phosphors,” *J. Appl. Phys.* 44: 4199-4203 (1973).
- <sup>19</sup> Williams M. B. , Mangiafico P. A. , Simoni P. U., “Noise power spectra of images from digital mammography detectors”, *Med.Phys.*26: 1279-1293(1999).
- <sup>20</sup> [www.bicron.com](http://www.bicron.com) [manufacturer of the crystals used in this study]
- <sup>21</sup> [www.hamamatsu.com](http://www.hamamatsu.com) [manufacturer of the photodiodes used in this study]
- <sup>22</sup> [www.gel.ulaval.ca/detect](http://www.gel.ulaval.ca/detect) [DETECT2000 software website]



## Chapter 4: RESULTS AND DISCUSSION

The results of the Monte Carlo and experimental studies described in Chapter 3 are presented and discussed in this chapter. The first set of results examines the characteristics of single CsI(Tl) and CdWO<sub>4</sub> crystals. These results include the afterglow assessment, a comparison of the modeled and measured signals as a function of crystal height when these two types of crystals are placed in a Co<sup>60</sup> beam under identical conditions, along with the corresponding details of the optical photon simulations in DETECT2000. The second set of results is concerned with the linearity of response to dose of the (CdWO<sub>4</sub>) detector array, and with measuring attenuation both in open and blocked Co<sup>60</sup> beams. The third set of results presents the imaging characteristics of the prototype detector array both in Co<sup>60</sup> and 6 MV beams. In this section, the modeled and measured line spread function (LSF), frequency dependent modulation transfer function (MTF(f)), noise power spectrum (NPS(f)), and detective quantum efficiency (DQE(f)) of the detector are given in Co<sup>60</sup> and 6 MV beams. It is also shown why we are not able to measure the NPS (f) and hence the DQE (f) in the 6 MV beam. This last set of results also contains information regarding the LSF, MTF(0) and DQE(0) of the detector assuming that all the optical photons created in the CdWO<sub>4</sub> crystals are detected by the photodiodes; as such the effect of optical photon transport on the degradation of the imaging characteristics of the detector is investigated.

## 4.1 Single Crystals

### 4.1.1 Afterglow Assessment

Figure 4.1 shows the afterglow measurements for the single crystals of CsI(Tl) and CdWO<sub>4</sub> (0.275 x 0.8 x 1.0 cm<sup>3</sup>) performed in a radiotherapy simulator beam. During the beam-on time, the absolute signal in CsI(Tl) was about 6 times higher than CdWO<sub>4</sub>. This is due to lower self-absorption, better optical spectral match with the photodiode (Figures 3.10, 3.11, 3.12 and 3.13) and higher optical yield (Table 3.1) per MeV absorbed in CsI(Tl) than CdWO<sub>4</sub>. This data suggests the absolute DQE(f) may be higher for CsI(Tl) than CdWO<sub>4</sub> if the array detector is formed from CsI(Tl). However, we found that CsI(Tl) retained about 0.5% of the beam on signal at 60 ms after the beam was turned off due to the afterglow compared to only 0.02% for CdWO<sub>4</sub>. Such a large after glow in CsI(Tl) is undesirable even for the slower scan time of MVCT since the time between collection of various fan-beam projections is still of the order of tens milliseconds. For the modern diagnostic CT scanners with scan times <1 s, it is desirable to have an after glow of <0.01% at ~ 3 msec (Eijk, 2002). Moreover, CsI(Tl) is hygroscopic and not easy to handle. Therefore, the array detector was not made from CsI(Tl).

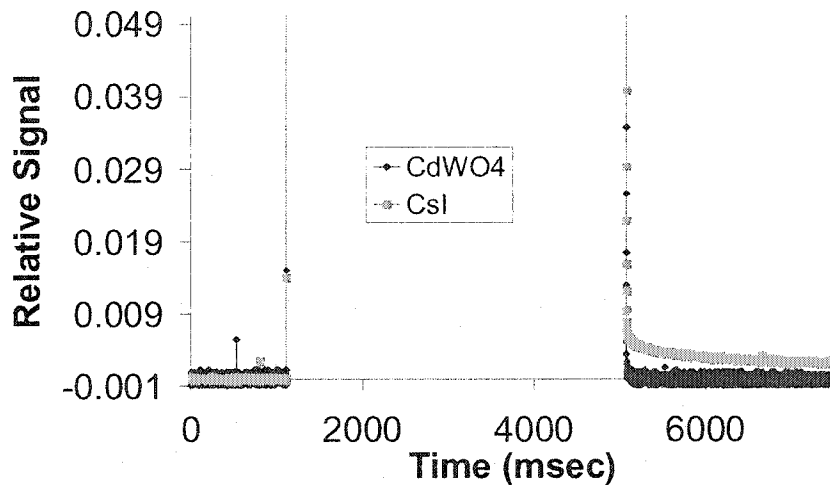


**Figure 4.1:** Afterglow Assessment of 1 cm long CdWO<sub>4</sub> and CsI(Tl) Crystals: The signal in both crystals is normalized to the corresponding signal when the radiation is on. The signal in CdWO<sub>4</sub> falls to 0.02% 60 ms after the radiation is off, compared to 0.5% in CsI(Tl). Technique: Radiographic mode in a Model Super 800 CP, Phillips Medical Systems radiographic simulator beam at 100 kV and 40 mA.

#### 4.1.2 Detector Signal as a Function of Crystal Height

The measured and modeled signals as a function of crystal height for CdWO<sub>4</sub> and CsI(Tl) in a Co<sup>60</sup> beam are shown in Figure 4.2. Except for a 0.4 cm tall CsI(Tl) crystal, the modeled and measured signals are in good agreement. The data for both the modeled and measured signals are normalized such that mean modeled and measured values for all crystals are both unity. The signal in CdWO<sub>4</sub> crystals levels off more rapidly with crystal height than CsI(Tl) due to the higher self-absorption in CdWO<sub>4</sub>. The importance of these results lies in the agreement between the measured and modeled signals. The good agreement between

measured and modeled signal serves as a validation of our use of DETECT2000 and the parameters employed in defining the geometry of the single crystals, especially for the reflection coefficient for the Teflon tape coating.

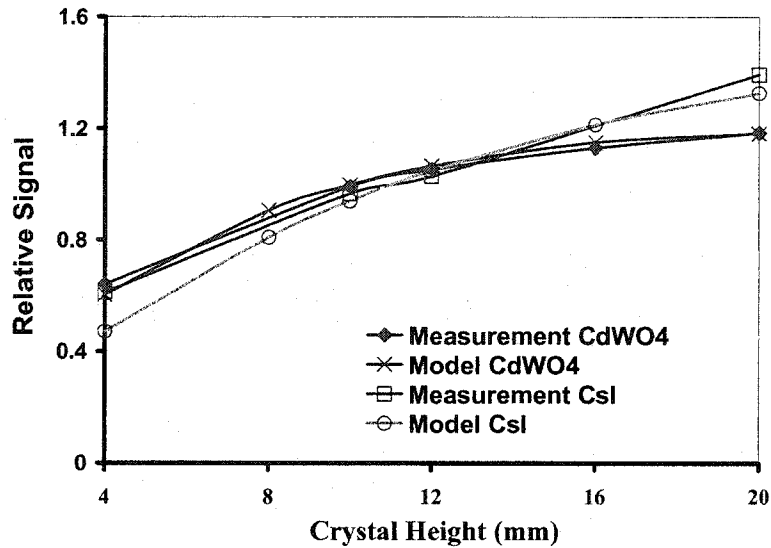


**Figure 4.2:** The normalized measured and modeled signals as a function of crystal height for both CdWO<sub>4</sub> and CsI(Tl) crystals under identical conditions in a Co<sup>60</sup> beam.

The results of optical photon transport simulations in DETECT2000 are shown in Figure 4.3. The detected fraction is the fraction of photons which have made their way to the photodiodes. The difference in bulk absorption between CsI(Tl) and CdWO<sub>4</sub> is again quite significant. It is clear from Figure 4.3 that both the bulk absorption (self-absorption) and absorption in the coated surfaces is increased as the crystal height is increased. This is the main reason that detector signal will level off at some crystal height, where the increased energy deposition due to x-ray photons is counterbalanced by a reduced fraction of detected optical photons. Since the self absorption is larger in CdWO<sub>4</sub> than CsI(Tl), the detector

signal for CdWO<sub>4</sub> levels off for a smaller crystal height than CsI(Tl). Another reason for having a higher signal as a function of height in CsI(Tl) is a better match between the spectrum of optical photons created and the photodiode sensitivity spectrum. (Figures 3.11 and 3.13).

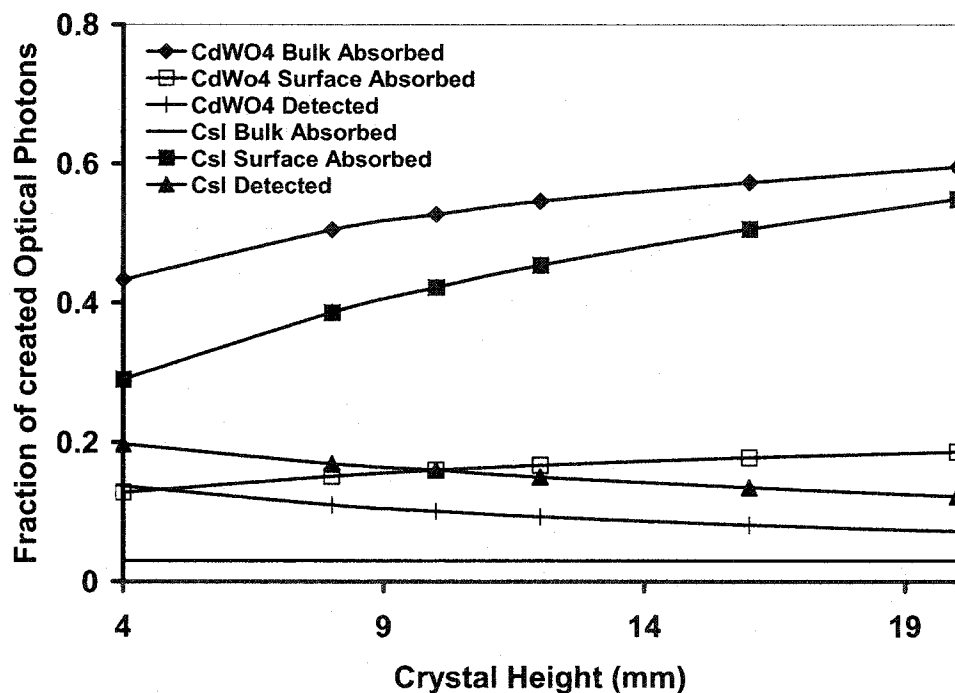


**Figure 4.3:** Results of Optical Simulations for Single Crystals in DETECT2000: Fraction of optical photons that are absorbed in crystal bulk and surfaces, and that are detected by the photodiode. The remaining fraction, not shown in the figure, is transmitted through the photodiode due to the mismatch between emission and sensitivity spectra.

#### 4.2 Linearity of the CdWO<sub>4</sub> Array Detector

The imaging characteristics of a detecting system can only be quantified using the MTF(f), NPS(f) and DQE(f) if the system is linear (Bushberg et al., 2002). Even though, in the real world this assumption of linearity only applies

approximately within a certain range of operation, it is still a requirement for quantifying the imaging characteristics.

#### **4.2.1 Detector Dose Response**

Figure 4.4 shows the mean detector signal as a function of dose in free space (dose to small amount of tissue in air) at the location of the detector. It can be seen that the detector's response with dose is fairly linear. Differences in the signal magnitude for various channels arise due to various factors such as non-uniform thickness of optical glue, photodiode sensitivity variations, etc. The small differences in the slope of the lines are caused by radiation scattered from a crystal to its neighbours. As such, the inner channels (e.g. 4 and 5) may have a slightly steeper response than outer channels (e.g. 1 and 8) due to the increased detection of lower energy scattered radiation from neighbours. Since the dose in free space is proportional to the energy fluence incident on the detector, it can be assumed that the detector response to incident energy fluence is also linear.

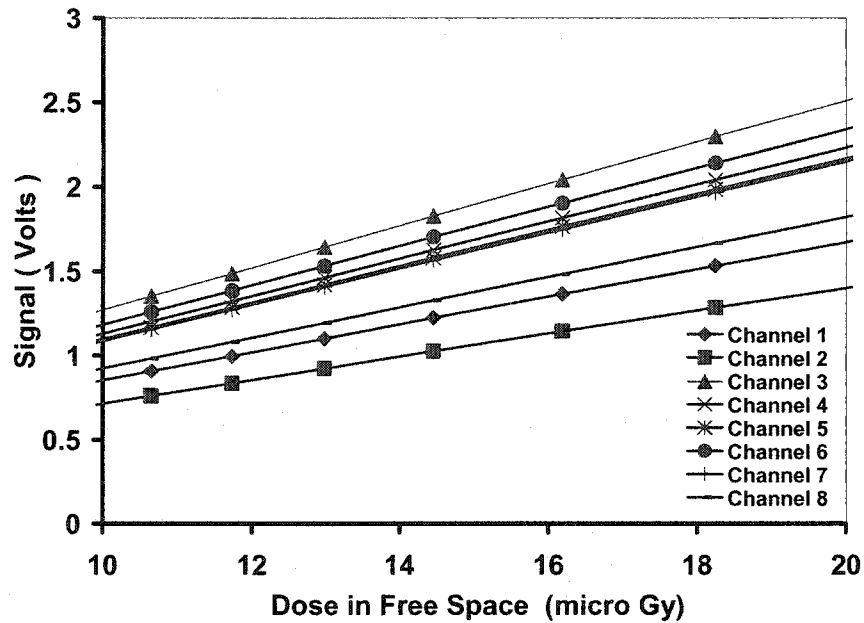


**Figure 4.4:** Dose Response of the Prototype Detector: Response of the 8-channel CdWO<sub>4</sub> array as a function of dose in free space in a Co<sup>60</sup> beam.

#### 4.2.2 Measurement of Beam Attenuation

Figure 4.5 shows the attenuation as a function of solid water thickness for a narrow Co<sup>60</sup> beam. Attenuation is defined as follows:

$$I = I_0 e^{-\mu x}$$

where  $I_0$  is the incident photon fluence and  $I$  is the output fluence after passing through a thickness,  $x$ , of interacting medium,  $\mu$  is the attenuation coefficient of the interacting medium. In Figure 4.5, the  $\ln(I_0/I)$  is plotted against  $x$ .

The straight line shown in this graph is the linear regression line through the attenuation data as measured by channel 8. This data clearly shows that the

detector will linearly measure the attenuation profiles required for CT image reconstruction. Since the thickness of solid water slabs was uniform, all the detectors show the same attenuation values. The slope of this curve will give the attenuation coefficient of the solid water in a  $\text{Co}^{60}$  beam. As expected, no spectral hardening occurs for the  $\text{Co}^{60}$  beam, which would have resulted in a downward deviation from a straight line for larger solid water thicknesses.

Beam hardening occurs for polyenergetic beams where a larger fraction of low energy photons interact with the medium compared to that of high energy photons, consequently the mean energy of  $I$  is slightly higher than  $I_0$ .

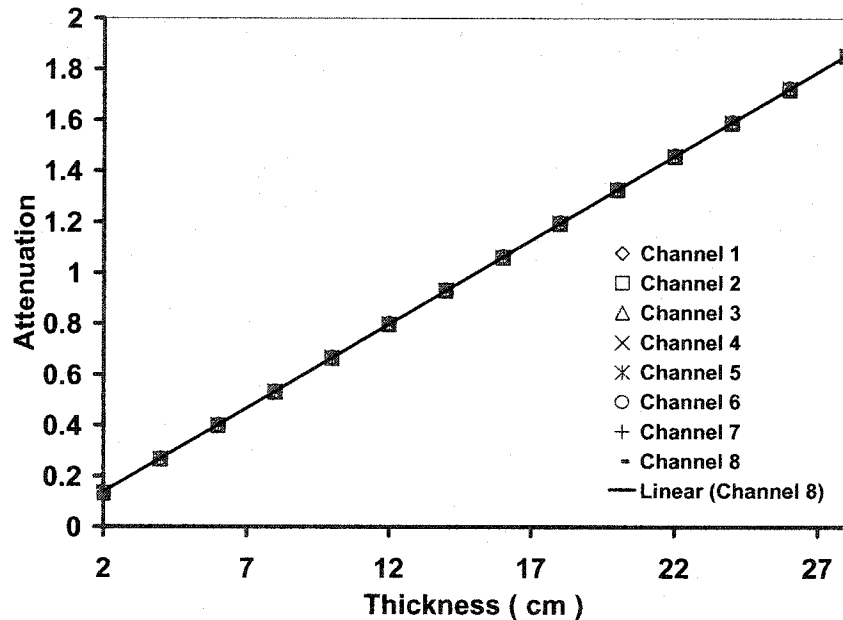


**Figure 4.5:** Attenuation Response of the Prototype Detector: The attenuation as a function of thickness of solid water for a narrow 1.25MeV beam measured by the  $\text{CdWO}_4$  detector array. The linear regression line for channel 8 data is also shown.



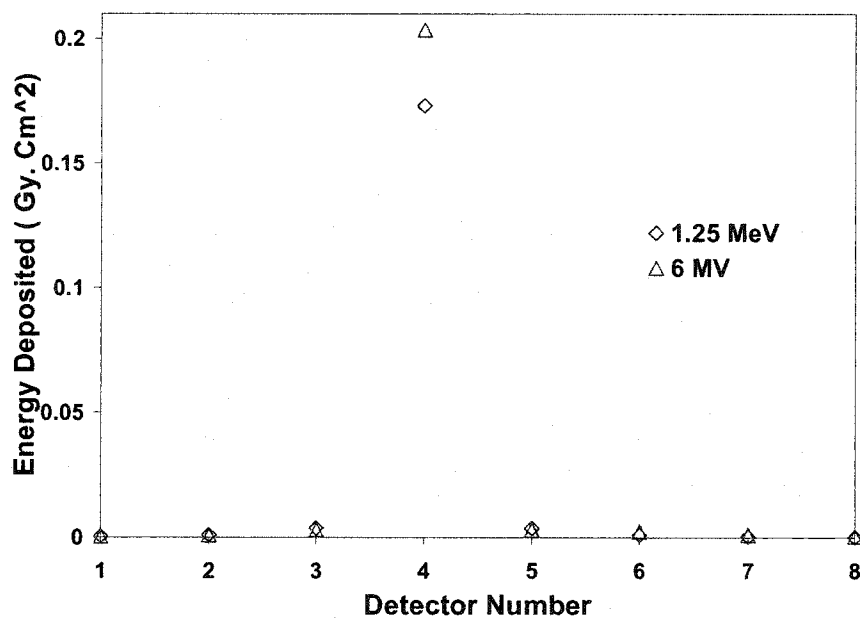
### 4.3 Imaging Characteristics Studies Performed on the CdWO<sub>4</sub> detector

#### 4.3.1 Gamma Photon Energy Deposition

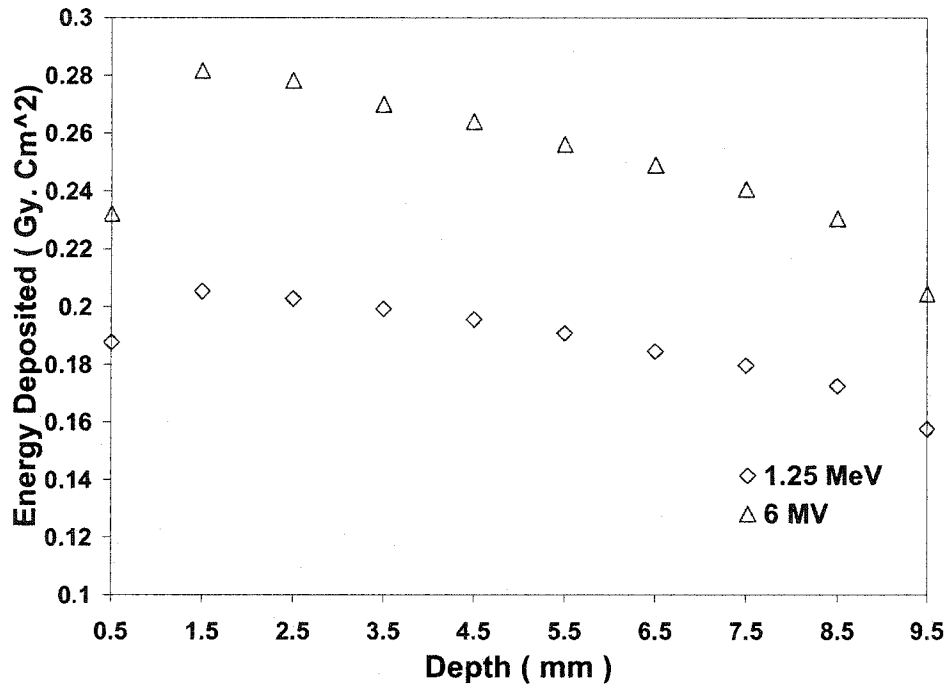
Figure 4.6 shows the energy deposited in Gy.cm<sup>2</sup> (i.e. the dose deposited in each voxel per incident fluence) in each crystal of the 8-element detector array when a slit (in y-direction of Figure 3.17) beam was incident in the middle of the fourth crystal. The input source geometry, described in section 3.6.1, was used for both 1.25 MeV and 6 MV photon beams. The pattern of the x-dependent energy deposition for these two energies is very similar. This is due to the fact that the mean energy of the 6 MV spectrum (Figure 3.18) is only slightly larger than 1.25 MeV. However, the energy deposited in the fourth crystal is higher for the 6 MV beam compared to the 1.25 MeV beam since higher energy photons deposit more energy per interaction in the crystals. As seen in Figures 4.6, almost all of the energy is deposited in the fourth crystal. Therefore, the spread of the energy deposition among the crystals in the array is very small for both energies. The energy deposited in crystals three and five is about 2 % of the energy deposited in crystal four for 1.25 MeV photons and 1.5 % for 6 MV photons. The ratio of the energy deposited in crystals three and five to the energy deposited in the fourth crystal is about 0.5 % lower in the 6 MV beam compared to the 1.25 MeV beam. This is due to the more forward scattering of the Compton photons at higher energies. (Johns and Cunningham, 1983)

Figure 4.7 shows the energy deposited in Gy.cm<sup>2</sup> as a function of depth (z), averaged over 8 crystals of the prototype detector array, as a result of 1.25 MeV and 6 MV slit beams incident in the middle of fourth crystal (Figure 3.17). The input source geometry is described in section 3.6.1. The pattern of the depth-dependent energy deposition for these two photon beam energies is very similar. Again, this is due to the fact that the mean energy of the 6 MV spectrum (Figure

3.18) is only slightly higher than 1.25 MeV. As expected the energy deposited in the detector at each depth is higher for the 6 MV beam. The build-up region (Johns and Cunningham, 1983) of energy deposition occurs up to a depth of 1.5 mm for both photon beam energies.



**Figure 4.6:** Simulated Energy Deposition for 1.25 MeV and 6 MV Photons: The energy deposited in each crystal (i.e. the energy deposited as a function of x) as simulated in EGSnrc in the prototype CdWO<sub>4</sub> detector array from 1.25 MeV and 6 MV slit beams incident in the middle of the fourth crystal is shown.



**Figure 4.7:** Simulated Energy Deposition for 1.25 MeV and 6 MV Photons: The energy deposited in the prototype CdWO<sub>4</sub> detector array as a function of depth (z) from 1.25 MeV and 6 MV slit beams incident in the middle of the fourth crystal and simulated in EGSnrc is shown.

### 4.3.2 Optical Photon Transport

The results described in this section pertain to the optical simulations performed in DETECT2000 for the 8-element CdWO<sub>4</sub> detector array for the purpose of determining the optical LSF.

Figure 4.8 shows the optical LSF,  $l(n; n', z)$ , as a function of the photodiode number  $n$ . These LSFs were calculated for optical line sources located at the five voxels within the fourth crystal in the x-direction (i.e.  $n' = 1-5$ ) at a fixed depth of 4.5 mm (i.e.  $z = 5$ ). A total of 80,000 optical photons were simulated for each line source, and the number of optical photons detected in each

photodiode was determined. It is apparent from Figure 4.8, that there is a very small  $n'$  dependence in the optical LSFs. These results indicate that we could replace the superposition in equation 3.37 with convolution in our future studies without any significant errors introduced in our results. Optical spreading occurs mostly through the glue and reflection off the metallic surface on the photodiode array.

Figure 4.9 shows the optical LSFs,  $l(n; n', z)$ , for the optical line sources at 0.5 mm and 9.5 mm depths in the central voxel of the fourth crystal in the  $x$ -direction (i.e.  $n' = 3$  and  $z = 1, 10$ ). Each line source was simulated to contain 80,000 optical photons in DETECT2000. It is apparent from Figure 4.9, that there is a slight  $z$  dependence (about 0.2% change in detected photons for the fourth crystal over 1 cm) in the optical LSFs for 1 cm long crystals. The  $z$  dependence is similar for the other  $n'$  values. This is due to the fact that the absorption mean free path of the optical photons in  $\text{CdWO}_4$ , as shown in Figure 3.12, is large compared to the height of the crystals. Another reason is that, since the optical photons are generated isotropically in DETECT2000, only a small fraction of the photons fall in the solid angle that faces the photodiodes. The difference in the size of this angle as a function of depth of photon generation is small and hence the height dependence of the optical LSFs is also small. It should be remembered that as the height of the crystals increases, this depth dependence becomes more pronounced (see Chapter 5).

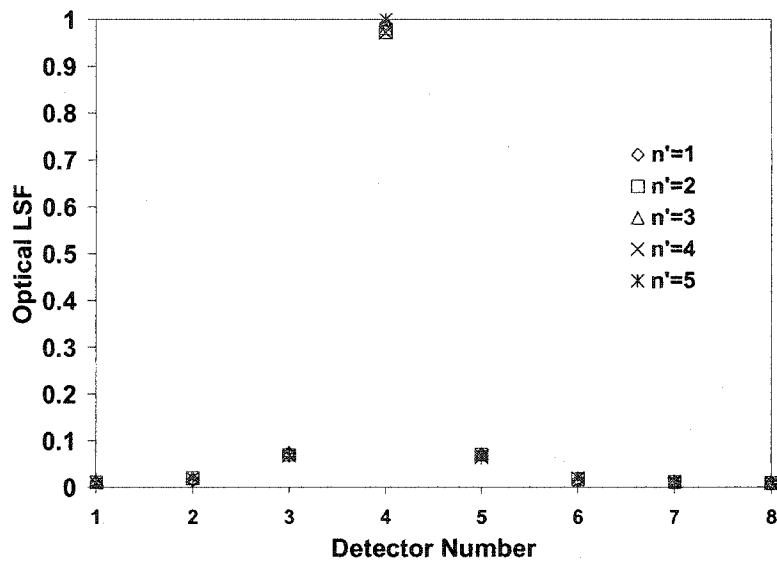


**Figure 4.8:** The optical LSF for various locations of line sources in the x-direction (i.e.  $n' = 1 - 5$ ) and at a depth of 4.5 mm within the fourth crystal. Each line source was simulated to have 80,000 optical photons in DETECT2000.

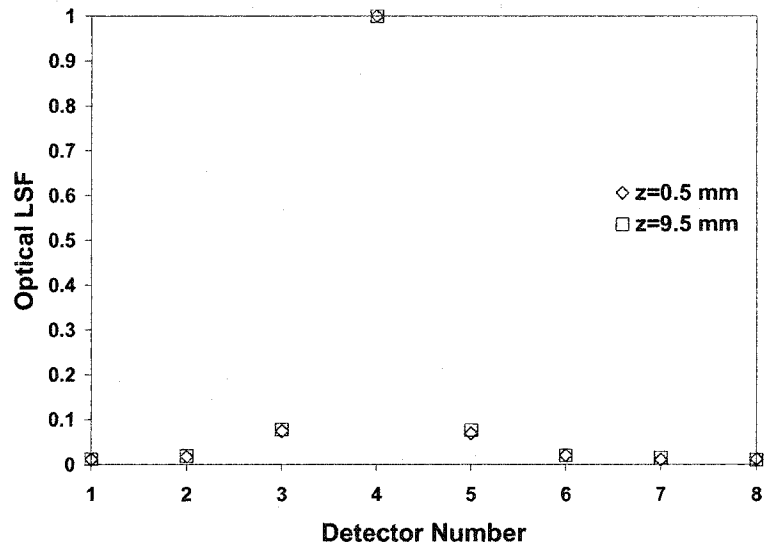


**Figure 4.9:** The optical LSFs for line sources at 0.5 mm and 9.5 mm depths in the central voxel of the fourth crystal in the x-direction. Relative number of optical photons detected in each photodiode is displayed for each line source simulated with 80,000 optical photons in DETECT2000.

Figures 4.10 to 4.13 show the fraction of detected, bulk absorbed, surface absorbed, and transmitted optical photons respectively, as a function of the depth of the optical line source generated in the middle of fourth crystal. Except for statistical noise, the shape of these graphs is as expected. More optical photons are detected when the line source is closer to the photodiodes (larger depths). Similarly, fewer optical photons are bulk or surface absorbed, as the line source gets closer to the photodiodes because the mean path length and average number of surface collisions in the crystal are lower. A larger fraction of optical photons is transmitted as a result of the mismatch between the photosensitivity of the photodiodes and the emission spectra of the crystal at larger depths, since more photons actually hit the photodiodes. It is shown in Figure 3.13 that approximately 20% of the photons which do hit the photodiodes are not detected. Therefore, in future optimization of the detector, it might be beneficial to choose a photodiode with a better spectral match.

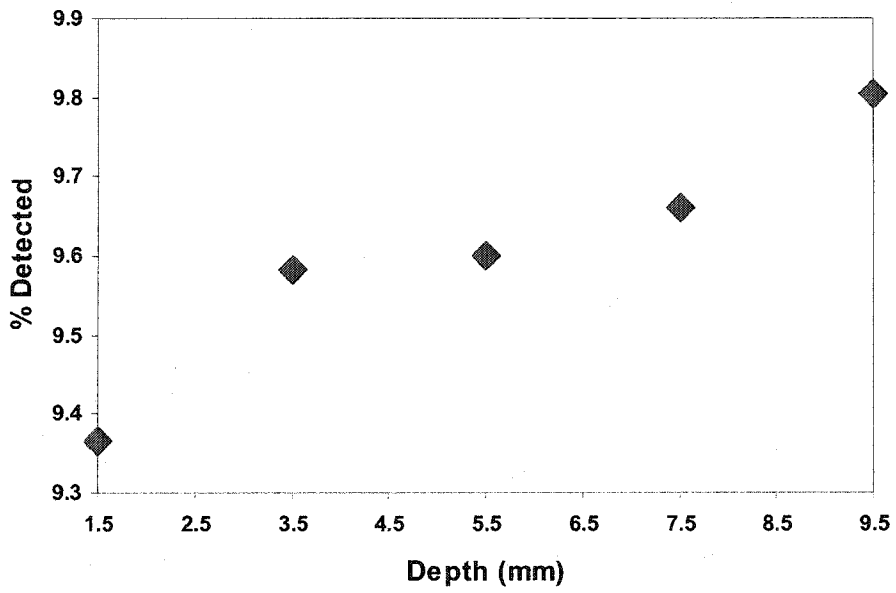


**Figure 4.10:** Simulated fraction of detected optical photons as a function of the depth of the optical line source at the center of the fourth crystal in the CdWO<sub>4</sub> detector array.

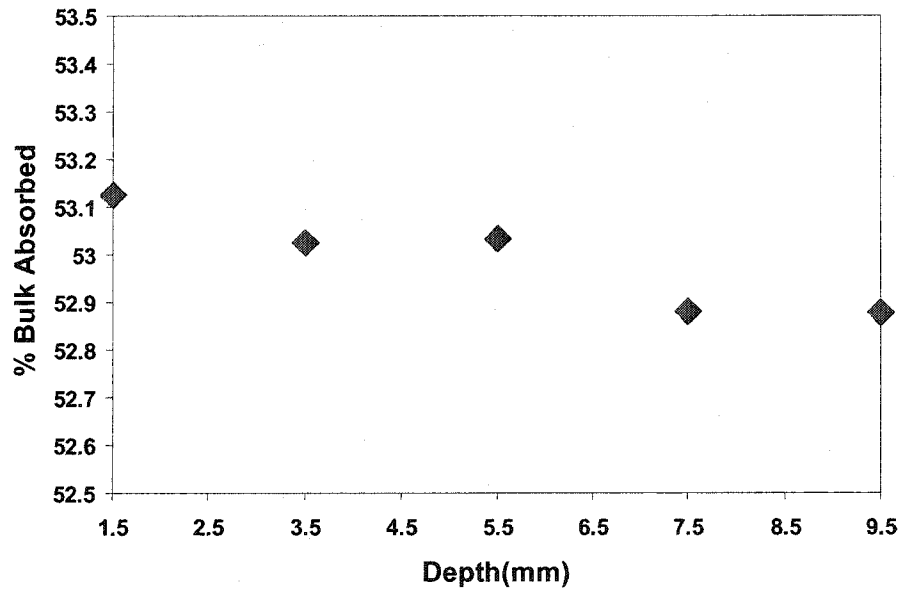


**Figure 4.11:** Fraction of bulk absorbed optical photons as a function of the depth of the optical line source at the center of the fourth crystal in the CdWO<sub>4</sub> detector array calculated by DETECT2000.

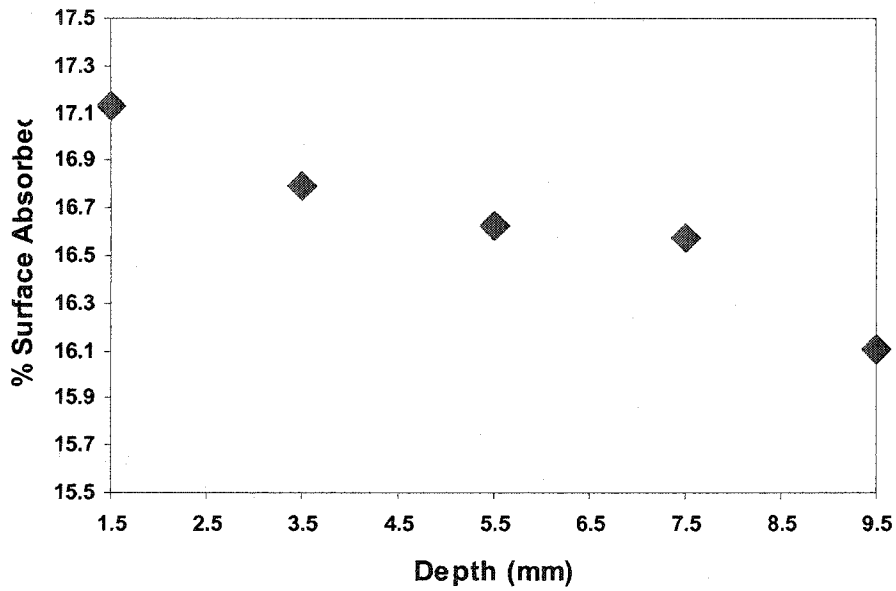


**Figure 4.12:** Fraction of surface absorbed optical photons as a function of the depth of the optical line source at the center of the fourth crystal in the  $\text{CdWO}_4$  detector array as predicted by the simulations performed in DETECT2000.

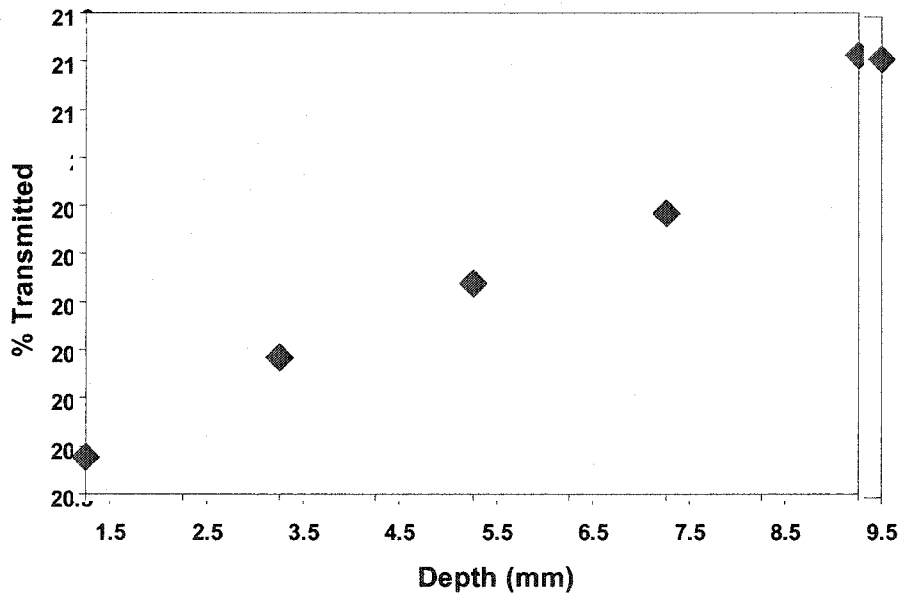


**Figure 4.13:** Simulated fraction of the transmitted optical photons as a function of the depth of the optical line source at the center of the fourth crystal in the  $\text{CdWO}_4$  detector array of as predicted by simulations performed in DETECT2000.



### 4.3.3 Checking the Upper Limit of DQE(0)

The AEDs within the CdWO<sub>4</sub> detector array for the Co<sup>60</sup> and 6 MV slit beams are shown in Figure 4.14. The very distinct peak seen at 1.25 MeV in Figure 4.14 (a) reflects the large probability of  $\gamma$  photons depositing all of their energy in 1 cm high CdWO<sub>4</sub> crystals. The smaller peak observed at approximately 1.05 MeV is the Compton edge (Johns and Cunningham, 1983). The shape of the 6 MV photon AED is a spectrum as expected since the input is also a spectrum (Figure 3.18). Table 4.1 shows the first, second and third moments of the AEDs i.e.  $M_0$ ,  $M_1$  and  $M_2$  as calculated by equation 3.47, and DQE(0) as given by equation 3.48, for 1.25 MeV and 6MV photons. The value for DQE(0) reported in Table 4.1 is an upper limit as it does not consider image degradation due to optical photon transport.

**Table 4.1:** The results of the preliminary assessment of DQE(0) for the CdWO<sub>4</sub> detector array, using the output of EGSnrc.

Energy	$M_0$ (Quantum Efficiency)	$M_1$	$M_2$	DQE(0)
1.25 MeV	0.33	0.25	0.25	0.26
6 MV	0.37	0.35	0.65	0.19

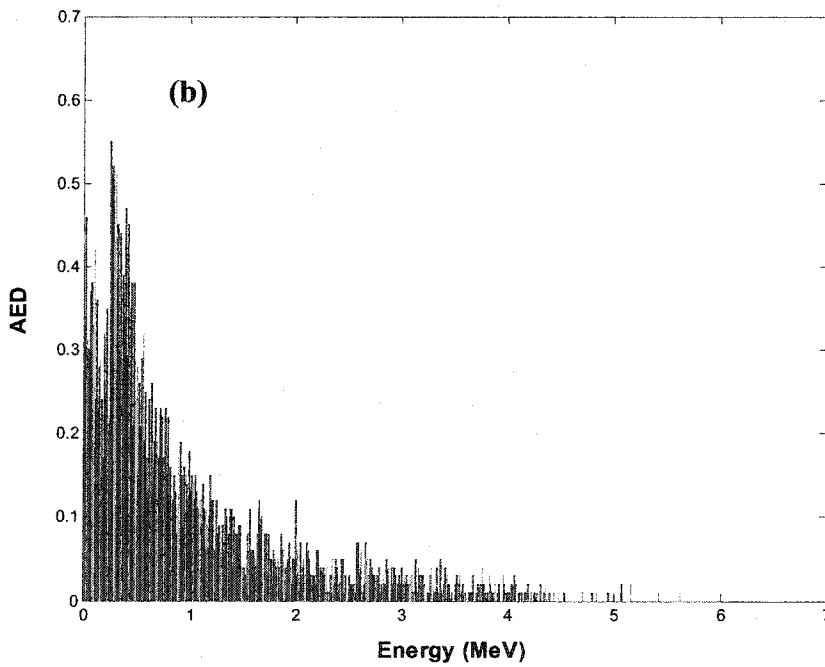
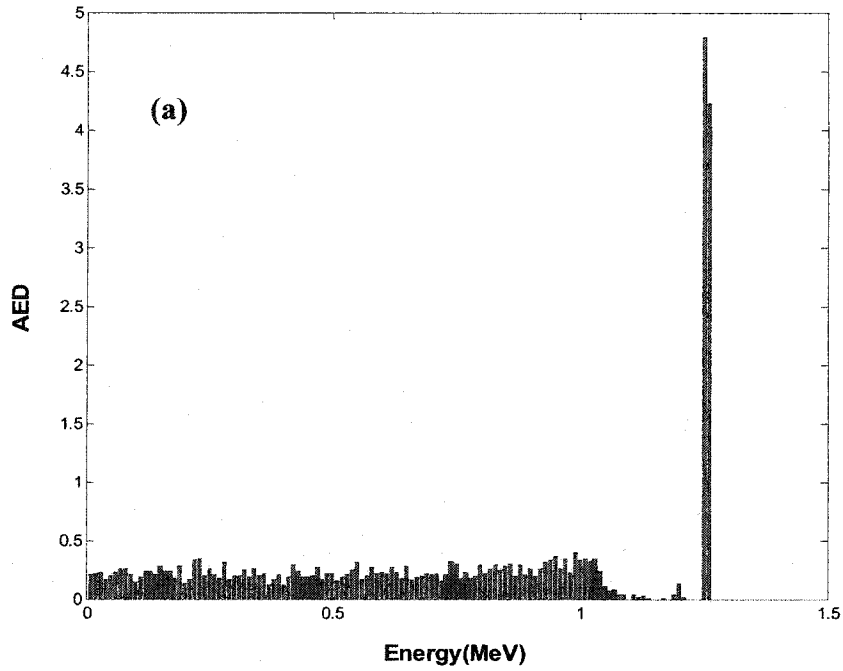


**Figure 4.14:** Absorbed energy distributions (% of number of histories) for (a) 1.25 MeV photons and (b) 6MV photons as given by the output of EGSnrc for 100000 histories.

#### 4.4 Measured and Modeled LSF, MTF(f), NPS(f) and DQE(f)

Figures 4.15 to 4.18 show the measured and modeled LSF, MTF(f), relative  $NPS_{det}(f)$  and DQE(f) respectively for the  $CdWO_4$  detector array in a  $Co^{60}$  beam. These graphs show that the modeled and measured values of the detector characteristics are in good agreement. The worst discrepancy between the measured and modeled MTF, NPS and DQE are 1.5, 1.2 and 1.9% respectively.

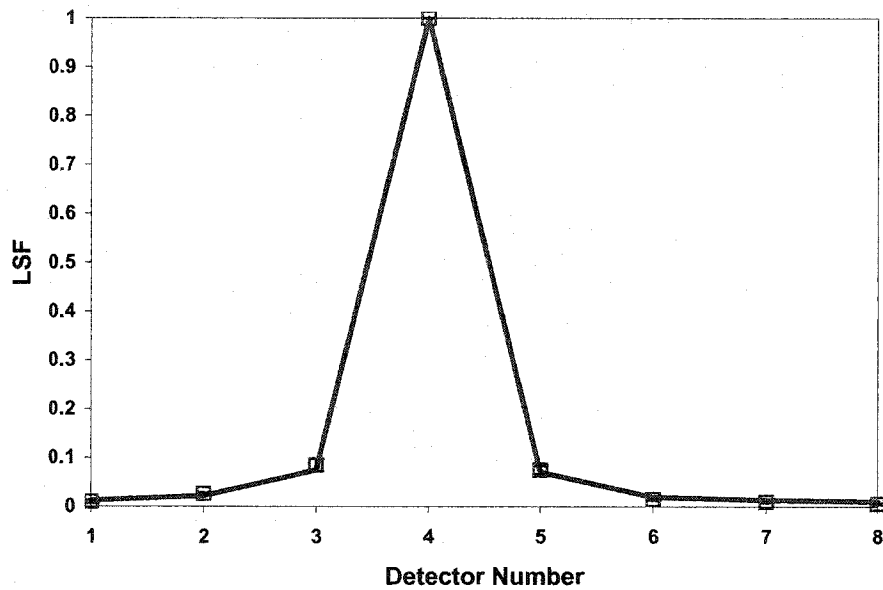


**Figure 4.16:** The modeled (line) and measured (squares) MTF(f) for the 8-element crystal array in a 1.25 MeV beam.

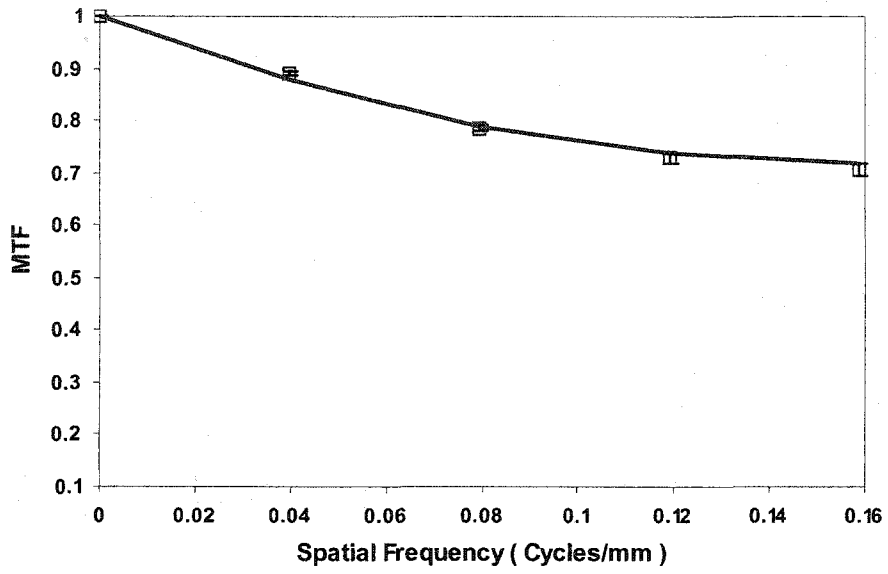


**Figure 4.15:** The modeled (line) and measured (squares) LSF for the 8-element crystal array in a 1.25 MeV beam.

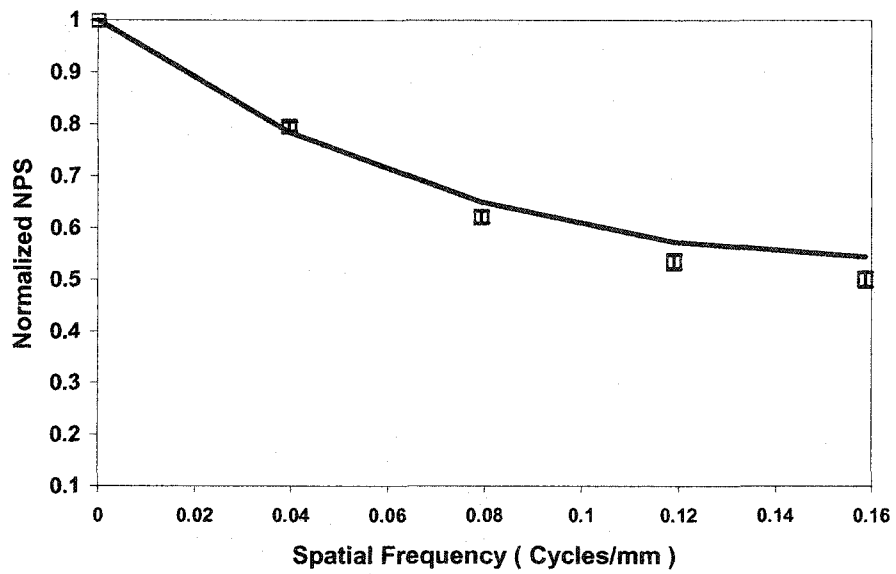


**Figure 4.17:** The modeled (line) and measured (squares) normalized  $NPS_{det}(f)$  for the 8-element crystal array in a 1.25MeV beam.

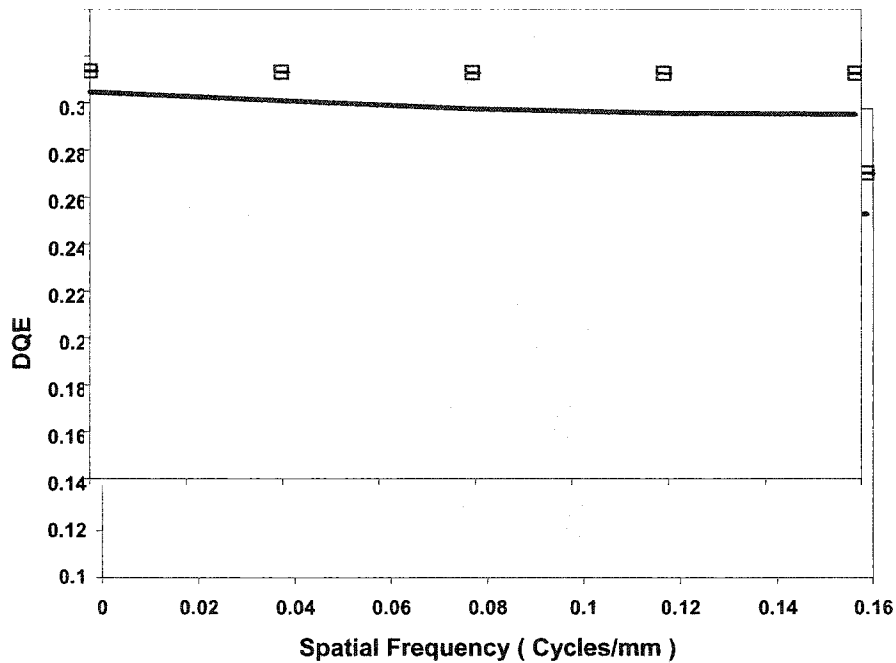


**Figure 4.18:** The modeled (line) and measured (quares) DQE(f) for the 8-element crystal array in a 1.25 MeV beam.

The modeled and measured MTF(f) for 6MV photons are shown in Figure 4.19. The worst discrepancy in this case is 2.5%. Figures 4.20 and 4.21 show the modeled  $NPS_{det}(f)$  and DQE(f) for 6 MV photons. We were not able to measure the  $NPS_{det}(f)$  due to the pulse to pulse fluctuations in the output of the linear accelerator. These fluctuations are depicted in figure 4.22. Figure 4.22(a) shows the signal for 50 pulses. The Figure 4.22(b) is a more global view of the fluctuations. The signal in all eight channels is shown only for the pulses where the radiation is on. The signals are corrected for the dark current and normalized to the mean detector signal. While these fluctuations are too small to create any clinical problems, they are still on the same order as the co-relational noise among detector channels.

The calculation of  $NPS_{det}(f)$  relies on temporal averaging of the Fourier transform of the noise among 8 channels. Because of the relatively large pulse to

pulse fluctuations, this procedure shows an erroneously large value for  $NPS_{det}(0)$  since all the channels are fluctuating in an identical manner. If this detector had a larger number of channels, the  $NPS_{det}(f)$  could have been estimated by performing spatial averaging using a periodogram method (Williams,1999). Increasing the number of channels in this detector is currently underway.

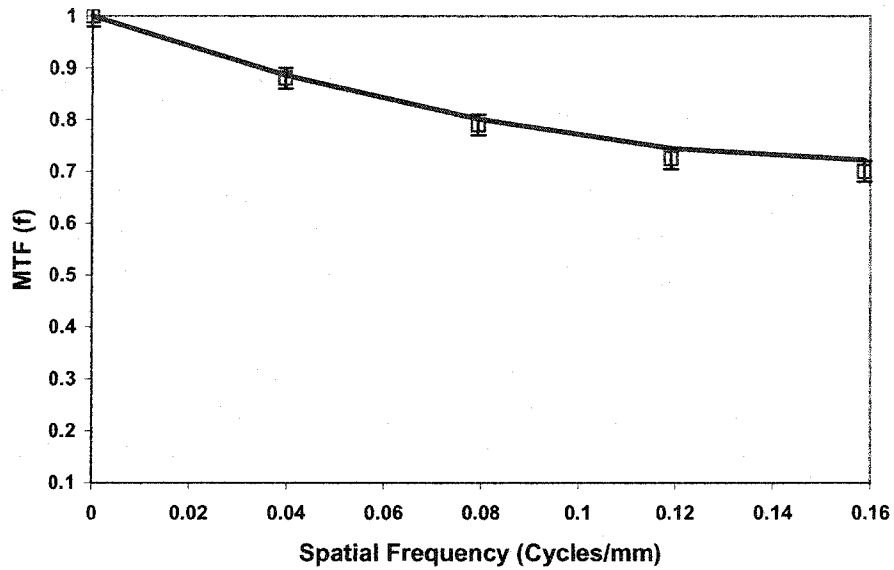


**Figure 4.19:** The modeled (line) and measured (squares) MTF(f) for the 8-element crystal array in a 6 MV beam.

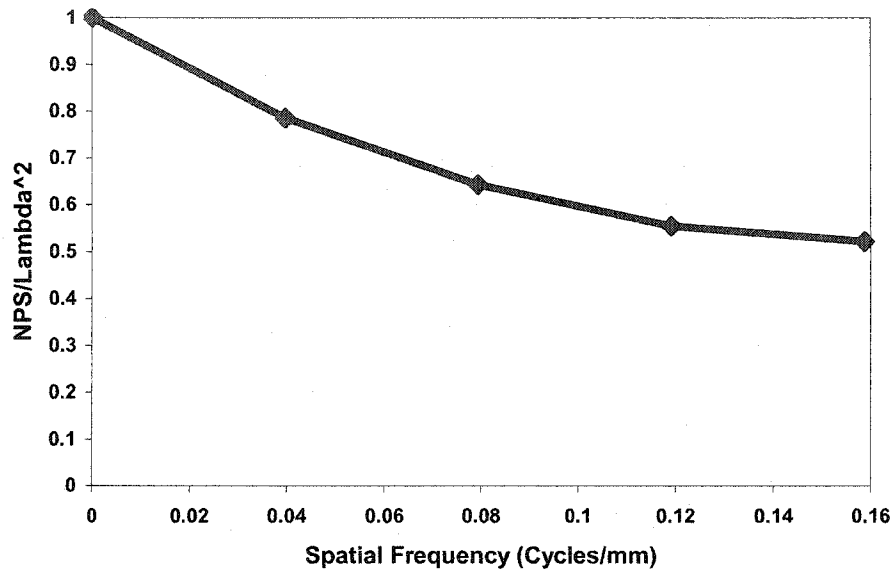


**Figure 4.20:** The modeled NPS(f) for the 8-element crystal array in a 6MV beam.

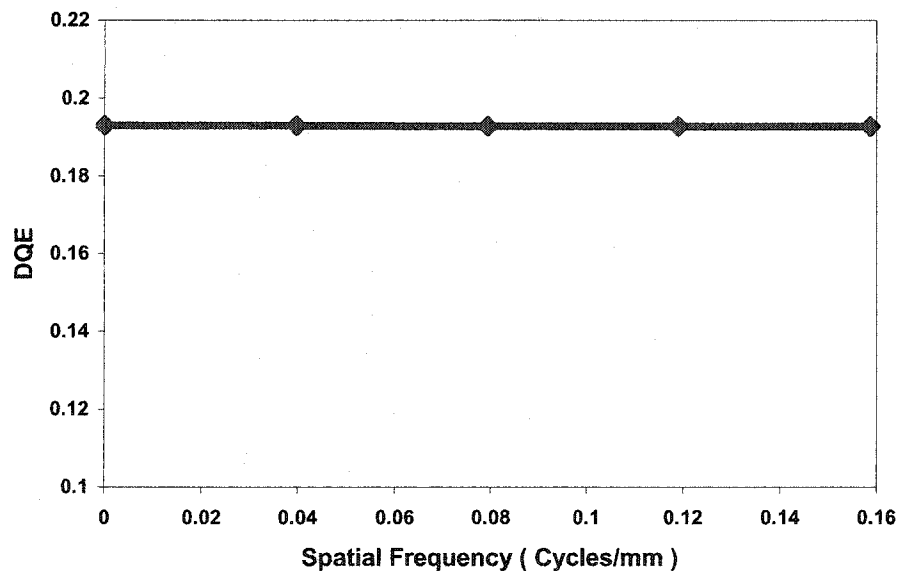


**Figure 4.21:** The modeled DQE(f) for the 8-element crystal array in 6MV beam.

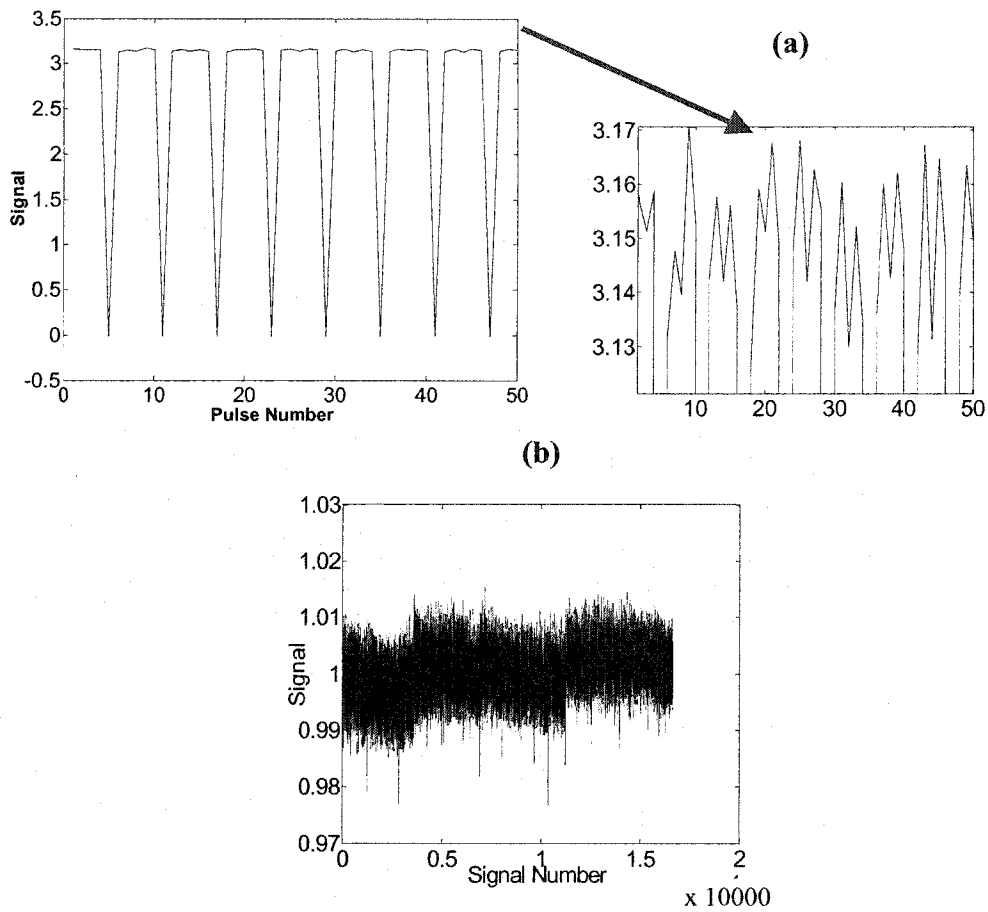


**Figure 4.22:** The pulse to pulse fluctuations in the output of a Varian 600C linac as measured by our detector. (a) This figure shows the signal for 50 pulses. The small figure on the right is a zoomed y-axis. (b) This is a more global view of the fluctuations. The signal in all eight channels is shown only for the pulses where the radiation is on. The signals are corrected for the dark current and normalized to the mean detector signal.



It should be noted that the modeled  $DQE(f)$  stays almost constant as a function of spatial frequency. This result is in contrast to the indirect detection active matrix flat panel imagers that use a thick phosphor screen for MV portal imaging (Lachaine et al., 2001). In these detectors, the  $DQE(f)$  falls significantly as a function of spatial frequency mainly because the optical scattering in turbid phosphor is significant, e.g. the mean free path is approximately  $25 \mu\text{m}$  in  $\text{Gd}_2\text{O}_2\text{S}$  (Kausch et al., 1999). In addition, the optical photons generated in the top layers of the screen scatter significantly more than the optical photons generated near the photo-detector. This causes additional noise correlation among pixels. The optical scattering between neighbouring crystals in our  $\text{CdWO}_4$  array is non-existent due to the gelcoat reflective coating. This is the reason that the  $DQE$  is essentially constant at all spatial frequencies. In practice, there might be a slight optical scattering within the optical glue sheet below the crystals. As a result, one may see a little drop in measured  $DQE(f)$ , as evident in Figure 4.18. We may also have underestimated both the thickness of the optical glue and its scattering mean free path in our model.

Since the mean photon energy for 6 MV photons is only slightly higher than 1.25 MeV, we expect the MTFs for these two energies to be fairly close. Our results satisfy this expectation with the  $MTF(f)$  for 6MV being slightly higher due to the more forward scattered photons generated in the crystal at this energy.

Due to the larger (0.275 cm) size of individual crystals along the array and the small number of crystals in the array, our results may suffer from significant aliasing. There are only 5 independent points in the spatial frequency domain. The important result, however, is that there is good agreement between the model and measurements. A larger crystal array (80-element) is currently being developed to address the problem of measuring NPS for a linear accelerator. In this case, the NPS can be obtained by using spatial averaging instead of temporal averaging, which is inadequate because of pulse to pulse variations. Monte Carlo simulations for a thinner crystal (0.1175 cm) along the array are also presented in the following chapter to address the aliasing problem.

## References:

- <sup>1</sup> Bushberg J.T., Seibert J.A., Leidholdt E.M., Boone J.M., *The Essential Physics of Medical Imaging*, (Lippincott Williams & Wilkins, Philadelphia, 2002).
- <sup>2</sup> Eijk C.W.E., "Inorganic scintillators in medical imaging," *Phys. Med. Biol.* 47: R85-R106 (2002).
- <sup>3</sup> Johns H.E., Cunningham J.R., *The Physics of Radiology*, 4<sup>th</sup> ed. (Thomas, Springfield, IL, 1983).
- <sup>4</sup> Kausch C., Schreiber B., Kreuder F., Schmidt R., Dossel O., "Monte Carlo simulation of the imaging performance of metal/phosphor screens used in radiotherapy", *Med.Phys.* 26: pp. 2113-2124(1999).
- <sup>5</sup> Lachaine M., Fourkal E., Fallone B.G., "Detective quantum efficiency of a direct-detection active matrix flat panel imager at megavoltage energies", *Med. Phys.* 28: 1364-1372 (2001).
- <sup>6</sup> Williams M. B. , Mangiafico P. A. , Simoni P. U., "Noise power spectra of images from digital mammography detectors", *Med.Phys.*26: 1279-1293(1999).

## Chapter 5: FUTURE DIRECTIONS

The good agreement between the modeled and experimental data in chapter 4 suggests that the two-step Monte Carlo modeling approach accurately predicts signal formation in single crystals as well as crystal arrays. In this chapter, the modeling method is applied to different crystal geometries. In the first part, a 16-element crystal array is compared with the previous 8-element array in order to understand the effect on MTF(f), NPS(f) and DQE(f). In second part, the effect of increasing the crystal height on the imaging parameters is considered to determine a theoretical height that will provide the best DQE(f).

### 5.1 Aliasing

#### 5.1.1 Theory

The prototype array of eight CdWO<sub>4</sub> detectors is a discrete imaging system. As such it samples the input function at eight discrete locations in order to produce the detector output. In this case, the sampling interval can be considered as the distance between the middle points of two consecutive crystals; this length is 3.15 mm (crystal width + gap) as shown in Figure 3.2.

The process of breaking up a function into discrete representative points is called sampling (Cunningham, 2000). If a function  $d(x)$  has an infinite extent and is sampled with uniform spacing  $x_0$ , the resulting sequence of sampled values  $d(nx_0)$  or  $d_n$  corresponds to values of  $d(x)$  at positions  $x = nx_0$ , where  $n$  is an integer. In the case of our 8-element array,  $d_n$  ( $0 \leq n \leq 7$ ) represents the discrete detector signal. The sampling of a function can be represented as (Cunningham, 2000):

$$d^\diamond(x) = d(x) \sum_{n=-\infty}^{\infty} \delta(x - nx_0) = \sum_{n=-\infty}^{\infty} d(nx_0) \delta(x - nx_0) = \sum_{n=-\infty}^{\infty} d_n \delta(x - nx_0) \quad (5.1)$$

Equation 5.1 is the definition of sampling;  $d(x)$  is the pre-sampling continuous signal and  $d^\diamond(x)$  is a sequence of scaled  $\delta$  functions. The Fourier transform of  $d^\diamond(x)$  is given as follows:

$$F\{d^\diamond(x)\} = D(u) * \frac{1}{x_0} \sum_{n=-\infty}^{\infty} \delta(u - \frac{n}{x_0}) \quad (5.2)$$

where  $D(u)$  is the Fourier transform of  $d(x)$  and  $*$  is the convolution symbol. Equation 5.2 follows from the fact that multiplication in the spatial domain is equivalent to convolution in the Fourier domain. Therefore, the Fourier transform of  $d^\diamond(x)$  is equal to  $D(u)$  scaled by  $1/x_0$  and then superimposed with an infinite number of similarly scaled and replicated versions of  $D(u)$ , each centered at frequencies  $u = n/x_0$  (Cunningham, 2000).

These replications of  $D(u)$  may overlap if  $D(u)$  extends beyond  $u = \pm 1/2x_0$  where  $1/x_0$  is the sampling frequency (Cunningham, 2000). The sampling cut off frequency is equal to  $1/2x_0$ . If overlap occurs, the Fourier transform  $D(u)$  cannot be determined from sampled data. This is called aliasing, and if it occurs the original function  $d(x)$  cannot be recovered from the sampled values  $d(nx_0)$ .

The sampling theorem states that, in order to faithfully reconstruct a band-limited function (i.e.  $D(u) = 0 | u \geq u_{\max}$ ) from its samples, the sampling frequency must be greater than  $u_{Ny} = 2u_{\max}$ , where  $u_{Ny}$  is called the Nyquist sampling frequency (Cunningham, 2000).

### 5.1.2 Materials and Methods

Since the sampling interval in our original CdWO<sub>4</sub> prototype detector array is set to 3.15 mm, the maximum possible frequency that the detector is able to evaluate is given by:

$$u_{\max} = \frac{1}{2x_0} = \frac{1}{2 \bullet 3.15\text{mm}} = 0.16\text{cycles / mm} \quad (5.3)$$

In the simulations, the dimensions of the crystals were decreased to 0.1175 x 0.8 x 1 cm<sup>3</sup> in order to study the effects of increasing  $u_{\max}$  on the MTF(f), NPS(f) and DQE(f) of the detector. Decreasing the crystal dimensions as such means that each crystal is in contact with one photodiode. Therefore, we studied the imaging characteristics of an array of 16 CdWO<sub>4</sub> crystals where two consecutive crystals are 0.04 cm apart. Since  $x_0$  is decreased to 1.575 mm,  $u_{\max}$  is increased to 0.32 cycles/mm in this case. With the exception of changing the dimensions of the crystals, our methods were identical to those described in section 3.6.1. Notice that, even though the spatial sampling interval changes from 3.15 to 1.575 mm, the frequency sampling interval,  $\Delta u$ , remains the same as it is given by (Cunningham, 2000) the maximum size of the array in the spatial domain:

$$\Delta u = \frac{1}{Nx_0} \quad (5.4)$$

where N is the number of sampled points. The product  $Nx_0$  remains the same irrespective of the number of elements used in the array. Therefore, up to 0.16 cycles/mm, the two arrays provide MTF(f) and NPS(f) at 5 identical spatial frequency values.

### 5.1.3 Results and Discussion

The simulated imaging characteristics of the 8 and 16 element array of  $\text{CdWO}_4$  crystals in 1.25 MeV and 6 MV beams are shown in Figures 5.1 to 5.6, respectively. As expected, the 16-element array provides information up to a spatial frequency of 0.32 cycles/mm that is twice the corresponding spatial frequency of the 8-element array. Up to spatial frequency of 0.16 cycles/mm, there are small discrepancies between the information provided by the simulation of the two arrays.

As mentioned at the end of chapter 4, the modeling analyses are carried out in complete isolation to a real CT scanner. Therefore, the finite size of the x-ray focal spot is not considered in these analyses. The lateral blurring in the detector signal occurs only due to Compton scattering within the scintillation material. As such, this spread would be very narrow in the high density and high atomic number material. Such a narrow function is not adequately sampled by either the 8-element or 16-element array. The imaging characteristics presented in the following figures for the 8-element and 16-element arrays are both significantly aliased; there is only a slight improvement shown in the data for the 16-element array. The important point to be noted is that the 16-element array doubles the operating range of spatial frequency without having an adverse effect on the noise characteristics or DQE. Therefore, barring limitations associated with the other sub-systems in the imaging cascade such as finite x-ray source size, convolution filter, and interpolation type, a 16-element detector array will provide images with higher spatial resolution. The fact that imaging characteristics for both detector arrays are aliased in the spatial frequency domain is not a concern in practice since a significant blurring is provided by both the finite size of the x-ray source and in-patient scattered radiation.

As such, one can continue to reduce the lateral size of the crystals in order to assess the gain in frequency dependent imaging characteristic of this detector array. However, such an analysis in isolation from the other degrading factors may only be of theoretical importance.

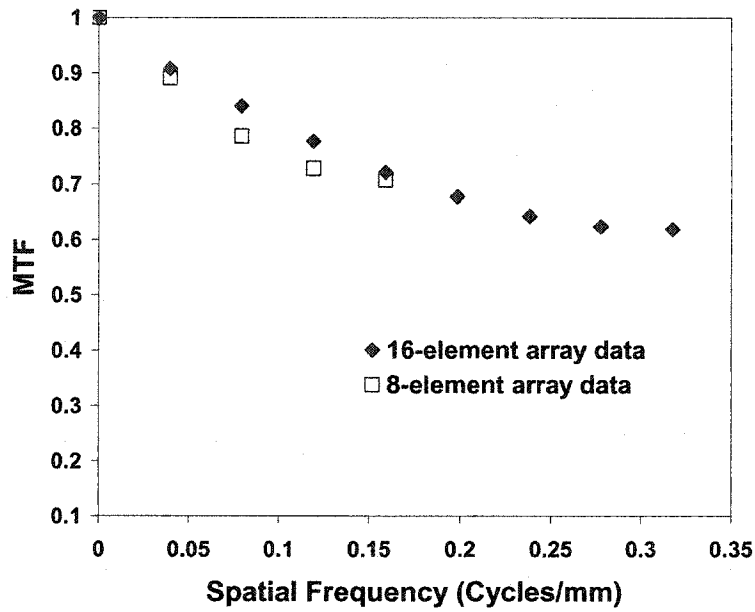


**Figure 5.1:** The simulated MTFs(f) of the 8 and 16-element arrays of CdWO<sub>4</sub> crystals in a 1.25 MeV beam.

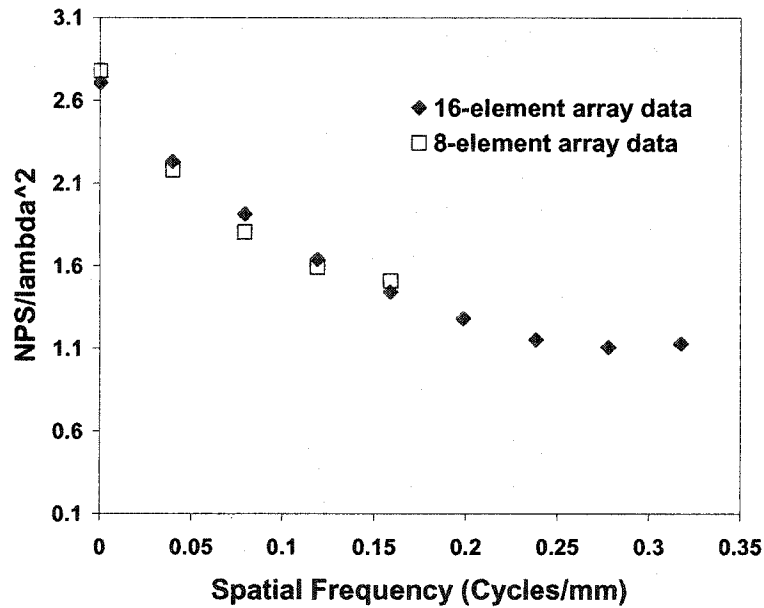


**Figure 5.2:** The normalized NPS(f) of the 8 and 16-element arrays of CdWO<sub>4</sub> crystals in a 1.25 MeV beam.



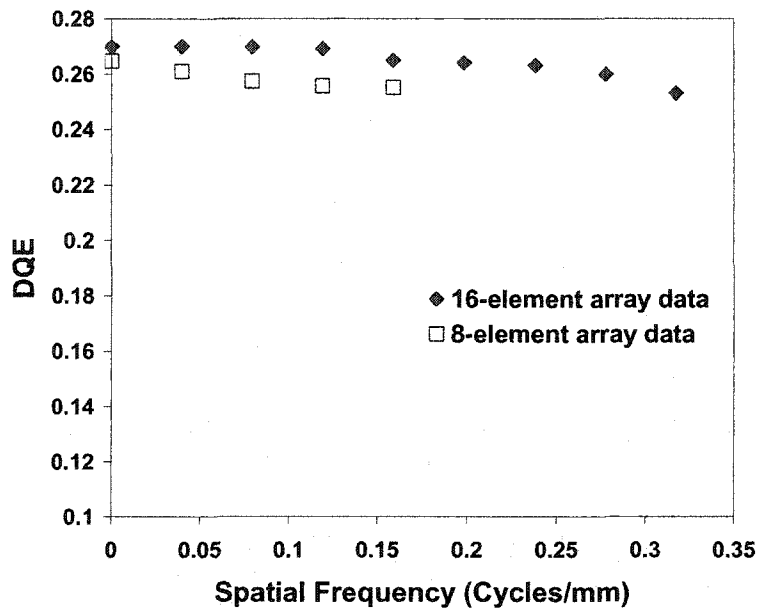


**Figure 5.3:** The DQE(f) of the 8 and 16-element arrays of CdWO<sub>4</sub> crystals in a 1.25 MeV beam.

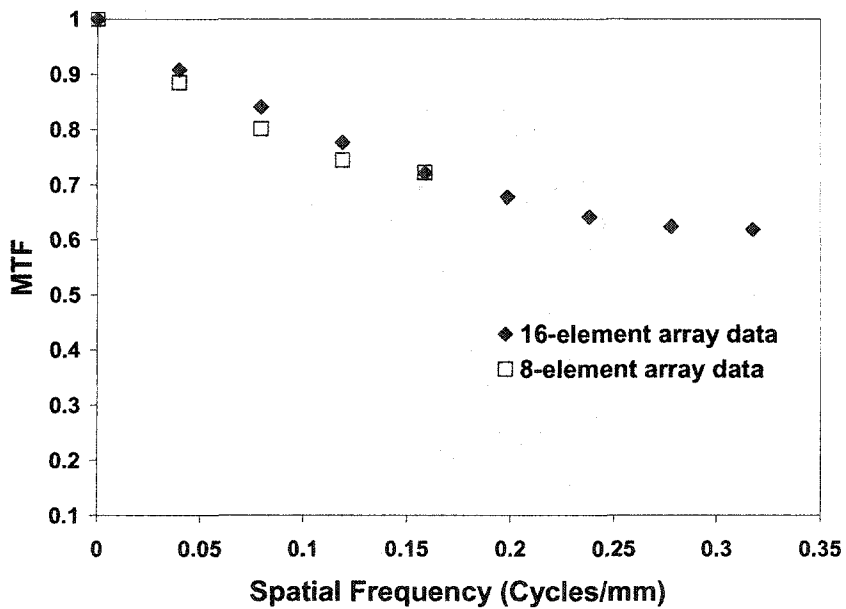


**Figure 5.4:** The MTF(f) of the 8 and 16-element arrays of CdWO<sub>4</sub> crystals in a 6 MV photon beam.

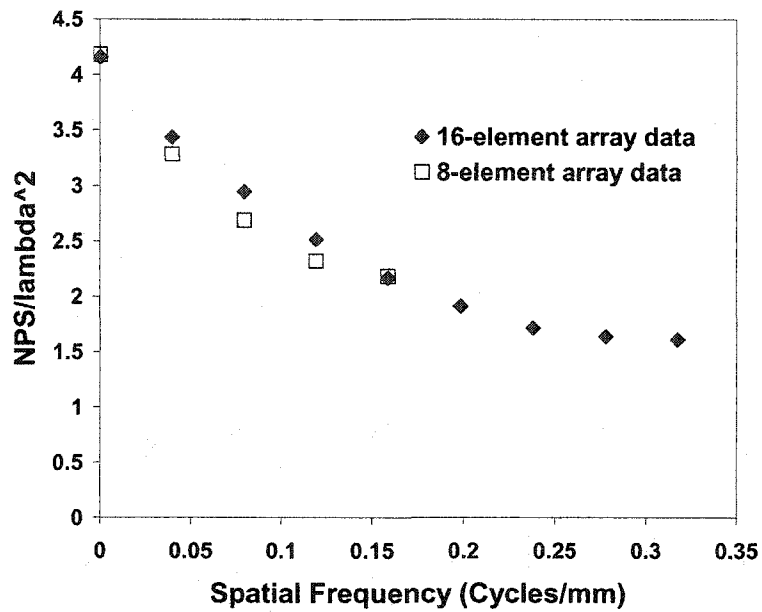


**Figure 5.5:** The normalized NPS(f) of the 8 and 16-element arrays of CdWO<sub>4</sub> crystals in a 6 MV photon beam.

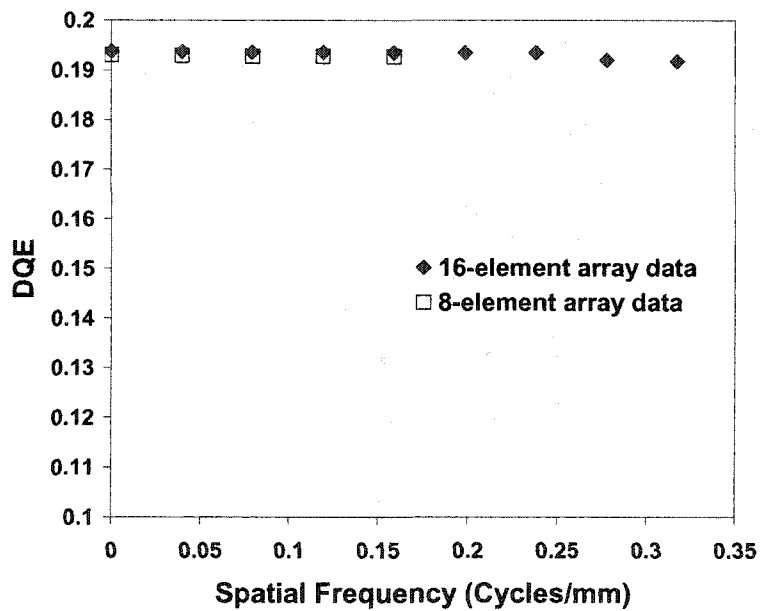


**Figure 5.6:** The DQE(f) of the 8 and 16-element arrays of CdWO<sub>4</sub> crystals in a 6 MV photon beam.

## 5.2 Crystal Height

The ultimate goal of this project is to use the proposed model for optimizing the CdWO<sub>4</sub> detector array to get the maximum possible DQE. The interplay of many parameters affects the final DQE of this detector. Some of these parameters include the width, length, height and surface coating of the crystals used in the design of the detector. In this section, the imaging characteristics of 8-element crystal arrays of various heights are calculated using the model described in chapter 4. The results presented are preliminary and not verified by measurement.

### 5.2.1 Materials and Methods

Methods identical to the ones described in section 3.6.1 were used. The array of 8 CdWO<sub>4</sub> crystals shown in Figure 3.2 was used for each simulation except for the crystal heights. Using Swank's method (see section 3.6.3) and the results of the EGSnrc simulations for crystals of height 3, 4, 5, 6 and 8 cm, the upper limit of DQE(0) was checked for this detector. It is worth noting that the results obtained using the theory of section 3.6.3 and equations 3.47 and 2.48 only predict the imaging characteristics of the detector assuming that optical photon transport does not degrade the noise transfer characteristics, and hence are strictly upper limits. Only a 1.25 MeV beam was considered in the simulations. The number of optical photons reaching the photodiodes from upper layers of very tall crystals may be very small. Therefore, additive noise due to optical photons may be present in the detector signal.

The MTF, NPS and DQE of the detector arrays were simulated for crystals of heights 5, 6 and 8 cm using the theory of section 3.6.1. As the crystals become taller, more of the x-ray photons have a chance to deposit their energy in the

detector. Therefore, the quantum efficiency of the detector increases with crystal height; however, the same is not true for the DQE. This is because, as the height of crystals increases, less and less of the optical photons created in the top layers of the detector, i.e. the layers farther away from the photodiodes, make their way to the photodiodes before being absorbed in the crystal bulk or surfaces. Hence, at some optimal height the DQE reaches its maximum value and then starts to decrease as the height of the crystals is increased further.

### 5.2.2 Results and Discussion

The upper limit of DQE(0) for crystals of height 3, 4, 5, 6, 7 and 8 cm are shown in Table 5.1 along with the first three moments of the associated AEDs. The values shown in this table indicate that as the height of the scintillation crystals increases, so does the upper limit for DQE(0). However, the rate of increase is more pronounced from 3 to 5 cm (the DQE(0) increases from 58% to 73%) than from 5 to 8 cm (the DQE(0) elevates from 73% to 80%). Since Swank's analysis for checking the upper limit of the DQE ignores optical transport, it is expected that the DQE will keep on increasing slowly as the crystal height is increased further.

The simulated MTF(f)s, NPS(f)s, and DQE(f)s of the prototype detector with crystals of height 5, 6 and 8 cm are shown in Figures 5.7, 5.8 and 5.9 respectively. From Figure 5.7, it may be concluded that the MTF(f) of the detector changes very slightly as the crystal heights are increased. It appears that the lateral spread of the energy deposition in CdWO<sub>4</sub> crystals does not change significantly with crystal height. The effect of increasing crystal height on MTF (f) is thus not visible unless the lateral crystal dimension is significantly reduced to reduce the aliasing. Therefore, it can be speculated that the spacing between the crystals

might have a more severe impact on the degradation of the MTF compared with the increase in height.

Figure 5.8 shows that the NPS( $f$ ) of the detector decreases as a function of height of the crystals. This decrease is mostly due to the fact that as the height of the crystals increases, the statistical variation in the energy deposition of  $\gamma$  photons goes down, i.e. we can predict with more confidence that one photon is going to deposit all of its energy in the detector. However, as the height of the crystals keeps on increasing, the optical photons generated in the layers of the crystal far away from the photodiodes may not be detected anymore. Therefore, the statistical uncertainty in the detection of optical photons increases. The interplay of these two factors is evident in the fact that the NPS( $f$ ) almost stays constant as the height of the crystals is increased from 6 to 8 cm. Consequently, the DQE( $f$ ) of the detector also stops increasing at a crystal height of approximately 6 cm as shown in Figure 5.9.

From Figure 5.9, it may be concluded that the optimal height for the detector lies somewhere around 6 cm. However, as we have no way of verifying our results experimentally, it must be emphasized that the results of this section have to be taken with caution. There are several reasons why the results of this section may not be accurate. The two main reasons are stated below:

- The main assumption in the analysis employed in section 3.6.1 is that the small quantum noise associated with the creation of optical photons is negligible compared with the large quantum noise of the  $\gamma$  ray interactions (Kausch, 1999). However, as the height of the crystals is increased, a smaller fraction of optical photons is detected from shallower depths in the crystal. The statistical noise associated with these optical photons may become comparable to the statistical noise associated with

the number of interacting  $\gamma$  photons. Ignoring quantum noise associated with the detection of optical photons, especially those created farther away from the photodiode, results in underestimating the NPS of the detector and subsequently overestimating the DQE.

- The high DQE of the detector as the height of the crystals is increased is a result of the excellent optical properties of the crystals. Figures 5.10 to 5.13 show the detected fraction, bulk absorbed fraction, surface absorbed fraction and transmitted fraction through the photodiodes as a function of the depth of the optical line source in a 6 cm tall crystal. Notice that the greater depths are closer to the photodiodes. As the depth of the optical line source is increased from 0.5 to 59.5 mm, the fraction of detected optical photons increases by 2.7%, the fraction of bulk absorbed optical photons decreases by 4%, the fraction of surface absorbed optical photons decreases by 5.3%, and the fraction of transmitted optical photons increases by 6.6%. Figure 5.10 indicates that in a 6 cm tall  $\text{CdWO}_4$  crystal, almost 3% of the optical photons that are generated 59.5 mm away from the photodiodes get detected. However, as indicated in chapter 3, the optical properties of the crystals were never determined experimentally in this research. Therefore, to further use the developed model it is best to verify these properties by performing experiments on the crystals available to us.

For the reasons stated above, our attempts in finding the optimal height for the  $\text{CdWO}_4$  crystal should only be taken as the first step in the future direction of this project. The optical properties of the  $\text{CdWO}_4$  crystals need to be determined accurately before any further attempts to optimize the dimensions of this detector.

**Table 5.1:** Results of the preliminary assessment of DQE(0) for the array of the CdWO<sub>4</sub> detector with crystals of height 3, 4, 5, 6, and 8 cm in a 1.25 MeV beam, using the Swank analysis of section 3.6.3.

Crystal Height (cm)	M <sub>0</sub> (Quantum Efficiency)	M <sub>1</sub>	M <sub>2</sub>	DQE(0)
3	0.72	0.58	0.60	0.58
4	0.84	0.68	0.70	0.67
5	0.90	0.74	0.76	0.73
6	0.93	0.78	0.80	0.77
7	0.95	0.81	0.83	0.79
8	0.96	0.82	0.85	0.80

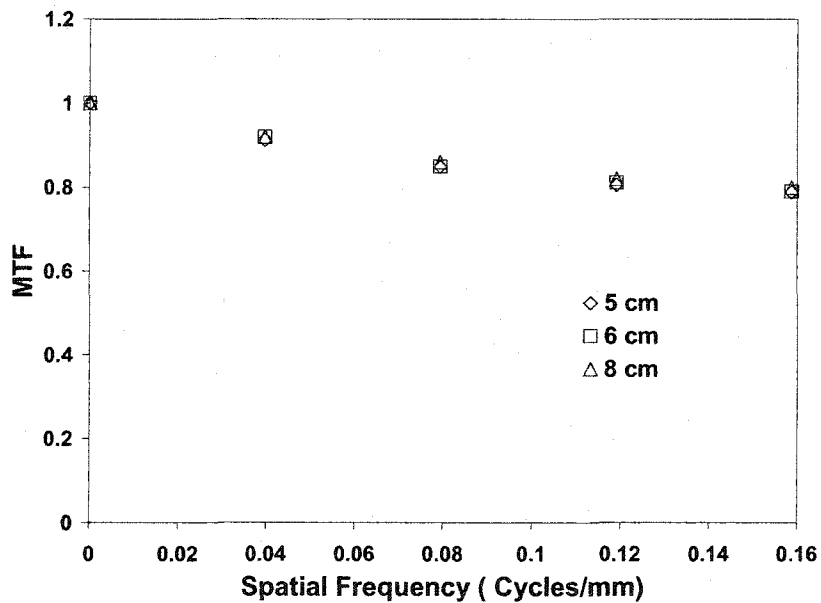


**Figure 5.7:** The results of the simulations for the MTF(f) of the 8-element CdWO<sub>4</sub> array with crystal heights of 5, 6, and 8 cm in a 1.25 MeV beam.

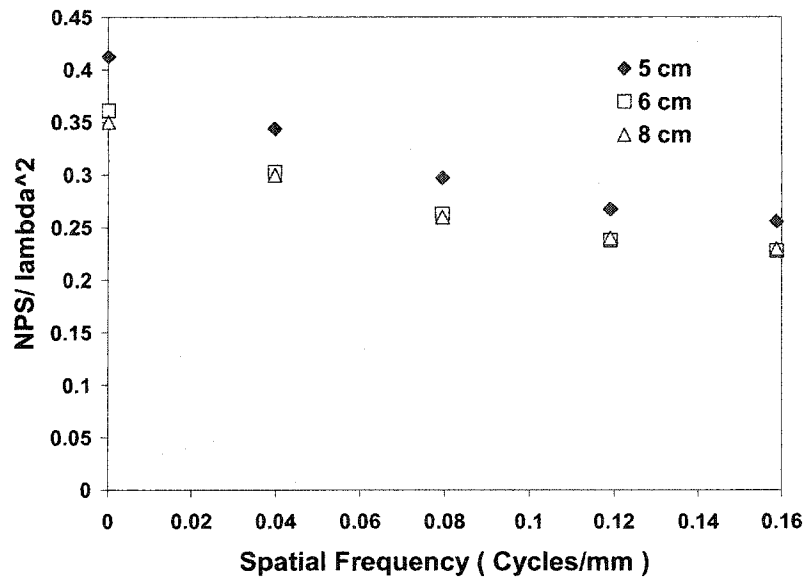


**Figure 5.8:** The results of the simulations for the normalized NPS( $f$ ) of the 8-element CdWO<sub>4</sub> array with crystal heights of 5, 6, and 8 cm in a 1.25 MeV beam.

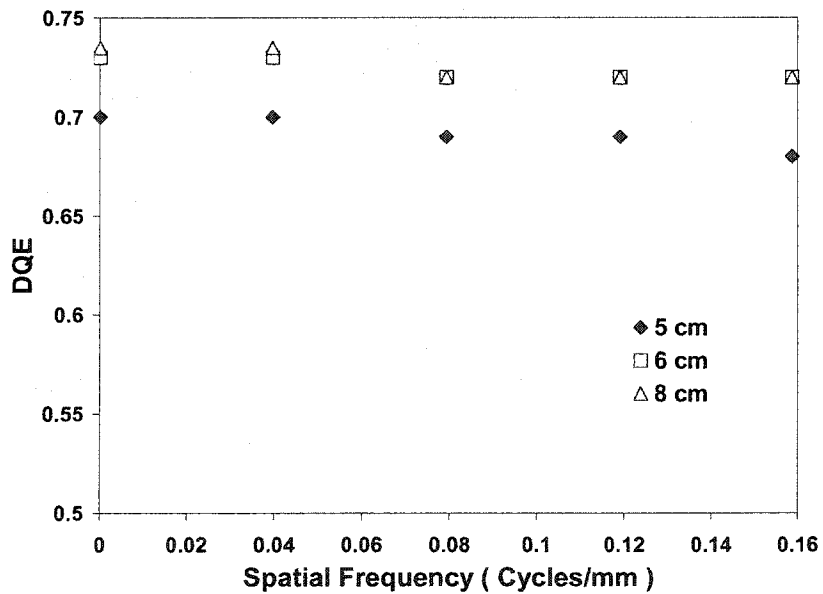


**Figure 5.9:** The results of the simulations for the DQE( $f$ ) of the 8-element CdWO<sub>4</sub> array with crystal heights of 5, 6, and 8 cm in a 1.25 MeV beam.



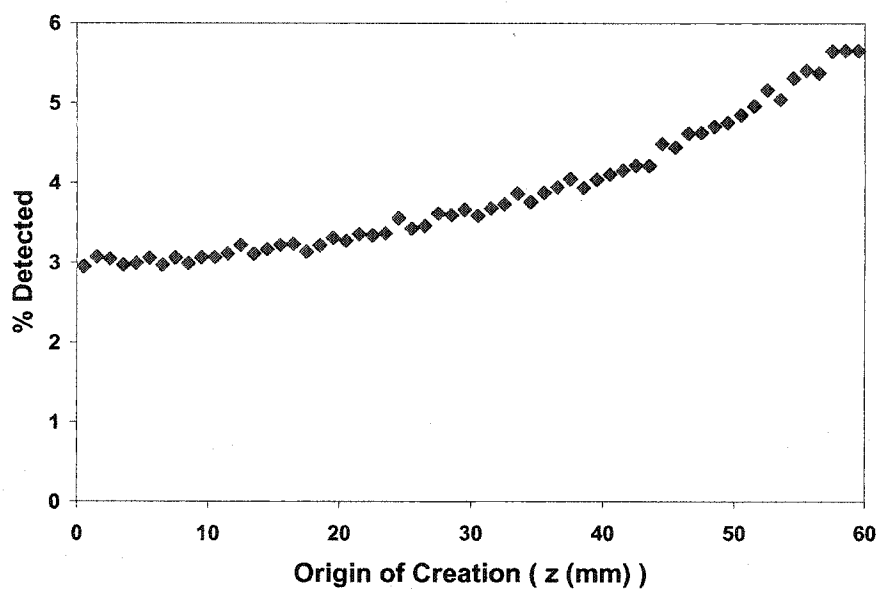


**Figure 5.10:** The fraction of optical photons detected, as a function of the original  $z$  location of the optical photon line source in a  $2.75 \times 8 \times 60 \text{ mm}^3$  ( $x y z$ )  $\text{CdWO}_4$  crystal.

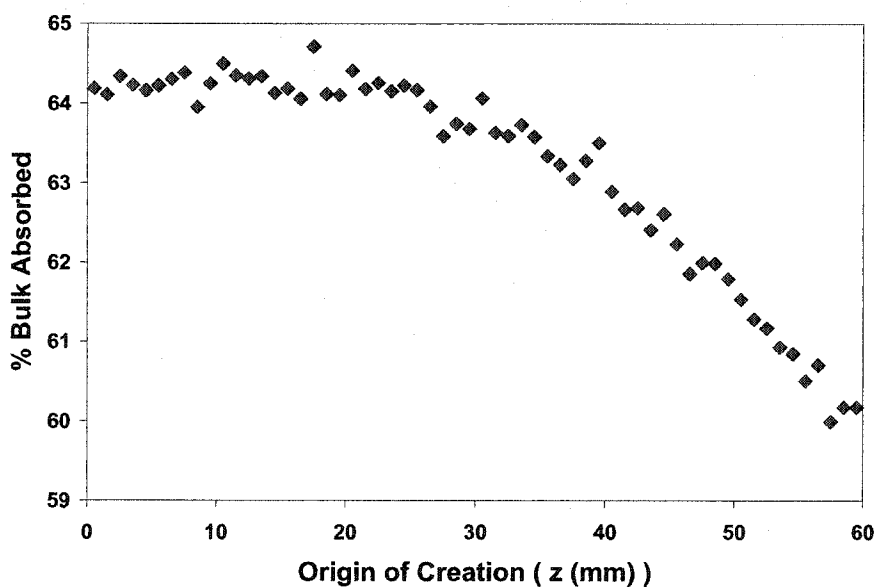


**Figure 5.11:** The fraction of optical photons bulk absorbed, as a function of the original  $z$  location of the optical photon line source in a  $2.75 \times 8 \times 60 \text{ mm}^3$  ( $x y z$ )  $\text{CdWO}_4$  crystal.

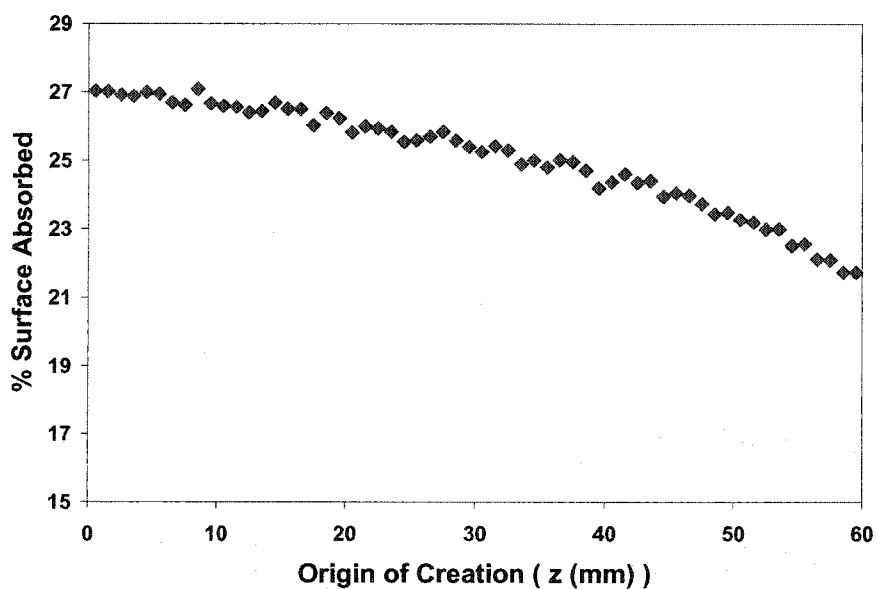


**Figure 5.12:** The fraction of optical photons surface absorbed, as a function of the original z location of the optical photon line source in a  $2.75 \times 8 \times 60 \text{ mm}^3$  (x y z)  $\text{CdWO}_4$  crystal.

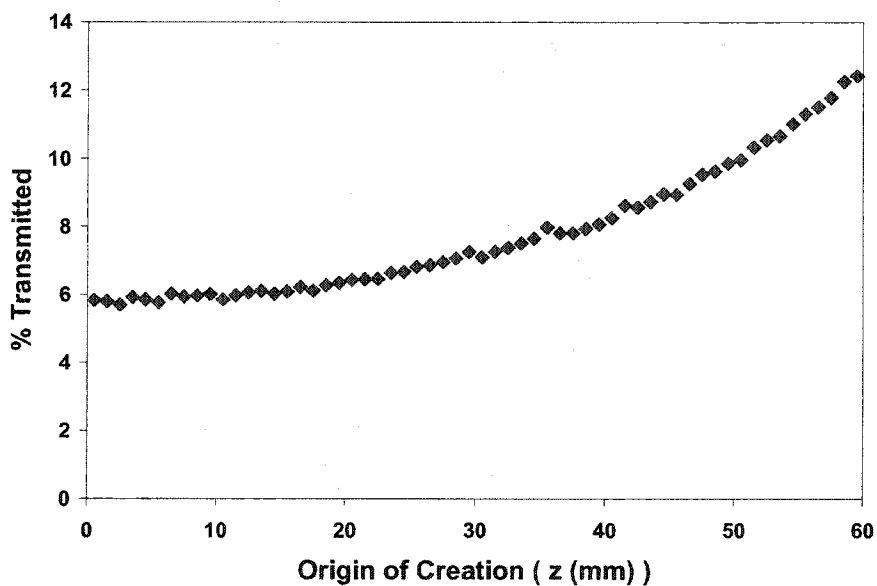


**Figure 5.13:** The fraction of optical photons transmitted, as a function of the original z location of the optical photon line source in a  $2.75 \times 8 \times 60 \text{ mm}^3$  (x y z)  $\text{CdWO}_4$  crystal.

**References:**

<sup>1</sup> Cunningham I. A., *Applied Linear-Systems Theory*, Chapter 2, Handbook of Medical Imaging Vol 1, Ed. R.L. Van Metter (SPIE Publications 2000).

<sup>2</sup> Kausch C., Schreiber B., Kreuder F., Schmidt R., Dossel O., "Monte Carlo simulation of the imaging performance of metal/phosphor screens used in radiotherapy", *Med.Phys.* 26: pp. 2113-2124(1999).

## Chapter 6: CONCLUSIONS

In this work, the use of both CdWO<sub>4</sub> and CsI(Tl) scintillation crystals in MVCT imaging was studied. First the signal generated by CsI(Tl) and CdWO<sub>4</sub> single crystals in a Co<sup>60</sup> beam was simulated and measured. In addition, measurements were made in a radiographic simulator beam to assess the afterglow of the two types of crystals. The simulations were done using EGSnrc for high energy photons and DETECT2000 for optical photons. A prototype detector was assembled which includes eight CdWO<sub>4</sub> crystals of size 2.75 x 8 x 10 mm<sup>3</sup> and sixteen photodiodes so that each crystal is in contact with two photodiodes. The linearity of the prototype detector was assessed by measuring the response of the detector in both open and blocked Co<sup>60</sup> beams. The ability of the detector to linearly measure the attenuation of a Co<sup>60</sup> beam by solid water was also assessed. The imaging characteristics of the detector were studied in both Co<sup>60</sup> and 6 MV beams. These imaging characteristics include the frequency dependent modulation transfer function, MTF(f), noise power spectrum, NPS(f), and detective quantum efficiency, DQE(f). Due to random fluctuations in the temporal output of the linear accelerator, we were unable to verify the NPS(f) and DQE(f) in the 6MV beam. The other parameters were verified by measurements. As part of the preliminary steps taken towards the future direction of this project, the imaging characteristics of a sixteen element CdWO<sub>4</sub> detector with crystals of size 1.175 x 8 x 10 mm<sup>3</sup> each in contact with only one photodiode were simulated. In addition, the effect of increasing the crystal height on the DQE(f) in the eight element detector was investigated to determine the best possible theoretical DQE(f) and hence optimum crystal height.

### **Afterglow**

The results of the afterglow assessment show that the CsI(Tl) scintillator retained about 0.5% of the beam-on signal 60 msec after the beam was turned off compared to only 0.02% in the case of CdWO<sub>4</sub>. This long afterglow and its hygroscopic nature are the main shortcomings of CsI(Tl) crystals in CT scanning. Therefore, CdWO<sub>4</sub> crystals were chosen for the prototype detector despite a smaller number of optical photons produced per deposited MeV as compared to CsI(Tl).

### **Single Crystals**

The comparison between the Monte Carlo simulated and measured response of the single crystals in a Co<sup>60</sup> beam shows good agreement. Therefore, we may conclude with confidence that the parameters chosen to define the crystal geometry and optical photon properties, such as the reflection coefficient of the teflon tape coating, are accurate.

### **Linearity**

The response of the prototype detector was found to be linear both as a function of dose in free space and of overlaying thickness of solid water in a narrow Co<sup>60</sup> beam. The linear response of the detector allows us to apply cascade imaging analysis theories to calculate the imaging characteristics of the detector.

### **Imaging Characteristics of the 8-element CdWO<sub>4</sub> Array**

Checking the upper limit of DQE(0) by ignoring the optical photon interactions in the crystals and employing Swank analysis suggests a DQE(0) of slightly above 26% and 19% for the detector in Co<sup>60</sup> and 6 MV beams, respectively. The results of the Monte Carlo simulations in the Co<sup>60</sup> beam predict a MTF(0.16) slightly higher than 70% and an approximately constant DQE(f) of 26% up to 0.16 cycles/mm. These predictions were verified in a Co<sup>60</sup> teletherapy

beam. The maximum discrepancies between the modeled and measured MTF(f), NPS(f) and DQE(f) were found to be 1.5%, 1.2% and 1.9% respectively. The Monte Carlo simulations predict a MTF(0.16) of approximately 72% with maximum discrepancy of 2.5% between the corresponding measured values, while the DQE(f) stays approximately constant around 19%. Due to fluctuations in the output of the linear accelerator we were unable to verify the NPS(f) and hence DQE(f) in the 6 MV beam. The reason that DQE(f) stays approximately constant in this detector for the two photon energies is due to the negligible optical scattering in the detector. The fact that the MTF(f) of the detector is almost the same for the two energies is because the mean energy of the 6MV spectrum at approximately 2 MeV is close to 1.25 MeV.

#### **16-Element CdWO<sub>4</sub> Array**

As the prototype array is a digital detector and samples the radiation at spatial intervals equal to the distance between the centers of two adjacent elements, aliasing is unavoidable. In an attempt to study the effect of aliasing on the response of the detector, a 16-element array was modeled in DETECT2000. The size of each crystal is 1.175 x 8 x 10 mm<sup>3</sup>; each element is in contact with only one photodiode. This way we were able to predict the imaging characteristics up to a spatial frequency of 0.32 cycles/mm. It was found that, up to a spatial frequency of 0.16 cycles/mm, there are very small discrepancies between the information provided by the 8-element array and the 16-element array. Therefore doubling a spatial frequency does not have any adverse effects on the noise characteristics of DQE(f). Although reducing the detector size increases the spatial resolution, since the simulations ignore blurring factors such as the finite size of the x-ray source and patient scatter, improvements due to smaller elements may only be of theoretical importance.

### **Crystal Height**

Since the ultimate goal of this project is to optimize the detector dimensions and characteristics using a simulation model, as a preliminary step towards this goal, the effect of increasing the crystal height on  $DQE(f)$  was also studied. It was found that the  $DQE(f)$  of the detector increases up to a crystal height of 6 cm, beyond which optical photons generated in distal layers do not reach the photodiode. Therefore, 6 cm was reported as the height for which  $DQE(f)$  is theoretically optimized.

## BIBLIOGRAPHY

(In brackets after each entry are the pages on which the reference is referred to.)

- Barrett H., Swindell W., *Radiological Imaging: The Theory of Image Formation, Detection, and Processing*, (Academic Press, 1981). [1]
- Berndt A.G., "A Fourth Generation 192Ir Source-Based CT scanner for Brachytherapy", PhD thesis, University of Manitoba (2002). [16, 34:35, 67]
- Bushberg J.T., Seibert J.A., Leidholdt E.M., Boone J.M., *The Essential Physics of Medical Imaging*, (Lippincott Williams & Wilkins, Philadelphia, 2002). [16,20,23:25, 69:73, 94]
- Carol M.P., "Peacock<sup>TM</sup>: a system for planning and rotational delivery of intensity modulated fields," *Int.J. Img. Sys. Tech.* 6:56-61 (1995). [10]
- Cho G., Kim H. K., Chung Y. H., Kim D. K., Lee H. K., Suh T. S., and Joo K. S., "Monte Carlo analyses of x-ray absorption, noise and detective quantum efficiency considering therapeutic x-ray spectrum in portal imaging detector," *IEEE Trans. Nuc., Trans., Sci.* 48: 1423-1427(2001). [86: 87]
- Cunningham I. A., *Applied Linear-Systems Theory*, Chapter 2, Handbook of Medical Imaging Vol 1, Ed. R.L. Van Metter (SPIE Publications 2000). [116:118]
- Derenzo, S. and Moses W. W., "Experimental efforts and results in finding new heavy scintillators", Proceedings of the CRYSTAL 2000 International Workshop on Heavy Scintillators for Scientific and Industrial Applications, Chamonix, France, 125-135(1992). [33:34, 83]
- Duclos S. J., "Scintillator phosphors for medical imaging," *The Electrochemical Society Interface*, 34-38 (1998) [61:62]
- Eijk C.W.E., "Inorganic scintillators in medical imaging," *Phys. Med. Biol.* 47: R85-R106 (2002). [91]
- Endo M., Tsunoo T., Nakamori N., and Yoshida K., "Effect of scattered radiation on image noise in cone beam CT," *Med. Phys.* 28: 469-474 (2001). [18]
- Feldkamp L.A., Davis L.C., and Kress J.W., "Practical cone-beam algorithm," *J. Opt. Soc. Amer.*, 1: 612-619 (1984). [18]
- Ford E.C., Chang J., Mueller K., Sindhu K., Todor D., Mageras G., Yorke E., Ling C.C., and Amols H., "Cone-beam CT with megavoltage beams and an amorphous silicon electronic portal imaging device : potential for verification of radiotherapy of lung cancer," *Med. Phys.* 29: 2913-2924 (2002). [19]



- Glover G.H. and Eisner R.L., "Theoretical resolution of computed tomography systems," *J. Comput. Assist. Tomog.* 3: 85-91 (1979). [79]
- Groh B. A., Siewerdsen J. H., Drake D. G., Wong J. W., and Jaffray D. A., "A performance comparison of flat-panel imager-based MV and kV cone-beam CT," *Med. Phys.* 29: 967-975 (2002). [22]
- International Commission on Radiation Units and Measurements "Prescribing, Recording, and Reporting Photon Beam Therapy" ICRU Report 50, Washington, D. C. (1993). [5]
- International Commission on Radiation Units and Measurements, "Determination of Dose Equivalents Resulting from External Radiation Sources," ICRU Report 39, (1985). [12]
- Jaffray D.A., Siewerdsen J.H., Wong J.W., Martinez A.A., "Flat panel cone-beam computed tomography for image guided radiation therapy," *Int. J. Radiation Oncology Biol. Phys.* 53: 1337-1349 (2002). [18]
- Johns H.E., Cunningham J.R., *The Physics of Radiology*, 4<sup>th</sup> ed. (Thomas, Springfield, IL, 1983). [21:22, 49: 51, 53, 84, 98: 99, 106]
- Kapatoes J. M., Olivera G. H., Balog J. P., Keller H., Reckwerdt P. J., and Mackie T. R., "On the accuracy and effectiveness of dose reconstruction for tomotherapy," *Phys. Med. Biol.* 46: 943-966 (2001). [12, 20]
- Kausch C., Schreiber B., Kreuder F., Schmidt R., Dossel O., "Monte Carlo simulation of the imaging performance of metal/phosphor screens used in radiotherapy", *Med.Phys.* 26: pp. 2113-2124(1999). [77, 113, 126]
- Kawrakow I. and Rogers D. W. O., "The EGSnrc code system: Monte Carlo Simulation of electron and photon transport," NRCC Report PIRS-701(2002). [49, 51: 52]
- Keller H., Glass M., Hiderer R., Ruchala K., Jeraj R., Olivera G., and Mackie T.R., "Monte Carlo study of a highly efficient gas ionization detector for megavoltage imaging and image-guided radiotherapy", *Med. Phys.* 29: 165-175 (2002). [12, 21]
- Kinloch D. R., Novak W., Raby P., and Toepke I., "New developments in Cadmium Tungstate", *IEEE Trans. Nucl. Sci.*, 41: pp .752-754 (1994). [61:63]
- Krus D. J., Novak W. P., Perna L., " Precision linear and two-dimensional scintillation crystal arrays for x-ray and gamma ray imaging applications," Presented at The SPIE International Symposium on Optical Science, Engineering and Instrumentation, July 18-23, 1999, Hard X-ray, Gamma-Ray and Neutron Detector Physics (SPIE Vol. 3768) .[34]

- Kuriyama K., Hiroshi O., Sano N., Komiyama T., Tanaka S., Aikawa Y., Tateda Y., Araki T., Ikenaga S., Umatsu M., “A new irradiation unit constructed of self-moving gantry-CT and linac,” *Int. J. Radiation Oncology Biol. Phys.* 55: 428-435 (2003). [17]
- Lachaine M., Fourkal E., Fallone B.G., “Detective quantum efficiency of a direct-detection active matrix flat panel imager at megavoltage energies”, *Med. Phys.* 28: 1364-1372 (2001). [53, 82, 84, 113]
- Levin A. and Moisan C., “A more physical approach to model the surface treatment of scintillation counters and its implementation into DETECT,” in 1996 IEEE Nuclear Science Symp. Conf. Rec. 2, pp. 702-706 (1997). [54:58]
- Lewis D.G., Swindell W., Morton E.J., Evans P.M., and Xiao Z.R., “A megavoltage CT scanner for radiotherapy verification,” *Phys. Med. Biol.* 37: 1985-1999 (1992). [19]
- Mackie T. R., Holmes T., Swerdloff S., Reckwerdt P., Deasy J. O., Yang J., Paliwal B., and Kinsella T., “Tomotherapy: a new concept for the delivery of dynamic conformal radiotherapy,” *Med. Phys.* 20: 1709-1719 (1993). [10]
- Mohan R., “Intensity modulated radiotherapy”, in *Teletherapy: Present and Future*, edited by Mackie T.R and Palta J.R. (Advanced Medical Publishing, Madison, WI, 1996), pp.761-793. [8:11]
- Mosleh-Shirazi M.A., Evans P.M., Swindell W., Webb S., Partridge M., “A cone-beam Megavoltage CT Scanner for Treatment Verification in Conformal Radiotherapy”, *Radiotherapy and Oncology.* 48: 319-328 (1998). [19]
- Munro P., “Megavoltage radiation for treatment verification”, in *The Modern Technology of Radiation Oncology*, edited by Van Dyk J. (Medical Physics Publishing, Madison, WI, 1999), pp. 481-508. [11, 13:15]
- Pedrotti F. L., Pedrotti L. S., *Introduction to Optics*, Prentice Hall (Upper Saddle River, NJ, 1993). [55:56]
- Olivera G. H., Shepard D.M., Ruchala K., Aldridge J.S., Kapatoes J., Fitchard E.E., Reckwerdt P. J., Fang G., Balog J., Zachman J., Mackie T. R., “Tomotherapy”, in *The Modern Technology of Radiation Oncology*, edited by Van Dyk J. (Medical Physics Publishing, Madison, WI, 1999), pp. 521-588. [10]
- Rizzoni G., *Principles and Applications of Electrical Engineering*, 3rd Ed. (McGraw-Hill, 2000). [40]
- Rogers, D., EGSnrc Reference Manual, <http://www.irs.inms.nrc.ca/inms/irs/EGSnrc/pirs701/node58.html> (2002). [53]

Ruchala K.J., Olivera G.H., Schloesser E.A., Mackie T.R., “ Megavoltage CT on a tomotherapy system,” *Phys. Med. Biol.* 44: 2597-2621 (1999). [20:22]

Shalev S., “Megavoltage portal imaging”, in *Teletherapy: Present and Future*, edited by Mackie T.R and Palta J.R. (Advanced Medical Publishing, Madison, WI, 1996), pp.445-469. [12:13]

Sheikh-Bagheri D., and Rogers D.W.O., “Monte Carlo calculation of nine megavoltage photon beam spectra using the BEAM code,” *Med. Phys.* 29: 391-402 (2002). [82:83]

Shepp L.A. and Logan, B.F., “The Fourier reconstruction of a head section,” *IEEE Trans.Nucl.Sci.*,21:21-43 (1974). [15]

Simpson R.G., Chen C.T., Grubbs E.A, Swindell W., “A 4-MV CT scanner for radiation therapy: the prototype system,” *Med. Phys.* 9: 574-579 (1982). [18:19]

Siewerdsen J. H., and Jaffray D. A., “A ghost story: spatial-temporal response characteristics of an indirect-detection flat-panel imager,” *Med. Phys.* 26: 1624-1641 (1999). [18]

Swank R. K., “ Absorption and noise in x-ray phosphors,” *J. Appl. Phys.* 44: 4199-4203 (1973). [86:87]

Van Dyk J., “Radiation oncology overview”, in *The Modern Technology of Radiation Oncology*, edited by Van Dyk J. (Medical Physics Publishing, Madison, WI, 1999), pp.1-19. [5,7]

Van Dyk J., Munro P., “Simulators”, in *The Modern Technology of Radiation Oncology*, edited by Van Dyk J. (Medical Physics Publishing, Madison, WI, 1999), pp.95-130. [6]

Webb S., *Intensity-Modulated Radiation Therapy*, Institute of Physics Publishing, (Bristol and Philadelphia, 2001). [9:11]

Williams M. B. , Mangiafico P. A. , Simoni P. U., “Noise power spectra of images from digital mammography detectors”, *Med.Phys.*26: 1279-1293(1999). [84, 111]

www.bicron.com [manufacturer of the crystals used in this study]

www.hamamatsu.com [manufacturer of the photodiodes used in this study]

www.gel.ulaval.ca/detect [DETECT2000 software website] [49, 54:58]